

BioMed Research International

Advances in Molecular Pathway-Directed Cancer Systems Imaging and Therapy

Guest Editors: David J. Yang, Lan Pham, Mei-Hsiu Liao, Fan-Lin Kong,
Hiroji Uemura, and Yen-Yu Ian Shih





Advances in Molecular Pathway-Directed Cancer Systems Imaging and Therapy

BioMed Research International

Advances in Molecular Pathway-Directed Cancer Systems Imaging and Therapy

Guest Editors: David J. Yang, Lan Pham, Mei-Hsiu Liao,
Fan-Lin Kong, Hiroji Uemura, and Yen-Yu Ian Shih



Copyright © 2014 Hindawi Publishing Corporation. All rights reserved.

This is a special issue published in “BioMed Research International.” All articles are open access articles distributed under the Creative Commons Attribution License, which permits unrestricted use, distribution, and reproduction in any medium, provided the original work is properly cited.

Contents

Advances in Molecular Pathway-Directed Cancer Systems Imaging and Therapy, David J. Yang, Lan Pham, Mei-Hsiu Liao, Fan-Lin Kong, Hiroji Uemura, and Yen-Yu Ian Shih
Volume 2014, Article ID 639475, 2 pages

Patched Targeting Peptides for Imaging and Treatment of Hedgehog Positive Breast Tumors, Daniel Smith, Fanlin Kong, David Yang, Richard Larson, Jennifer Sims-Mourtada, and Wendy A. Woodward
Volume 2014, Article ID 525680, 9 pages

Design of CGMP Production of ^{18}F - and ^{68}Ga -Radiopharmaceuticals, Yen-Ting Chi, Pei-Chun Chu, Hao-Yu Chao, Wei-Chen Shieh, and Chuck C. Chen
Volume 2014, Article ID 680195, 8 pages

Automated Synthesis of ^{18}F -Fluoropropoxytryptophan for Amino Acid Transporter System Imaging, I-Hong Shih, Xu-Dong Duan, Fan-Lin Kong, Michael D. Williams, Kevin Yang, Yin-Han Zhang, and David J. Yang
Volume 2014, Article ID 492545, 11 pages

Evaluation of Inhibitory Effect of Recreational Drugs on Dopaminergic Terminal Neuron by PET and Whole-Body Autoradiography, Skye Hsin-Hsien Yeh, Ming-Hsien Lin, Fan-Lin Kong, Chi-Wei Chang, Li-Chung Hwang, Chien-Feng Lin, Jeng-Jong Hwang, and Ren-Shyan Liu
Volume 2014, Article ID 157923, 11 pages

Rational Design of a Triple Reporter Gene for Multimodality Molecular Imaging, Ya-Ju Hsieh, Luen Hwu, Chien-Chih Ke, Skye Hsin-Hsien Yeh, Chien-Feng Lin, Fu-Du Chen, Hsin-El Wang, Kang-Ping Lin, Ran-Chou Chen, and Ren-Shyan Liu
Volume 2014, Article ID 605358, 11 pages

Editorial

Advances in Molecular Pathway-Directed Cancer Systems Imaging and Therapy

David J. Yang,¹ Lan Pham,¹ Mei-Hsiu Liao,² Fan-Lin Kong,¹
Hiroji Uemura,³ and Yen-Yu Ian Shih⁴

¹University of Texas MD Anderson Cancer Center, Houston, TX 77030, USA

²Radiopharmaceuticals Production and Marketing Center, Institute of Nuclear Energy Research,
Atomic Energy Council, Taoyuan 32546, Taiwan

³Yokohama City University Graduate School of Medicine, Yokohama 236-0004, Japan

⁴Small Animal MRI, Biomedical Research Imaging Center, University of North Carolina at Chapel Hill, Chapel Hill, NC 27599, USA

Correspondence should be addressed to David J. Yang; jung-yang@msn.com

Received 7 September 2014; Accepted 7 September 2014; Published 21 December 2014

Copyright © 2014 David J. Yang et al. This is an open access article distributed under the Creative Commons Attribution License, which permits unrestricted use, distribution, and reproduction in any medium, provided the original work is properly cited.

Molecular nuclear imaging agents enable the comprehensive characterization of therapeutic intervention and can be used in patient selection, pharmacokinetic, dosage-finding, and proof-of-concept studies. The effort in image-guided cell therapy and theranostic approaches in parallel with instrumentation development would be more comprehensive in the outcome assessment of patient response to treatment. To extend the threshold of being able to provide personalized therapy for patients, the integration of imaging findings to genomic and proteomic systems profiling is essential to validate targeted pathways.

The Food and Drug Administration (FDA) permits radiopharmaceuticals produced under well-controlled conditions in central commercial facilities to be distributed to local clinics where they are administered. In addition, radiopharmaceutical production process must adhere to Current Good Manufacturing Practice (CGMP) compliance to ensure the quality of drug product that meets acceptance criteria. The CGMP compliance covers manufacturing process and facility, quality guidelines, and personnel training. Y.-T. Chi et al. reported the design of CGMP production for ¹⁸F- and ⁶⁸Ga-radiopharmaceuticals. The Pharmaceutical Inspection Convention and Pharmaceutical Inspection Cooperation Scheme (jointly referred to as PIC/S) are two international

instruments between countries and pharmaceutical inspection authorities, which provide together an active and constructive cooperation in the field of Good Manufacturing Practice (GMP). PIC/S' mission is to lead the international development, implementation, and maintenance of harmonized CGMP standards and quality systems of inspectorates in the field of medicinal products. They reviewed FDA and PIC/S guidelines for the synthesis of radiopharmaceuticals. Two examples, ⁶⁸Gallium-[1,4,7,10-tetraazacyclododecane-N,N',N'',N'''-tetraacetic acid]-D-Phe¹, Tyr³-octreotate (⁶⁸Ga-DOTATATE) and ¹⁸F-fluorodeoxyglucose (¹⁸F-FDG), were manufactured under CGMP process. They have reviewed acceptance criteria for these clinic useful radiopharmaceuticals.

Radiopharmaceutical chemistry requires intricate handling of radioactive materials, fast reaction times, ease of synthesis, and reproducible results. In the preclinical setting, radiopharmaceuticals are typically synthesized manually. Such applications use *in vitro* and small animal models to validate the agent and require low levels of radioactivity. The use of manual synthesis for clinical imaging, however, is challenging for multiple reasons: (1) clinical agents must meet strict sterility and pyrogenicity requirements which are validated from batch to batch; (2) batch-to-batch reproducibility is

required to demonstrate suitable radiochemical yield, radiochemical purity, and other quality control analyses; (3) synthesis time must be fast when dealing with radionuclides with a short half-life; (4) clinical studies require multiple patient doses and would expose radiochemists to much higher levels of radioactivity; and (5) production cost and availability of the technology may limit the viability of the agent in routine clinical practice. I.-H. Shih et al. reported the manufacturing of a cGMP grade of [^{18}F]fluoropropoxytryptophan (^{18}F -FTP) to assess tryptophan transporters. PET imaging studies were performed with ^{18}F -FTP and ^{18}F -FDG in prostate and small cell lung tumor-bearing animal models. They have reported that ^{18}F -FTP could be synthesized with high radiochemical yield. They conclude that ^{18}F -FTP may provide potential applications in differential diagnosis and prediction of early treatment response for carcinoids.

Molecular imaging science has been focused on imaging guidance in the areas of targeting epigenetic abnormalities and disease microenvironment in overcoming resistance in diseases. Multimodality imaging using noncytotoxic triple fusion (TF) reporter genes is an important application for cell-based tracking, drug screening, and therapy. Y.-J. Hsieh et al. reported the rational design of a triple reporter gene for multimodality molecular imaging. They reported that an optimized triple fusion reporter constructed with DsRedmfl-ttksr39 was developed and validated for more effective and sensitive *in vivo* animal imaging using fluorescence, bioluminescence, and PET imaging modalities. Their findings may facilitate different fields of biomedical research and applications.

The use of image-guided technologies to select patient for personalized therapy and to monitor therapeutic outcomes is the focus of this special issue. S. H.-H. Yeh et al. reported the evaluation of inhibitory effect of recreational drugs on dopaminergic terminal neuron by ^{18}F -FDOPA and whole-body autoradiography. They used ^{18}F -FDOPA PET imaging and autoradiographic techniques to assess the impact of recreational drugs such as ketamine, cocaine, and methamphetamine on dopamine neurons in peripheral organs. They have demonstrated that both dynamic ^{18}F -FDOPA PET and autoradiography were useful crossing-validating tools to evaluate the alteration of dopaminergic neurons in peripheral tissues. D. Smith et al. reported the application of patched targeting peptides for imaging and treatment of hedgehog positive breast tumors. Hedgehog (Hh) signaling is involved in breast cancer growth and metastasis and high tumor Sonic Hedgehog (SHh) expression is correlated with poor prognosis in invasive ductal carcinoma. Peptides which bind the PTCH receptor have recently been reported to have a growth inhibitory effect in tumors with activated Hh signaling. These peptides may be used as molecular imaging probes to monitor changes in Hh expression after chemotherapy. Their studies showed that peptides which bind the SHh docking site in PTCH-1 correlate with PTCH-1 expression and can be used to image PTCH-1 *in vivo*. They conclude that radiolabeled peptides may enable examining the activity of the Hh signaling pathway and evaluating response to anticancer therapies.

In summary, this special issue covers advances in molecular imaging in drug manufacturing under CGMP environment, preclinical drug discovery, image-guided drug response, and target validation using PET/SPECT hybrid with CT.

David J. Yang
Lan Pham
Mei-Hsiu Liao
Fan-Lin Kong
Hiroji Uemura
Yen-Yu Ian Shih

Research Article

Patched Targeting Peptides for Imaging and Treatment of Hedgehog Positive Breast Tumors

Daniel Smith,¹ Fanlin Kong,² David Yang,² Richard Larson,¹
Jennifer Sims-Mourtada,³ and Wendy A. Woodward¹

¹ Department of Radiation Oncology, The University of Texas M.D. Anderson Cancer Center, Houston, TX 77030, USA

² Department of Cancer Systems Imaging, The University of Texas M.D. Anderson Cancer Center, Houston, TX 77030, USA

³ Center for Translational Cancer Research, Helen F. Graham Cancer Center and Research Institute, Christiana Care Health System, 4701 Oglethorpe-Stanton Road, Newark, DE 19713, USA

Correspondence should be addressed to Jennifer Sims-Mourtada; jsimsmourtada@christianacare.org

Received 28 May 2014; Revised 11 July 2014; Accepted 15 July 2014; Published 8 September 2014

Academic Editor: Mei-Hsiu Liao

Copyright © 2014 Daniel Smith et al. This is an open access article distributed under the Creative Commons Attribution License, which permits unrestricted use, distribution, and reproduction in any medium, provided the original work is properly cited.

High tumor hedgehog expression is correlated with poor prognosis in invasive ductal carcinoma. Peptides which bind the patched receptor have recently been reported to have a growth inhibitory effect in tumors with activated hedgehog signaling. We sought to examine growth inhibition with these peptides in breast cancer cells and use these peptides as molecular imaging probes to follow changes in hedgehog expression after chemotherapy. Significant growth inhibition was observed in breast cancer cell lines treated with PTCH-blocking peptides. Significant *in vitro* uptake was observed with both FITC- and ^{99m}Tc-EC-peptide conjugates. *In vivo* imaging studies displayed greater accumulation of ^{99m}Tc-labeled peptides within tumors as compared to adjacent muscle tissue. Patched receptor expression increased after treatment and this correlated with an increase in tumor radiotracer uptake. These studies suggest that peptides which bind the sonic hedgehog docking site in patched receptor correlate with patched expression and can be used to image patched *in vivo*. Further, our data suggest that radiolabeled peptides may enable us to examine the activity of the hedgehog signaling pathway and to evaluate response to anti-cancer therapies.

1. Introduction

The hedgehog (Hh) signaling pathway plays a critical role in embryonic development and wound healing, and its aberrant activity is associated with several malignancies. Recent studies implicate Hh signaling in breast cancer growth and metastasis, and high tumor sonic hedgehog (SHh) expression is correlated with poor prognosis in invasive ductal carcinoma. SHh binds to the suppressive receptor patched-1 (PTCH-1) and relieves the inhibition of the transmembrane protein smoothed (Smo) by PTCH-1, resulting in the translocation of Gli transcription factors to the nucleus and activation of Hh target genes. In tumors with activated Hh signaling, high levels of PTCH-1 have been reported, especially within the tumor stroma.

Previously, we demonstrated strong detection of tumor xenografts using an iodinated derivative of the PTCH-1

binding ligand, sonic hedgehog [1]. Although this agent was capable of delineating tumor tissue, its clinical utility is limited due to poor stability and pharmacokinetics. Imaging with radiolabeled peptides has been shown to improve pharmacokinetics and the targeting of other tumor-based receptors. Therefore, we sought to develop radiolabeled peptides which dock inside the PTCH receptor. Nakamura et al. previously reported the synthesis of several peptides targeting the PTCH-1 receptor [2]. These peptides were shown to bind to the PTCH-1 receptor on the surface of pancreatic tumors and decrease tumor growth.

Here, we selected technetium-99 m (^{99m}Tc) as the radioisotope because of its favorable physical characteristics for diagnostic imaging studies and due to the ease of using its benchtop generator-based system for clinical applications. It emits 140 keV gamma ray, with an 89% branching fraction,

which can be detected by single photon emission computed tomography (SPECT). In addition, the half-life of ^{99m}Tc is relatively long (6.02 h) compared to most nuclear imaging radioisotopes, which facilitates serial imaging that may improve the differentiation of tumor from inflammation. To label the peptide with ^{99m}Tc , the chelator N,N'-ethylenedi-L-cysteine (EC) is selected and used as a linker. EC is known to chelate ^{99m}Tc stably owing to the efficient binding of the oxotechnetium group to the two thiols and two amine nitrogen atoms of EC.

Here, we report the radiolabeling of these peptides to detect the PTCH receptor on breast cancer cells and breast cancer stem cell-enriched populations. These molecular imaging probes have the potential to identify Hh-induced changes in PTCH-1 expression, which is useful for the imaging of aberrant Hh signaling in malignancies.

2. Methods

2.1. Peptides. PTCH-binding peptides A—sequence FAPVL-DGAVSTLLGV— and B—sequence DNTRYSPPPPYSSHS— were commercially synthesized with or without an N-terminal FITC-Ahx modification (GenScript, Piscataway, NJ). Peptides were resuspended at a stock concentration of 200 μM in 10% DMSO in deionized water.

2.2. Synthesis and Radiolabeling of PTCH. Ethylenedicysteine (EC) was selected as a chelator for PTCH conjugation. Sodium bicarbonate (1N, 1mL) was added to a stirred solution of EC (5 mg, 0.019 mmol). To this colorless solution, sulfo-NHS (4 mg, 0.019 mmol) and EC (5 mg, 0.019 mmol) were added. PTCH (0.3 mg) was then added. The mixture was stirred at room temperature for 24 hours. The mixture was dialyzed for 48 hours with a cutoff at molecular weight 10,000 Da. After dialysis, the product was freeze-dried, with the product in the salt form weighing 0.5 mg.

^{99m}Tc -pertechnetate was obtained from Mallinckrodt (Houston, TX). Radiosynthesis of ^{99m}Tc -EC-PTCH was achieved by adding the required amount of ^{99m}Tc -pertechnetate into EC-PTCH (0.1 mg) and tin chloride (II) (SnCl_2 , 100 mg). The mixture was loaded on a sephadex gel column (PD-10, G-25) (Sigma Chemical Company, St. Louis, MO) and eluted with phosphate-buffered saline (pH 7.4). One milliliter of each fraction was collected. The product was collected at fraction 3, with a 70% yield. Radiochemical purity was assessed by Radio-TLC (BioScan, Washington, DC) using saline as an eluant.

2.3. Cell Lines and Culture Conditions. The human cell lines T47-D, SKBR3, and MCF-7 were obtained from the American Type Tissue Company (ATCC) and cultured in DMEM with 10% fetal bovine serum (Atlanta Biologicals, Flowery Branch, GA) and 1% antibiotic-antimycotic (Invitrogen Life Technologies, Grand Island, NY Life Technologies, Grand Island, NY). The human cell line SUM159 was obtained from Asterand (Detroit, MI) and cultured in DMEM containing 1 $\mu\text{g}/\text{mL}$ hydrocortisone (Invitrogen Life Technologies, Grand Island, NY Life Technologies, Grand Island, NY),

5 $\mu\text{g}/\text{mL}$ insulin (Invitrogen Life Technologies, Grand Island, NY), and 1% antibiotic/antimycotic. The rat breast cancer cell line 13762 was derived from a tumor induced in a Fischer-344 rat by giving an oral dose of 7,12-dimethylbenz[a]anthracene [3], and the cells were cultured in RPMI-1640 medium, supplemented with 10% (vol:vol) fetal bovine serum and 1% antibiotic-antimycotic. For mammosphere assays, cells were cultured in MEM media supplemented with 1X B27 (Invitrogen Life Technologies, Grand Island, NY), 20 ng/mL epidermal growth factor (EGF; Invitrogen Life Technologies, Grand Island, NY), and 20 ng/mL basic fibroblast growth factor (bFGF; Invitrogen Life Technologies, Grand Island, NY) and seeded into ultralow attachment plates (Corning Life Sciences, Salt Lake City, UT). Cells were grown for 7–10 days and spheres were obtained. All cells were cultured at 37°C in a humidified atmosphere containing 5% carbon dioxide.

2.4. Survival Assays. Breast cancer cell lines were seeded into 96-well plates at a density of 5,000–7,000 cells per well. Cells were grown overnight and media were replaced with culture media containing unlabeled peptides A and B at the indicated concentrations. Cells were cultured for an additional 48 hours and survival was determined using the MTT-based Cell Proliferation Assay (Biotium). Data is expressed as %treated/untreated.

2.5. Fluorescence Microscopy. Breast cancer cell lines were seeded onto chamber slides (Nunc, Roskilde, Denmark) and grown overnight. For sphere assays, cells were seeded in 3D media as described above in 96-well low attachment plates at a density of 100–1000 cells per well and cultured for 7–10 days until spheres were formed. Spheres were filtered using a cell strainer and replated into low attachment plates. Cells or spheres were treated with 100 nM peptide A or B and incubated for 2 hours. Media were removed and cells or spheres were washed two times with 1X PBS. Following washes, 1 mL of 1X PBS was added to the slide or plate and cells or spheres were analyzed by fluorescence microscopy using a Zeiss motorized AxioObserver Z1 microscope. For co-localization experiments, cells were seeded at a density of 7000 cells per well in a chamber slide and cultured overnight. Cells were incubated with 100nM peptide and incubated for 2 hours. Cells were fixed in methanol at -20 degrees Celsius for 5 min, and blocked with PBS containing 10% goat serum. Cells were stained with anti-PTCH antibody (Santa Cruz Biotechnology, Dallas, TX) overnight at 4 degrees Celsius, washed 3 time in 1XPBS and incubated with an anti-rabbit Alexa-555 secondary antibody for 1 hour at RT. Slides were washed 3 times with PBS and stained with DAPI Prolong Gold (Invitrogen Life Technologies, Grand Island, NY). Slides were analyzed using a Zeiss motorized AxioObserver Z1 microscope.

2.6. Uptake Studies. To measure uptake of the FITC-tagged peptide, cells were plated at a density of 5,000–10,000 cells per well in a 24-well plate and grown overnight. For sphere assays, cells were plated as described above. Cells or spheres

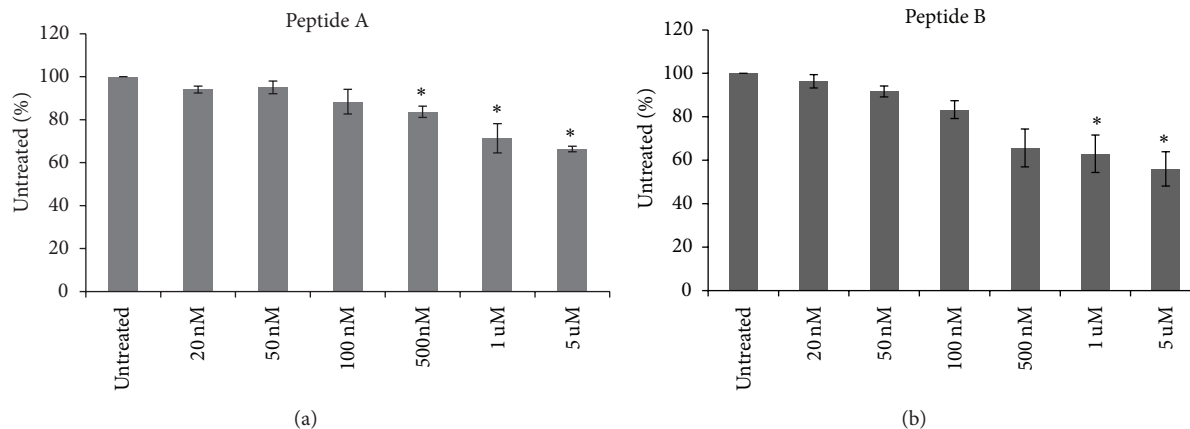


FIGURE 1: Patched-binding peptides decrease growth of the SKBR3 breast cancer cell line. Using the MTT assay, peptides A and B administered to SKBR3 significantly decreased growth compared to untreated cells. Error bars represent standard deviation. Significance is represented by asterisk. * $P \leq 0.05$.

were treated with 100 nM peptide and incubated for 2 hours. Cells or spheres were washed 3X with PBS, trypsinized, and resuspended in 500 μ L culture media. Cells were counted using a Countess automated cell counter (Invitrogen Life Technologies, Grand Island, NY Life Technologies, Grand Island, NY) after staining with trypan blue (Invitrogen Life Technologies, Grand Island, NY Life Technologies, Grand Island, NY). Next, 100 μ L of cell suspension was transferred to black polystyrene 96-well plates. Fluorescence was measured at 485 nm excitation and 535 nm emission. Uptake is reported as mean fluorescence intensity per 1,000 cells.

The rat breast carcinoma cell line 13762 and the human breast cancer cell lines SUM159 and MDA-IBC3 were used for the *in vitro* radiotracer uptake. One day before the uptake experiment, 2×10^5 cells/well of each cell line were seeded in six-well plates and incubated at 37°C in 5% CO₂ under humidified conditions. The following day, 300 kBq of ^{99m}Tc-EC-peptide A or ^{99m}Tc-EC was added with 2 mL of the appropriate media to each of the wells. The cells were incubated for 30 minutes, 1 hour, 2 hours, or 4 hours, after which the media was aspirated, cells were washed twice with PBS, and then cells were suspended with trypsin. Radioactivity of collected cells was measured on a gamma counter (Packard) with an energy window of 126–154 keV for ^{99m}Tc, and percent uptake was calculated by using an appropriate standard. Percent uptake was then normalized to milligrams of protein in the sample, where the protein concentration was measured using the Bradford method (Bio-Rad Laboratories, Berkeley, CA). Each sample was run in triplicate, with error bars indicating standard deviation.

2.7. Animal Model and Chemotherapy Treatment. All animal work was carried out in the Small Animal Imaging Facility (SAIF) at the University of Texas M.D. Anderson Cancer Center under an approved Institutional Animal Care and Use Committee (IACUC) protocol. Female Fischer 344 rats (150 \pm 25 g, $n = 6$) (Harlan Sprague-Dawley, Indianapolis, IN) were inoculated subcutaneously with 0.1 mL of a 13762

breast carcinoma cell suspension (10^5 cells/rat of a breast tumor cell line specific to Fischer rats) into the hind legs using 25-gauge needles. Studies were performed 12–14 days after inoculation when tumors reached approximately 1 cm in diameter. For treatment studies, rats were injected with 20 mg/kg paclitaxel and reimaged 7 days later. After the posttreatment scan, tumors were removed and formalin sections were made. Control tumors were taken from untreated mice 13 days after inoculation. Sections were stained with an anti-patched antibody (Santa Cruz) using a peroxide-based immunohistochemical detection kit (Dako) according to the manufacturer's instructions.

2.8. Planar Imaging. Planar scintigraphic images were obtained using M-CAM (Siemens Medical Solutions, Hoffman Estates, IL) equipped with a low energy high resolution (LEHR) collimator. Anesthetized breast tumor-bearing rats were injected intravenously with ^{99m}Tc-EC-peptide A (0.3 mg/rat, 300 μ Ci/rat; $n = 3$) before and 7 days after paclitaxel treatment. ^{99m}Tc-EC (0.15 mg/rat, 300 μ Ci/rat; $n = 3$) was used as a control. The images were acquired at 1 hr, 2 hr, and 4 hr after administration of radiotracers. Computer outlined regions of interest (ROIs in counts per pixel) between tumor and muscle were used to calculate tumor-to-muscle (T/M) ratios.

2.9. Statistical Analysis. Statistical analysis was performed using Graph Pad Prism 6 software (Graph Pad, La Jolla, CA) using ANOVA or unpaired *t*-test. For all tests, *P* values less than 0.05 were considered to be significant.

3. Results

3.1. Growth Inhibitory Effect of Peptides A and B in Breast Cancer Lines. Inhibition of hedgehog signaling has been shown to decrease growth and survival of breast cancer cells [2, 4]. Antibodies that disrupt the binding of sonic hedgehog to the PTCH receptor have also been reported to inhibit breast

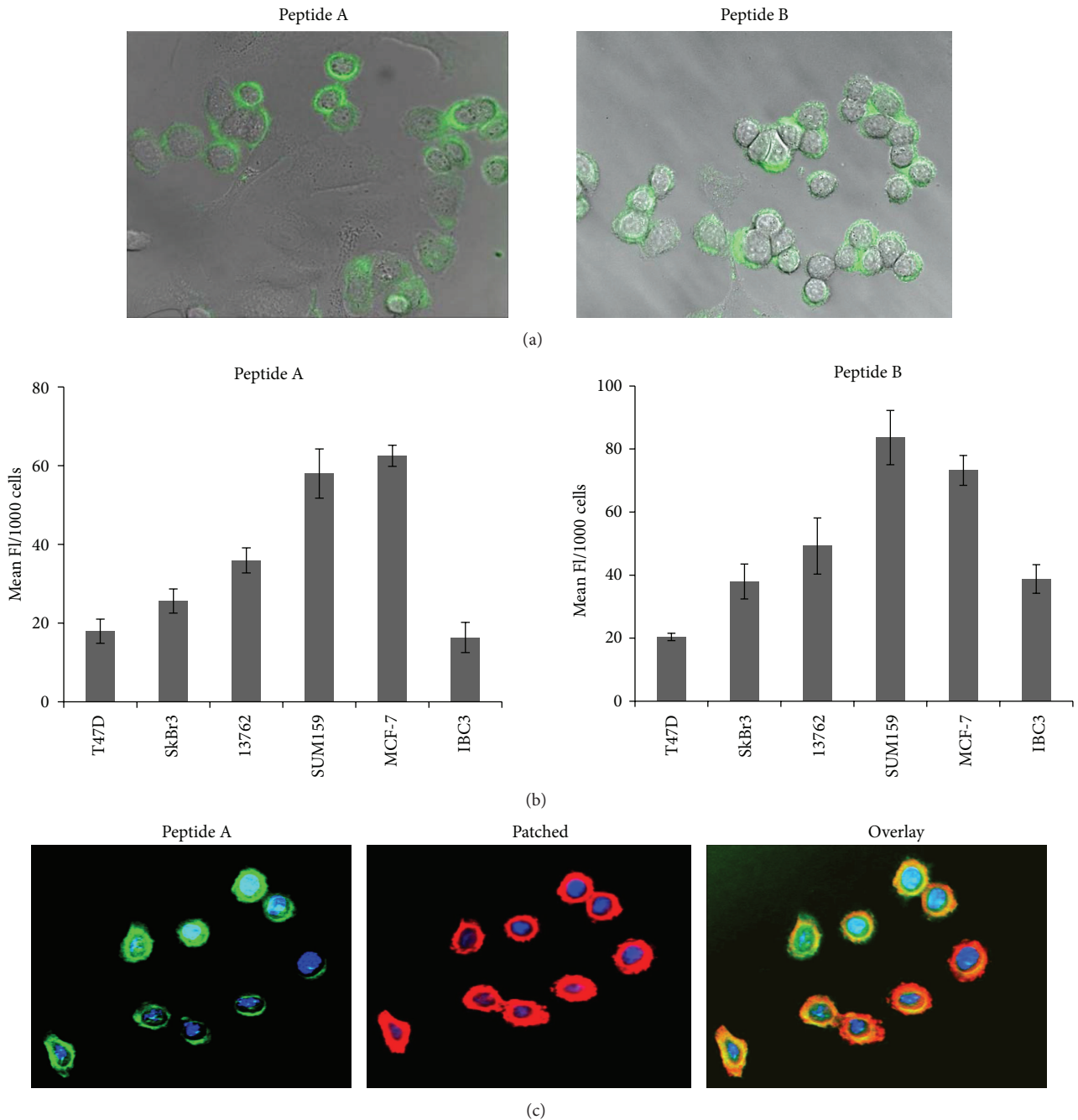


FIGURE 2: Patched-binding peptides have significant uptake in breast cancer cell lines. (a) Fluorescence microscopy of FITC-labeled peptides A and B in SKBR3 breast cancer cells. (b) Quantification of FITC-peptides A and B uptake in breast cancer cell lines. (c) Fluorescence microscopy of SKBR3 cells showing colocalization of peptide B (green) with the PTCH receptor (red). Colocalization appears as yellow staining in the image overlay.

cancer growth [5]. The PTCH-binding peptides, referred to, in this paper, as peptides A and B, have previously been shown to decrease hedgehog-dependent growth of pancreatic cancer cell lines. Therefore, we sought to determine their effect on breast cancer cell lines. As shown in Figure 1, treatment of SkBr3 breast cancer cell lines with peptides A and B resulted in significant growth inhibition at higher concentrations. Minimal effect was observed at lower concentrations.

3.2. Peptide Uptake in Breast Cancer Cell Lines and Mammospheres. To validate the PTCH-binding peptides A and B as ligands to detect breast cancer cells, we evaluated the cellular uptake of the peptides labeled with FITC. Fluorescence microscopy of breast cancer cell lines revealed uptake of the FITC-tagged peptides. As shown in Figure 2(a), cytosolic fluorescence was observed 24 hours after treatment of the breast cancer cell line SKBR3 with peptide A or peptide B. To

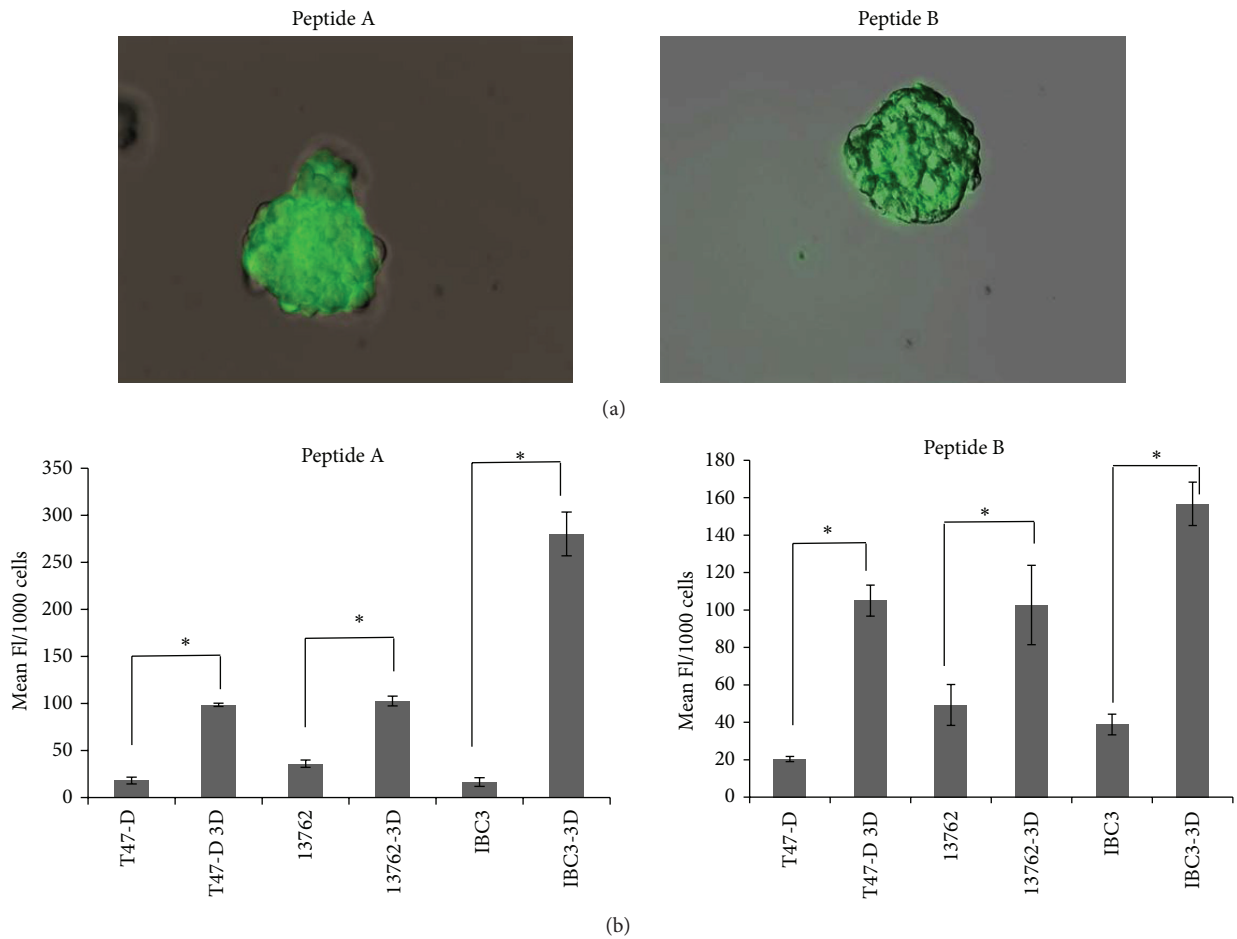


FIGURE 3: Uptake of patched-binding peptides is increased in mammospheres from breast cancer cell lines. (a) Fluorescence microscopy of FITC-labeled peptides A and B in mammospheres from T47-D. (b) Quantification of FITC-peptides A and B uptake in breast cancer cell lines in monolayer and mammosphere cultures. Uptake was significantly higher in cells cultured in mammosphere promoting conditions (3 dimensional cultures) than in those grown in standard monolayer conditions. Significance is represented by asterisk. * $P \leq 0.01$.

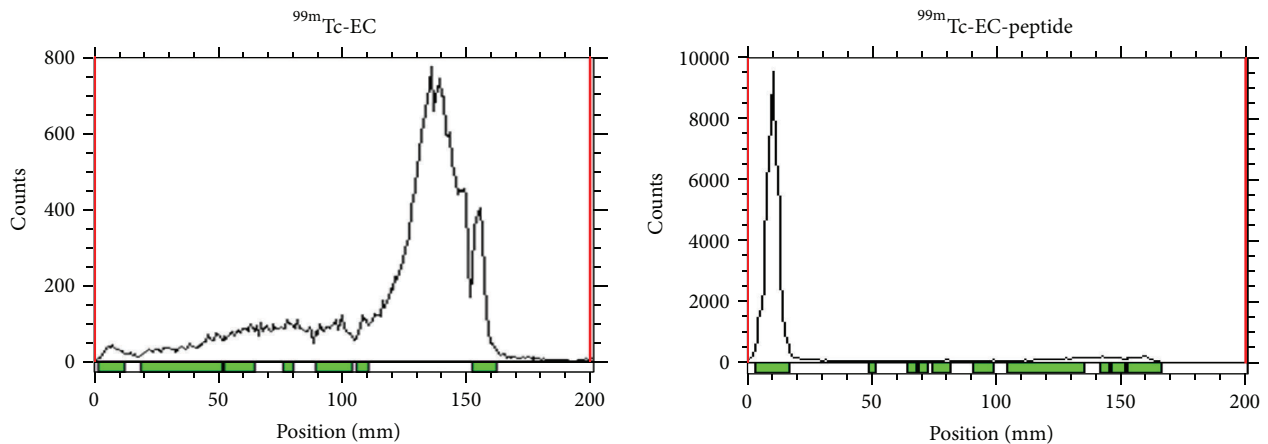


FIGURE 4: Radiochemical purity of $^{99m}\text{Tc-EC}$ and $^{99m}\text{Tc-EC-peptide}$ A. Radiochemical purity was determined by RadioTLC with saline as the mobile phase.

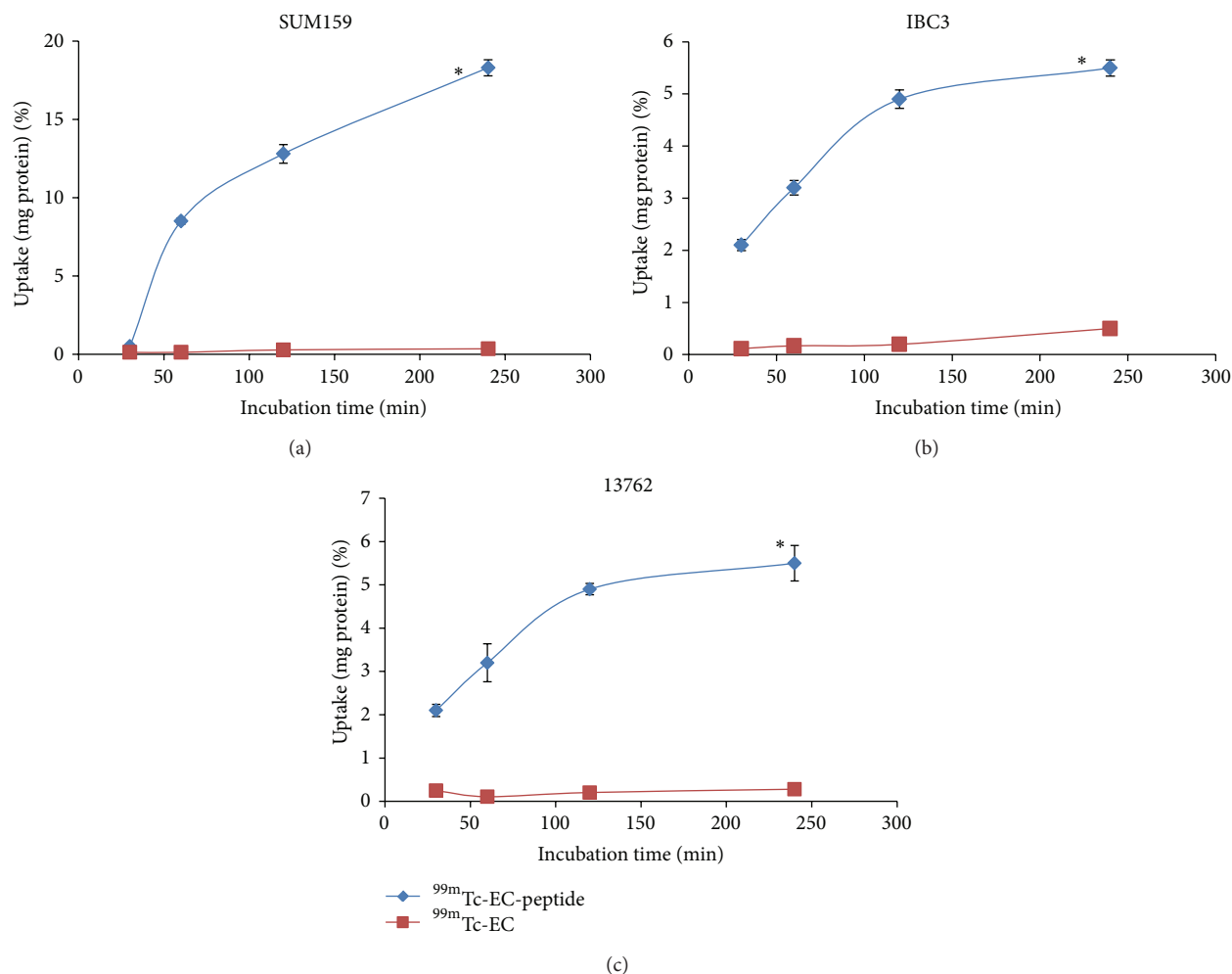


FIGURE 5: *In vitro* uptake of ^{99m}Tc -EC-peptide A. Results of *in vitro* assays showing significant uptake of peptide A compared to ^{99m}Tc -EC control in (a) SUM159, (b) MDA-IBC3, and (c) 13762 breast cancer cell lines. Data is represented as % uptake per mg/protein. Error bars represent standard deviations. Significance is represented by asterisk. * $P \leq 0.001$.

quantify these findings, uptake studies were performed in a panel of breast cancer cell lines and fluorescence intensity was measured. As shown in Figure 2(b), significant uptake of the fluorescent peptides was observed. Furthermore, fluorescent intensity corresponded to PTCH expression as previously reported [1], suggesting that binding is specific to the PTCH receptor. To further confirm colocalization of PTCH-binding peptides with PTCH receptor expression, we performed fluorescence microscopy using anti-PTCH antibodies on cells treated with FITC-labeled PTCH-binding peptides. As shown in Figure 2(c), uptake of PTCH-binding peptides (green) colocalized with PTCH receptor expression (red).

Hedgehog pathway members PTCH, Gli-1, and Gli-2 have been reported to be more highly expressed in normal mammary stem cells and their malignant counterparts, breast cancer stem cells, compared to more differentiated breast cancer cells [6]. High expression of the PTCH receptor has been reported in breast cancer cells cultured in stem cell-enriching conditions (mammospheres, 3 dimensional cultures). Consistent with these findings, an increase in

peptide uptake was observed in mammospheres compared to 2 dimensional monolayer cultures (Figure 3). These data indicate that PTCH-binding peptides may provide a method of targeting breast cancer stem cells.

3.3. Synthesis and Radiolabeling of EC-Peptide A. To establish the uptake of PTCH-binding peptides *in vivo*, we synthesized chelator-peptide conjugates that could be radiolabeled with ^{99m}Tc for gamma scintigraphy. A simple and efficient synthesis of ^{99m}Tc EC-PTCH was developed. EC was conjugated to the lysine residue of peptide A. ^{99m}Tc EC-PTCH was found to be radiochemically pure (100%, Figure 4).

3.4. In Vitro Uptake Studies. *In vitro* cellular uptake of the ^{99m}Tc -conjugated peptide was performed in three breast cancer cell lines: SUM159, MDA-IBC3, and 13762. As shown in Figure 5, cellular uptake of the peptide conjugate was significantly higher than that of the chelator alone in all lines. Similar to the data for the FITC-tagged peptide, the SUM159

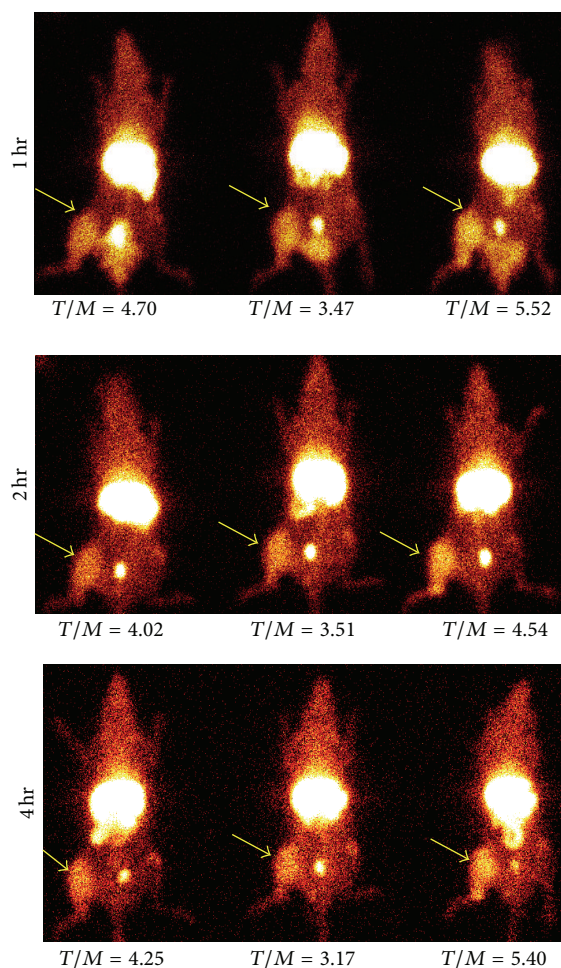


FIGURE 6: *In vivo* uptake of ^{99m}Tc -EC-peptide A in rats bearing 13762 breast carcinoma xenografts. Tumor-to-muscle (T/M) ratios are given for 3 separate rats at multiple timepoints after injection of the radiotracer. Arrows indicate tumor location.

line showed the highest radiotracer uptake with approximately 18% uptake per mg protein at 4 hours (Figure 5(a)). Significant uptake of the radiotracer was also observed in two other lines, increasing steadily in MDA-IBC3 (Figure 5(b)) and reaching saturation after 1-2 hours in 13762 (Figure 5(c)).

3.5. *In Vivo* Imaging. To investigate the utility of peptide imaging of the PTCH receptor in breast cancer, planar scintigraphy was performed in a rat model of breast cancer using ^{99m}Tc -EC-peptide A. Fisher rats were inoculated with the mammary carcinoma cell line 13762, and after tumors grew for two weeks, rats were injected with approximately 300 μCi of the ^{99m}Tc -labeled peptide. Planar scintigraphy was conducted at 1, 2, and 4 hours after injection of the radio-labeled peptide, and tumor-to-muscle ratios were calculated. An average tumor-to-muscle ratio of 4.5 ± 0.07 was obtained at 1 hour. Significant retention of the peptide was observed in the tumor tissue up to 4 hours after injection (Figure 6).

Several studies have reported that hedgehog signaling induces resistance to chemotherapy [4, 7, 8]. Therefore,

we expect that residual cells which remain after treatment with chemotherapy would have high expression of hedgehog pathway members. We examined PTCH expression in tumor xenografts before and after treatment with paclitaxel. As shown in Figure 7(a), an increase in PTCH protein expression is observed in the residual tumor seven days after treatment. Although there was a decrease in tumor volume after treatment, planar imaging with ^{99m}Tc -EC-peptide A revealed no significant decrease in tumor accumulation of the peptide (Figure 7(b)). These findings suggest that PTCH receptor imaging may provide a useful method to assess resistant tumor tissue after chemotherapy treatment.

4. Discussion

Neoadjuvant chemotherapy is commonly prescribed for treatment of invasive or large tumors to allow for breast-conserving surgery. However, there is currently no reliable method to noninvasively follow response to chemotherapy. It is unclear whether the current standard for clinical imaging, ^{18}F -FDG PET, is predictive of treatment response due to false positive results following treatment. *In vitro* and *in vivo* studies have demonstrated high FDG uptake in inflammatory lesions [5]. Increased FDG uptake in macrophages and neutrophils caused by treatment-induced inflammation has also been reported [9, 10].

We show that *in vivo* imaging with ^{99m}Tc -PTCH peptides may offer an alternative method to follow treatment response and allow for tumor-specific imaging prior to and immediately after chemotherapy treatment. Our data suggest that peptides which bind to the ligand docking site of the hedgehog receptor, PTCH, are localized to breast cancers *in vivo*. Furthermore, we show that PTCH receptor expression is increased after paclitaxel treatment in a rat model of breast cancer. These results indicate that PTCH-positive, treatment-resistant cells may be enriched after chemotherapy. In addition to tumor uptake, significant uptake of the peptide was observed in liver and kidney tissues. This may be due to clearance of the peptide and the FITC tag. Additionally, liver uptake may be due to low level endogenous expression of the PTCH receptor by liver tissue. Although our work and that of others [2] suggest that PTCH docking peptides specifically target the PTCH receptor on cancer cells, binding to other cell surface receptors cannot be ruled out.

The cancer stem cell hypothesis states that tumors consist of a heterogeneous population of cells, including both rapidly dividing, differentiated cells that can be effectively targeted by chemotherapy and relatively resistant stem-like cells [11]. Previous studies have reported that breast cancer stem cells express high levels of the PTCH receptor and that hedgehog signaling is required for the growth of these cells [6]. Our data indicate that PTCH-binding peptides have higher uptake in cells cultured under stem cell-promoting conditions (mammospheres) and may serve as a ligand to detect and target this cell population. Additionally, our findings suggest that PTCH receptor-positive cells are resistant to chemotherapy and that ^{99m}Tc -peptide A may be a useful agent for the detection of

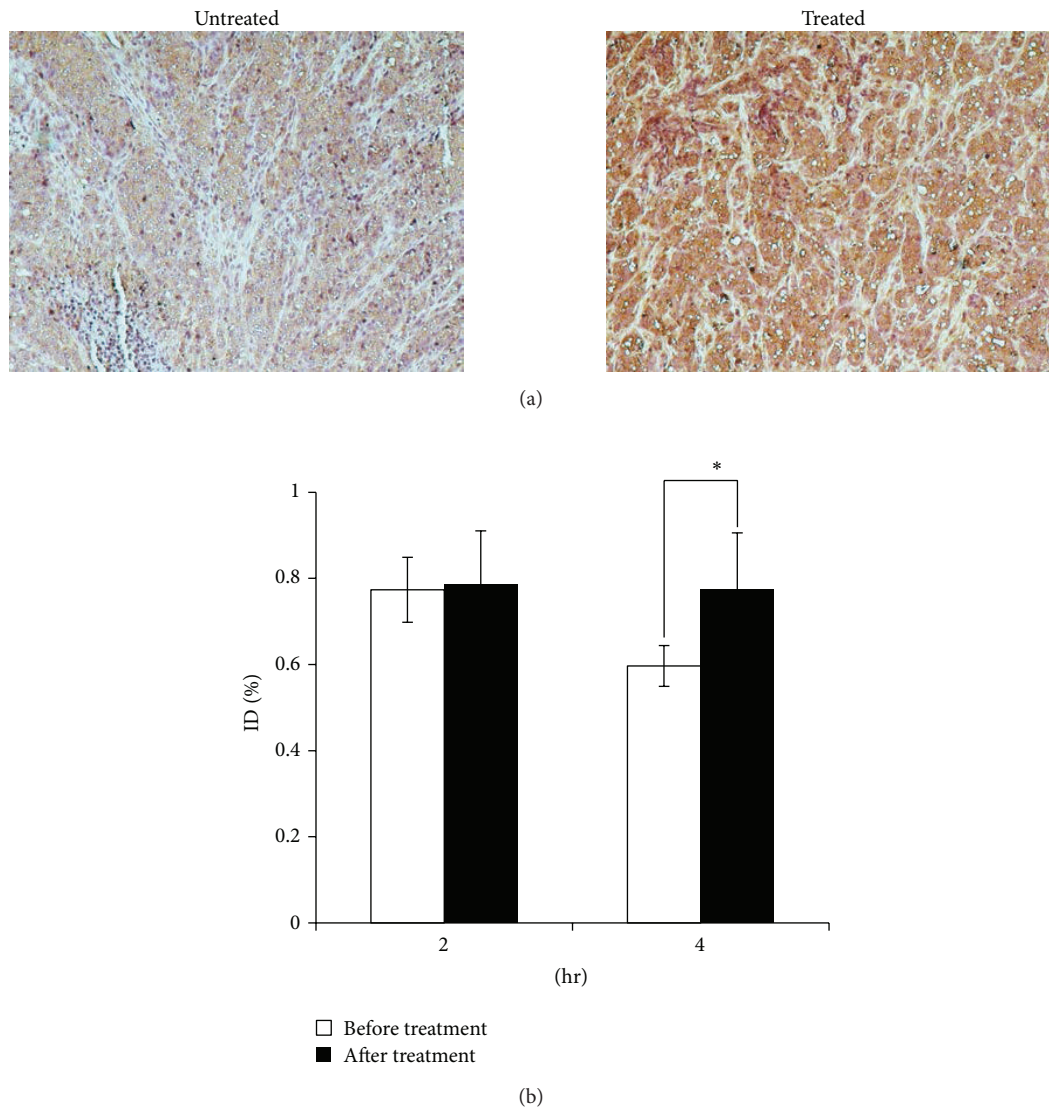


FIGURE 7: PTCH expression is increased in breast cancer xenografts after chemotherapy treatment. (a) Immunohistochemical detection of PTCH before and after treatment with paclitaxel. (b) Tumor uptake of ^{99m}Tc -EC-peptide A is increased after treatment with chemotherapy. Data represents % injected dose in the ROI of the tumor. Error bars represent standard deviation. Significance is represented by asterisk. * $P \leq 0.05$.

treatment-resistant breast cancer cells with active hedgehog signaling.

PTCH-blocking peptides have been shown to decrease growth of pancreatic cancer cell lines [2]. Similar to previous studies, we show that treatment of breast cancer cell lines with PTCH-binding peptides decreases growth of breast cancer cell lines. While our preliminary results suggest that PTCH-binding peptides may slow growth of breast cancer, further study is needed to validate the therapeutic effect. Our data also indicate that further evaluation of the effect of PTCH-binding peptides on tumor detection, growth, and survival in orthotopic models of breast cancer is warranted. These

peptides may serve as useful theranostics which may be used to both image and treat breast cancer.

Conflict of Interests

The authors declare that there is no conflict of interests regarding the publication of this paper.

Acknowledgments

This project was supported by the National Institutes of Health grant U54-GM104941, the NIH/National Cancer

Institute Grant ROI CA138230-01 and the Delaware INBRE program, with a grant from the National Institute of General Medical Sciences—NIGMS (8 P20 GM103446-13).

References

- [1] J. Sims-Mourtada, D. Yang, I. Tworowska et al., “Detection of canonical hedgehog signaling in breast cancer by 131-iodine-labeled derivatives of the sonic hedgehog protein,” *Journal of Biomedicine and Biotechnology*, vol. 2012, Article ID 639562, 8 pages, 2012.
- [2] M. Nakamura, H. Tanaka, Y. Nagayoshi et al., “Targeting the hedgehog signaling pathway with interacting peptides to Patched-1,” *Journal of Gastroenterology*, vol. 47, no. 4, pp. 452–460, 2012.
- [3] D. J. Yang, W. E. Fogler, J. L. Bryant et al., “Assessment of antiangiogenic effect using ^{99m}Tc -EC-endostatin,” *Cancer Biotherapy and Radiopharmaceuticals*, vol. 17, no. 2, pp. 233–245, 2002.
- [4] F. Chai, J. Zhou, C. Chen et al., “The Hedgehog inhibitor cyclopamine antagonizes chemoresistance of breast cancer cells,” *Oncotargets and Therapy*, vol. 6, pp. 1643–1647, 2013.
- [5] S. Law, M. Fok, S. Chow, K.-M. Chu, and J. Wong, “Preoperative chemotherapy versus surgical therapy alone for squamous cell carcinoma of the esophagus: a prospective randomized trial,” *Journal of Thoracic and Cardiovascular Surgery*, vol. 114, no. 2, pp. 210–217, 1997.
- [6] S. Liu, G. Dontu, I. D. Mantle et al., “Hedgehog signaling and Bmi-1 regulate self-renewal of normal and malignant human mammary stem cells,” *Cancer Research*, vol. 66, no. 12, pp. 6063–6071, 2006.
- [7] J. Sims-Mourtada, J. G. Izzo, J. Ajani, and K. S. C. Chao, “Sonic Hedgehog promotes multiple drug resistance by regulation of drug transport,” *Oncogene*, vol. 26, no. 38, pp. 5674–5679, 2007.
- [8] J. Sims-Mourtada, J. G. Izzo, S. Apisarnthanarax et al., “Hedgehog: an attribute to tumor regrowth after chemoradiotherapy and a target to improve radiation response,” *Clinical Cancer Research*, vol. 12, no. 21, pp. 6565–6572, 2006.
- [9] D. R. Jones, L. A. Parker Jr., F. C. Detterbeck, and T. M. Egan, “Inadequacy of computed tomography in assessing patients with esophageal carcinoma after induction chemoradiotherapy,” *Cancer*, vol. 85, pp. 1026–1032, 1999.
- [10] G. Zuccaro Jr., T. W. Rice, J. Goldblum et al., “Endoscopic ultrasound cannot determine suitability for esophagectomy after aggressive chemoradiotherapy for esophageal cancer,” *The American Journal of Gastroenterology*, vol. 94, no. 4, pp. 906–912, 1999.
- [11] G. J. Lindeman and J. E. Visvader, “Insights into the cell of origin in breast cancer and breast cancer stem cells,” *Asia-Pacific Journal of Clinical Oncology*, vol. 6, no. 2, pp. 89–97, 2010.

Research Article

Design of CGMP Production of ^{18}F - and ^{68}Ga -Radiopharmaceuticals

Yen-Ting Chi, Pei-Chun Chu, Hao-Yu Chao, Wei-Chen Shieh, and Chuck C. Chen

PET Pharm Biotech Company Limited, 1-2F No. 143 and 1-2F No. 141 HouGang, Xinzhuang District, New Taipei City 24257, Taiwan

Correspondence should be addressed to Chuck C. Chen; chuck@bqsv.com

Received 1 July 2014; Accepted 17 July 2014; Published 2 September 2014

Academic Editor: David J. Yang

Copyright © 2014 Yen-Ting Chi et al. This is an open access article distributed under the Creative Commons Attribution License, which permits unrestricted use, distribution, and reproduction in any medium, provided the original work is properly cited.

Objective. Radiopharmaceutical production process must adhere to current good manufacturing process (CGMP) compliance to ensure the quality of precursor, prodrug (active pharmaceutical ingredient, API), and the final drug product that meet acceptance criteria. We aimed to develop an automated system for production of CGMP grade of PET radiopharmaceuticals. **Methods.** The hardware and software of the automated synthesizer that fit in the hot cell under cGMP requirement were developed. Examples of production yield and purity for ^{68}Ga -DOTATATE and ^{18}F -FDG at CGMP facility were optimized. Analytical assays and acceptance criteria for cGMP grade of ^{68}Ga -DOTATATE and ^{18}F -FDG were established. **Results.** CGMP facility for the production of PET radiopharmaceuticals has been established. Radio-TLC and HPLC analyses of ^{68}Ga -DOTATATE and ^{18}F -FDG showed that the radiochemical purity was 92% and 96%, respectively. The products were sterile and pyrogenic-free. **Conclusion.** CGMP compliance of radiopharmaceuticals has been reviewed. ^{68}Ga -DOTATATE and ^{18}F -FDG were synthesized with high radiochemical yield under CGMP process.

1. Introduction

1.1. Trends in Radiopharmaceutical Development. Molecular imaging agents play a major role in drug discovery and development because of their ability to quantify drug properties *in vivo*. Among molecular imaging modalities, positron emission tomography (PET) imaging agents are the most sensitive and could provide target specific information. PET agents show high specific activities since they are made through a nuclear transformation and used carrier free forms of isotopes. PET agents do not produce detectable pharmacologic effects but provide important information concerning the characterization of various diseases. PET agents are able to assist in the determination of optimal therapeutic dosing, delineate differential diagnosis between responder and nonresponder, and predict treatment response by selecting patient who may respond to therapy.

There are two categories in PET radiochemistry. The first category is known as covalent chemistry using cyclotron-produced organic isotopes such as ^{18}F or ^{124}I to incorporate

into molecules. For instance, ^{18}F -fluorodeoxyglucose (FDG), a gold standard for PET, has been successfully used to image diseases with high glycolysis. However, FDG has several limitations that give rise to false positive/negative diagnosis and poor predictive value of chemoradiation therapy to tumor response [1]. In addition, certain tumors such as neuroendocrine type tumors have poor uptake of FDG. Therefore, there is a high demand to develop new radiopharmaceuticals beyond FDG in oncology field. In contrast with cyclotron-produced isotopes, the second category employs coordination chemistry using metallic radionuclides produced from generators. A generator uses a parent-daughter nuclide pair wherein a relatively long-lived parent isotope decays to a short-lived daughter isotope for imaging. The parent isotope, which is produced at a cyclotron facility, can be shipped to a clinical site and is the source from which the daughter isotope is readily eluted. ^{68}Ga -based (68-minute half-life, $\beta^+ = 89\%$ and $\text{EC} = 11\%$) PET agents are with significant commercial potential because the isotope can be produced from a $^{68}\text{Ge}/^{68}\text{Ga}$ generator (275-day half-life or 18-month shelf

life) on site and is a convenient alternative to cyclotron-produced PET isotopes, such as ^{18}F or ^{124}I . The short half-life of ^{68}Ga permits applications with suitable radioactivity while maintaining patient dose to an acceptable level. Furthermore, $^{68}\text{Ga}^{3+}$ can form stable complexes with many ligands containing oxygen and nitrogen as donor atoms. This makes ^{68}Ga suitable for chelation in various molecules. Over the last three decades, several $^{68}\text{Ge}/^{68}\text{Ga}$ generators have been proposed in an attempt to provide high yield of ^{68}Ga and low breakthrough of ^{68}Ge . The efforts in image-guided therapy, theranostic (image and therapy) approaches, pivotal clinic trials, and integration with system biology findings on genomic and proteomic expressions are the trends for PET agent development in patient care management.

1.2. Need for Automated Synthesis of PET Radiopharmaceuticals. Radiopharmaceutical chemistry requires intricate handling of radioactive materials, fast reaction times, ease of synthesis, and reproducible results. In the preclinical setting, radiopharmaceuticals are typically synthesized manually. Such applications use *in vitro* and small animal models to validate the agent and require low levels of radioactivity. The use of manual synthesis for clinical imaging, however, is challenging for multiple reasons: (1) clinical agents must meet strict sterility and pyrogenicity requirements which are validated from batch to batch; (2) batch-to-batch reproducibility is required to demonstrate suitable radiochemical yield, radiochemical purity, and other quality control analyses; (3) synthesis time must be fast when dealing with radionuclides with a short half-life; (4) clinical studies require multiple patient doses and would expose radiochemists to much higher levels of radioactivity; and (5) production cost and availability of the technology may limit the viability of the agent in routine clinical practice. The Food and Drug Administration (FDA) permits radiopharmaceuticals produced under well-controlled conditions in central commercial facilities to be distributed to local clinics where they are administered. In addition, radionuclide generator systems produced in well-controlled facilities have gained FDA acceptance and have a long history of successful clinical application. The competitive advantage of generator-based agents lies in their convenient synthetic schemes; however, this attribute is greatly diminished if the tracers lack clinical usefulness. An automated apparatus is needed to assure production efficiency and minimize the radiation exposure by PET isotopes. Regardless of classification, all medical devices are subject to general controls and baseline requirements of the Food, Drug and Cosmetic (FD&C) Act as well as the provisions and standards contained in the USP General Chapter <823> *Radiopharmaceuticals for Positron Emission Tomography-Compounding* and General Chapter <1015> *Automated Radiochemical Synthesis Apparatus*. It is, therefore, critical to consider these guidelines while designing the building blocks of the automated apparatus.

1.3. Current Good Manufacturing Practice (CGMP) Compliance in Automated Radiopharmaceutical Production. Radiopharmaceutical production process must adhere to CGMP

compliance to ensure the quality of precursor, prodrug (active pharmaceutical ingredient, API), and the final drug product that meet acceptance criteria. The FDA Modernization Act of 1977 (Section 121) requires the FDA to establish approval procedures and cGMP for PET drugs. In 2002, the FDA published a guideline called “Chemistry, Manufacturing, and Controls” dealing with three common PET drug products (i.e., ammonia ^{13}N , ^{18}F -FDG, and sodium fluoride ^{18}F injections) [2]. Even though these guidelines do not apply directly to ^{68}Ga , they play important roles in our design review. The FDA has released the CGMP requirements (to be CFR 21 Part 212) and guidance documents for PET drug products on September 15, 2005. The cGMP regulations are the minimum set of requirements for a facility to develop commercial use agents and will be complied with during the commercialization of the automated synthesizer as they apply. The following documents, as outlined in the cGMP guidance, are relevant for putting together the design specifications, installation, verification, and maintenance protocols for the automated synthesizer.

- (i) FDA. *Part 210—Current Good Manufacturing Practice in Manufacturing, Processing, packing or Holding of Drugs*. August 1996.
- (ii) FDA. *Part 211—Current Good Manufacturing Practice for Finished Pharmaceuticals*. August 1996.
- (iii) FDA. *Guide to Inspection of Computerized Systems in Drug Processing*. February 1983.
- (iv) FDA. *General Principles of Process Validation*. May 1987.
- (v) FDA. *Sterile Drug Products Produced by Aseptic Processing*. June 1987.
- (vi) FDA. 21 CFR Part 11; *Electronic Records; Electronic Signatures*. FR Notice 7/21/99 (64 FR 39146).
- (vii) U.S. Pharmacopeia. <823> *Radiopharmaceuticals for Positron Emission Tomography-Compounding*. USP 26, NF 21, 2003.
- (viii) U.S. Pharmacopeia. <1015> *Automated Radiochemical Synthesis Apparatus*. USP 26, NF 21, 2003.

The specific steps for quality assurance and validation are specified in these documents.

- (i) U.S. Pharmacopeia. <1> *Injections*. USP 26, NF 21, 2003.
- (ii) U.S. Pharmacopeia. <71> *Sterility Tests*. USP 26, NF 21, 2003.
- (iii) U.S. Pharmacopeia. <85> *Bacterial Endotoxins Test*. USP 26, NF 21, 2003.
- (iv) U.S. Pharmacopeia. <621> *Chromatography*. USP 26, NF 21, 2003.
- (v) U.S. Pharmacopeia. <821> *Radioactivity*. USP 26, NF 21, 2003.

The CGMP compliance covers manufacturing process and facility, quality guidelines, and personnel training. The

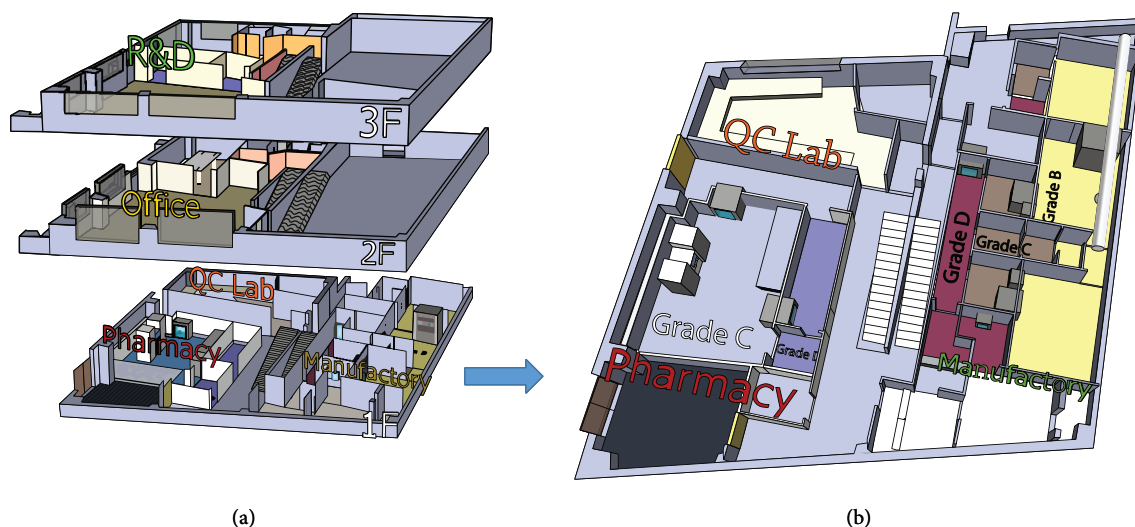


FIGURE 1: Design of a CGMP facility ((a) a three-floor design containing CGMP process at level 1, data management at level 2, and research development at level 3; (b) an expanded diagram of CGMP facility) at PET Pharm Biotech.

Pharmaceutical Inspection Convention and Pharmaceutical Inspection Co-operation Scheme (jointly referred to as PIC/S) are two international instruments between countries and pharmaceutical inspection authorities, which provide together an active and constructive cooperation in the field of Good Manufacturing Practice (GMP). PIC/S's mission is to lead the international development, implementation, and maintenance of harmonized GMP standards and quality systems of inspectorates in the field of medicinal products (<http://picscheme.org/>). At PET Pharm Biotech firm, we have adopted PIC/S guideline and USP 797 guidance for the production, formulation, and dispensing of PET radiopharmaceuticals. Current regulations and quality standards including FDA regulations and CFR, EU-GMP guidelines, WHO-GMP guidelines, and roles of PIC/S in international regulatory affairs are well documented in online resources. Our team has designed, built, and validated an automated bench-top system for PET radiopharmaceuticals. Here, we report two agents: ^{18}F -FDG and ^{68}Ga -DOTATATE. The guidance documents were from the FDA relevant CFR 21 part 212, "Current Good Manufacturing Practices for Positron Emission Tomography Drug Products" Final Guidance for Industry and FDA Staff, Center for Devices and Radiological Health, March 2002. We adhere to FDA and PIC/S guidelines for the synthesis of radiopharmaceuticals included in the USP 797 to ensure that the products can be produced using our system under the required conditions.

1.4. Materials and Methods. Entered via a series of small rooms increasing in the cleanliness grades, a grade B final gowning room opens to two grade B production rooms (Figures 1 and 4). In each production room (12 m²), stands one custom-made hot cell (BqSv, Inc., Taiwan) with two main compartments. The synthesis compartment is maintained in the same level of cleanliness as the room while the aseptic filling compartment is a grade A isolator. Inside this grade A

isolator, the particle counts are monitored continuously during filling of the final product by a semiautomatic apparatus and inlet is installed for hydrogen peroxide disinfection.

1.5. Key System Features during the Design Phase for ^{68}Ga -Agent

- (i) *Turnkey* solution to fully automate the process including syringe drives to elute generator and inject reagents into the vessels, N₂ gas regulator, and vacuum pump.
- (ii) *Purification* of ^{68}Ga by eluting ^{68}Ga from the generator before synthesis to produce clinical-grade ^{68}Ga using a purification cassette, a vial for collection and concentration of peak fraction of elution, an ion exchange column to trap ^{68}Ga , and a vial for waste collection of ^{68}Ge monitored by a collimated radiation detector.
- (iii) *Formulation* of ^{68}Ga conjugation with precursor and proper dilution for injection: this panel will have a disposable cassette, a smart reaction vessel receiving the clinical-grade ^{68}Ga from the purification panel, and an infrared heater.
- (iv) *Disposable cassettes* for 100% tubing replacement to eliminate possible contamination between runs.
- (v) *Automated dispensing* of reagents and solution via programmable syringe drives.
- (vi) *Real-time monitoring* of sample preparation and radioactivity at several points of the system using a real-time display.
- (vii) *Breakthrough monitoring* of ^{68}Ge (parent of ^{68}Ga) at the purification panel.

(viii) *Data recording* of all experimental data (including pressure, temperature, mass flow, reagents nature, and quantities) in tab delimited ASCII format that is readable in Microsoft Excel. Also, recording of the elution profile of the ^{68}Ga generator is desired.

1.6. Development of the Hardware and Mechanical to Fit in Hot Cell. This task includes the detailed mechanical design of the Scintomics module basic system. This activity was composed of the following tasks.

- (1) Develop the overall mechanical system layout.
- (2) Identify the mechanical subassemblies and produce drawings of the resulting high-level mechanical architecture.
- (3) Conduct a review of the high-level mechanical architecture.
- (4) Complete the detailed design of the mechanical sub-systems.
- (5) Produce detailed mechanical drawings and bills-of-material.
- (6) Identify critical and long lead-time components.
- (7) Place orders for individual parts, commercially available subassemblies, and vendor fabricated items.
- (8) Mechanically assemble the basic system instrument module.
- (9) Verify the mechanical assembly.

1.7. Development of the Hardware: Electronics. This activity includes the design of any electronics needed to support the operation of any sensors, motors, or other electronic devices used in the implementation of the basic system instrument module. This activity was composed of the following tasks.

- (1) Develop the high-level architecture of the Scintomics module system electronics.
- (2) Identify devices needing the design of custom interface circuitry.
- (3) Conduct an internal review of the high-level electronics architecture.
- (4) Complete the detailed design of all electronic sub-systems.
- (5) Produce circuit diagrams, complete the design of any necessary custom PCB's, and produce the corresponding bills-of-material.
- (6) Identify critical and long lead-time items.
- (7) Place orders for individual parts, PCB's, and off-the-shelf components.
- (8) Assemble the module electronics and perform preliminary troubleshooting.
- (9) Install the module electronics into the module's mechanical assembly.

1.8. Development of QA Tests for PET FDG or ^{68}Ga -DOTATATE Measurements. Prior to clinic studies, we also conduct testing for the membrane filter integrity, pH, sterility, and pyrogenicity of drug product. The QA criteria are described below.

- (i) *Appearance:* Solution must be colorless and free from particulate matter. The solution inside the collection vial before final release into the collection vial can be recorded by the Web-Cam. Lighting conditions must be consistent and optimal for this test. Test must be completed before release of the drug product.
- (ii) *Radiochemical purity/yield:* Radiochemical purity was assessed by HPLC and radio-TLC. The TLC chromatogram (silica gel coated plates) was scanned for distribution of radioactivity in a radio-TLC scanner. Using saline as the mobile phase, ^{68}Ga -DOTA migrates near the solvent front, while ^{68}Ga -DOTATATE remains at the origin. The retardation factor (R_f) values were determined. HPLC was carried out on a system consisting of two pumps, an injector and a variable UV/Vis detector, and a sodium iodide crystal detector. We have used UV absorbance 210 nm to assess the purity of the compound. HPLC was performed on a C-18 reversed phase column (C-18 Radial-Pak column, 4.6×150 mm, Waters, Milford, MA) with a mobile phase of water/acetonitrile, 70 : 30, using a flow rate of 0.25 mL/min. Findings were used to determine the specific activity of the final product. Tests must be completed before release of the drug product.
- (iii) *Radiochemical stability of ^{68}Ga -DOTATATE* in serum and saline was tested using HPLC and radio-TLC up to 4 hours. Test must be completed before release of the drug product.
- (iv) *Radionuclide purity:* A coaxial high purity germanium (HPGe) detector with a multichannel analyzer (MCA) (Canberra, DSA 2000, GC 8021) was used. This HPGe has an 80% relative efficiency, 1.8 keV FWHM at 1.33 MeV, and an energy range of 100 keV–10 MeV. Energy calibration was done using three NIST-traceable sources (^{137}Cs (11.34 uCi 15/3/01, $T_{1/2}$ 30.17 yrs), ^{60}Co (21.34 uCi on 15/3/01, $T_{1/2}$ 5.27 yrs), and ^{133}Ba (10.13 uCi 8/1/01, $T_{1/2}$ 3862 days)). The acceptance criteria for the radionuclide purity are that no less than 99.5% of the observed γ -emissions measured by HPGe should correspond to the gamma emission signature of ^{68}Ga [3].
- (v) *Radionuclide identity:* The half-life is determined by measuring the radioactivity decay of the sample over about 100 min period. The accepted tolerance is ± 5 min (^{68}Ga —half-life is 68 minutes). A NIST-traceable dose calibrator Capintec Dose Calibrator (CRC-15R) with CRC-2401 Vial/Syringe Dipper (Capintec Inc., Ramsey, NJ) was used to determine the half-life.

- (vi) *Assay for radioactivity*: NIST-traceable dose calibrator (Capintec Dose Calibrator: CRC-15R) with CRC-2401 Vial/Syringe Dipper (Capintec Inc., Ramsey, NJ) was used to determine total activity (MBq or mCi) and the radioactivity concentration (MBq or mCi/mL). The dial setting for ^{68}Ga provided by the vendor (dial setting = 416) was verified by a NIST traceable $^{68}\text{Ge}/^{68}\text{Ge}$ standard source (100 microCi, quoted activity uncertainty $\pm 4\%$); alternatively the ^{18}F dial setting can be used multiplied by (100/89) to correct for abundance difference between ^{18}F (100%) and ^{68}Ga (89%). A ^{90}Sr constancy source (Atlantic Research Co Model B-1 S/N 252) was used to insure proper response of the Capintec dose calibrator during data collection. The ^{90}Sr source was used once per month to check the well chamber response.
- (vii) *Radiochemical impurity*: No more than 5% of unbound radioactivity must be present in ^{68}Ga -DOTATATE injections. Impurity level should depend on its effect on image quality and/or patient radiation absorbed dose. Test must be completed before release of the drug product.
- (viii) *Specific activity*: HPLC was used to determine specific activity. The acceptable criteria will be 0.1–1.0 Ci/ μmole for ^{68}Ga -DOTATATE.
- (ix) *pH*: pH limits are 5.5–8.0. pH meter with pH reference standards was used. Test must be completed before release of the drug product.
- (x) *Chemical purity*: the purity of precursor (DOTATATE) was determined by proton NMR and elemental analysis. This test is done once per batch of precursor.
- (xi) *Residual solvents*: no more than 0.04% acetonitrile and 0.5% dehydrated alcohol were to be present in the drug injection. Testing was performed using a gas chromatography system with flame ionization detection. Test must be completed before release of the drug product.
- (xii) *Bacterial endotoxins*: No more than 175/V USP EU per milliliter of the drug injection, in which V is the maximum recommended total dose, in millimeters, at the expiration time is used. Test must be completed before release of the drug product.
- (xiii) *Sterility*: Sterility testing must be initiated within 24 hrs of preparation. To assure sterility, each batch of product was tested using culture vials with aerobic and anaerobic materials (NR6 and NR7, Becton Dickinson Diagnostic Instrument Systems Towson, MD). Drug solution (0.3 mL) was incubated with Bactec culture vials for 7 days at 37°C . Sterility was assayed by visualizing the cloudiness of the solution.

Additionally, manual testing was conducted to further characterize the generator to determine the following.

- (i) *Elution efficiency*: The ^{68}Ga elution efficiency in full 5 mL aliquots was determined using the dose calibrator and

$$\text{Elution_Eff\%} = \frac{{}^{68}\text{Ga} (10 \text{ mL} \cdot \text{aliquots}) [\text{Bq}]}{{}^{68}\text{Ga}_{\text{loaded}} (\text{decay_corrected}) [\text{Bq}]} \quad (1)$$

$$\times 100\%.$$

Elution efficiency was measured for 1, 3, and 7 hr time periods in between elutes over the life cycle of the generator. Meyer et al. reported that their Russian TiO_2 generator elution efficiency decreased from 90% at the first elution to 60% after 8 months and >500 elutes [4]. They estimated ^{68}Ge loss due to breakthrough that contributed to <1% of this efficiency loss. Possibly, the decrease in elution efficiency is due to alteration in the column structure. Velikyan et al. used also the Russian TiO_2 generator and reported similar loss of elution efficiency, down to 41% after 29-month use [5].

- (ii) *Trace-metal content/purification of elution*: Trace metal ions were analyzed using an Inductively Coupled Plasma-Atomic Emission Spectra (ICP-AES) procedure. We propose obtaining this analysis once every 6 months over the project period ($n = 3$) to observe the metal content of elute as the generator ages. A daily elution of the generator is recommended in order to keep the concentration of metal ions as low as possible.

2. Results

PET Pharm Biotech firm has three connecting laboratories and a room for quality assurance. The lab has been designed and equipped to perform CGMP radiolabeling of different isotopes and molecules (Figure 1). The drug product is synthesized and dispensed in hot cells (Figure 2). Radiation survey meters are mounted in CGMP facilities to monitor radiation exposure (Figure 3). There is a system established to monitor temperature, humidity, radiation dose rate, and air pressure in CGMP facility. The ventilation control system has chambers to collect waste gas as well as to vent through hot cell. The quality assurance lab consists of Millipore water filtration system for all chemical, biological, and radiological experiments, -80°C freezer, -20°C freezer, explosion proof refrigerator, vacuum pump, analytical balance, freeze-dryer, incubator, a Gamma Counter, Capintec dose calibrator, multichannel analyzer, gas chromatography, high performance liquid chromatography (HPLC) system with UV and radioactive flow detectors, radio-TLC scanner, and Survey meter with GM detector. Our system covers the design, monitoring, and control of manufacturing processes and facilities, maintenance, calibration, and validation of equipment, condition of facilities, qualifications and training of employees, reliability and reproducibility of processes, test method validation, handling of complaints, and system inspection and auditing. The staff maintains resources to the highest technical degree. There are different routes and

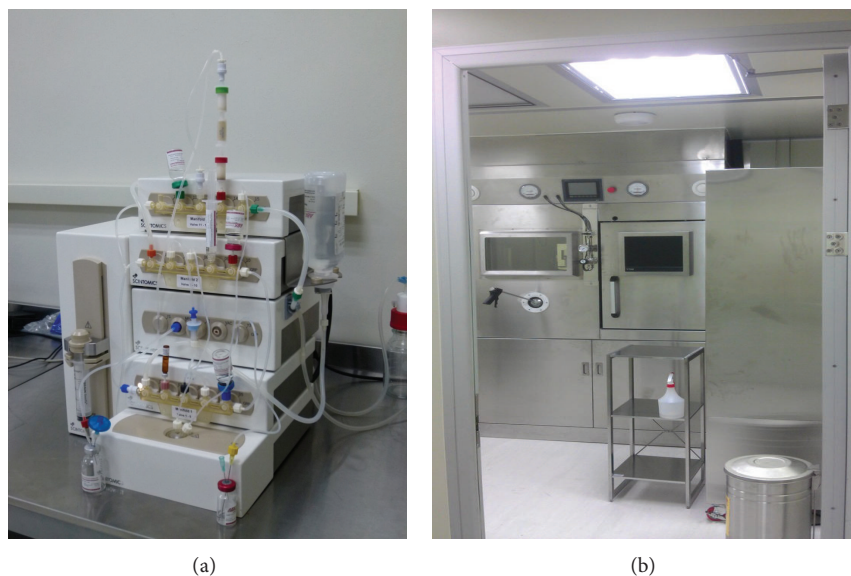


FIGURE 2: An automated synthesizer (a) is housed in a hot cell (b) for CGMP production of PET drug. Adjacent to the hot cell is the cell for dispensing of PET drug.

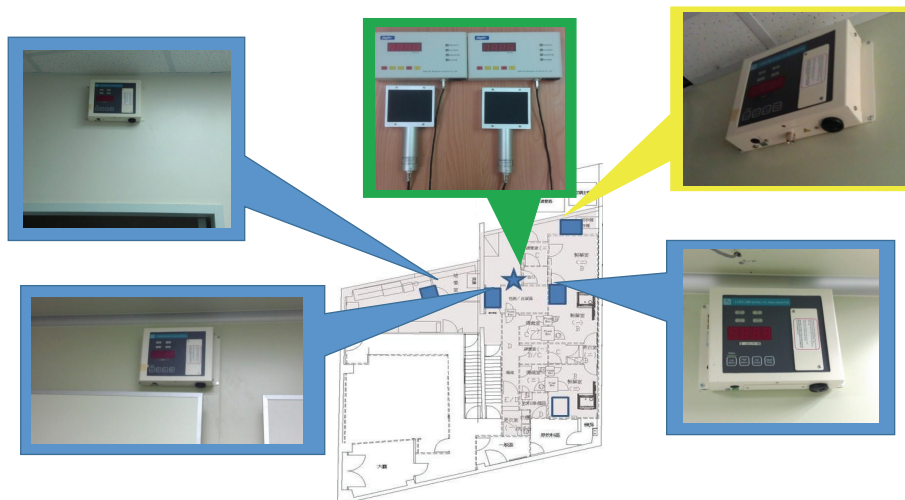


FIGURE 3: Radiation survey meters are necessary to measure radiation dose rates in the CGMP facilities.

grades for operators and drug delivery in CGMP facility (Figure 4). A conventional PET drug production room (in grade C cleanliness) usually has multiple hot cells enclosing various synthesis modules. Each module then is connected by a dedicated tubing and through it the formulated product is pumped to a distant hot cell (grade A) located in a separate room (grade B) for aseptic filling. Here, we present a new concept for the design of a radiopharmacy and have also constructed one accordingly. With this design, we argue that multiple small grade B rooms each set up with a hot cell encasing one grade B synthesis compartment and one grade A aseptic filling compartment would be a more efficient way for complying the most current GMP, especially in a radiopharmacy where more than one kind of PET drugs is regularly produced and dispensed (Figure 1).

Our current facility fulfills PIC/s GMP Guideline and USP (797) Guideline. We have reserved sites for production of different radiopharmaceuticals. Housing an automated module in our hot cell is also compliant with cGMP and FDA 21 CFR part 11 requirements. Our system is capable of detection of radioactivity during radiopharmaceutical production. For quality control (QC) and quality assurance (QA), we have established the criteria for control of the raw materials, analytical quality control, drug product stability testing prior to clinic distribution, and data integrity. For validation process, we have established the reference standard, equipment, and facilities validation and analytical method validation. A dose calibrator and chromatographic analysis were used to assess product quality. The general acceptance criteria for PET drug product especially ^{18}F -agent

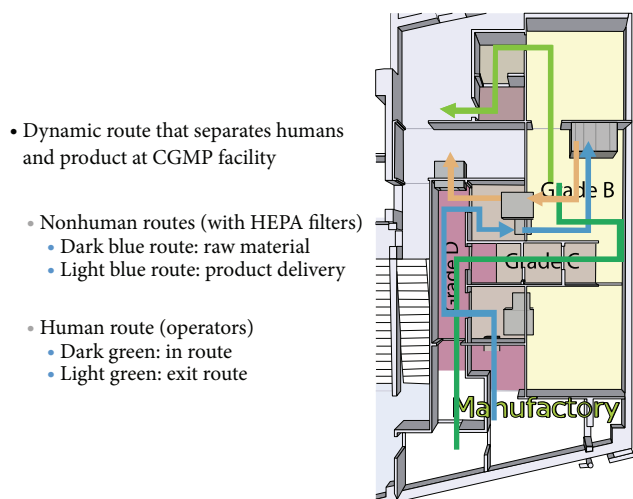


FIGURE 4: Human and nonhuman routes designs are separated in the CGMP facility.

TABLE 1: USP and EP criteria for release of PET drug product.

PET drugs	
pH value	Endotoxin test
Radiochemistry purity	Sterility test
Radiochemistry identity	Stability test
Radionuclide purity	Residual solvents test
Radionuclide identity	Kryptofix 222 test (for FDG)
Concentration of activity	

are shown in Table 1. For the ⁶⁸Ga-DOTATATE labeling, the radiochemical purity of final product in our system was greater than 96%, with decay-corrected radioactive yields of 80%. The total synthesis time reported is 20 minutes, including elution time. The temperature and pressure profiles during the process were examined for consistency.

The concerned cleanroom area is including buffer, final gowning, raw materials and products in-and-out, and two production rooms. With each production room only 12 m², one hot cell, and maximum two operators, grade B is easily maintained. The regular and frequent disinfection practice required for the grade B room is also achieved without any difficulties. Within hot cell, the two compartments are adjacent and, thus, the product transport line is short enough to allow the use of prepackaged disposable sterilized tubing. Importantly, two production rooms can be in operation simultaneously with the diminished risk of cross contamination. The government (Taiwan) auditors have deemed this design in compliance with PIC/S GMP requirements.

3. Discussion

Due to the preferential accumulation of ¹⁸F-FDG in tumor cells, FDG-PET can provide valuable information for tumor diagnosis. In contrast to conventional imaging modalities, FDG-PET can detect lesions with high glucose metabolism

regardless of their anatomical shape or location and, therefore, can distinguish between posttherapy changes and foci of residual active disease. FDG-PET has been shown to be more accurate for the diagnosis and staging of tumors than conventional imaging methods in clinical trials [6–8]. Unfortunately, FDG has not been as advantageous for imaging neuroendocrine tumors (NETs) and only tumors with high proliferative activity and low differentiation have shown an increased FDG uptake [9].

The incidence of NETs has increased over the past several decades, due in part to improvements in discovering them at a localized stage using imaging. While the early detection of NETs allows for potentially curative treatment, the five-year survival rate for patients is less than 80% due to recurrence. The abundant expression of somatostatin receptors (sst2) is a characteristic of NETs. Several analogues are used for peptide receptor radionuclide therapy (PRRT) and ¹¹¹In-octreotide scintigraphic imaging or PET of NET. Sensitivity of PET demonstrated its superiority over scintigraphy, MRI, and CT. The efficiency of a somatostatin analogue depends on its specific binding profile. Recently, reports have shown that ⁶⁸Ga-DOTATOC PET improves staging of NETs by PET and target definition for fractionated stereotactic radiotherapy in patients with intracranial meningiomas [10, 11]. The affinity of ⁶⁸Ga-DOTATATE in binding sst2 (0.2 ± 0.04 nM) has been determined to be approximately 10-fold higher than that of ⁶⁸Ga-DOTATOC (2.5 ± 0.5 nM) [12]. Existing data show that the ⁶⁸Ga-DOTATATE PET represents a major improvement compared to the current standard in NETs imaging. For instance, on the ⁶⁸Ga-DOTATATE PET/CT scan, intense uptake raising suspicions for recurrent NET was observed [13]. Here, we use ⁶⁸Ga-DOTATATE for imaging NETs due to its known affinity and exciting clinic trial results.

Cross contamination among different drug products and procedures is one of the major issues that PIC/S GMP requirements designed to avoid. Yet most PET radiopharmacies in their effort to comply with these rules still set up their production rooms with multiple hot cells so various PET drugs could be produced on the same day even simultaneously. To make the matters worse, these different products often share the same aseptic filling space. Though the production rooms are only required to maintain for grade C cleanliness, the grade A aseptic filling still needs to be stationed in a grade B background which requires a preceding grade B gowning room. The overall usage of space is not as economical as one might think and it would be hard to convince the auditors that cross contamination would be unlikely.

In summary, our one room, one product concept simplifies the work flow and allows two rooms in operation simultaneously. No different batches of PET drugs will be processed in the same hot cell space that greatly lowers the risk of cross contamination. Though now the synthesis module is set up in grade B environment, this only enhances the quality of production. In conclusion, our cleanroom design is effective and in compliance with the most current GMP.

Conflict of Interests

The authors declare that there is no conflict of interests regarding the publication of this paper.

Acknowledgment

The authors wish to thank Dr. Chih-Hao K. Kao, the Nuclear Medicine and Radiopharmaceutical Production, Hualien Tzu Chi Hospital, Hualien, Taiwan, for his valuable comments on design and validation of the CGMP facility.

References

- [1] D. Delbeke, R. E. Coleman, M. J. Guiberteau et al., "Procedure guideline for tumor imaging with ^{18}F -FDG PET/CT 1.0," *Journal of Nuclear Medicine*, vol. 47, no. 5, pp. 885–895, 2006.
- [2] *Fludeoxyglucose F 18 injection. Sample Formats: Application to Manufacture Ammonia N 13 Injection, Fluorodeoxyglucose F 18 Injection (FDG F 18) and Sodium Fluoride F 18 Injection Chemistry, Manufacturing, and Control Sections*, U.S. Food and Drug Administration, 2002.
- [3] J. C. Hung, "Comparison of various requirements of the quality assurance procedures for ^{18}F -FDG injection," *Journal of Nuclear Medicine*, vol. 43, no. 11, pp. 1495–1506, 2002.
- [4] G.-J. Meyer, H. Mäcke, J. Schuhmacher, W. H. Knapp, and M. Hofmann, " ^{68}Ga -labelled DOTA-derivatised peptide ligands," *European Journal of Nuclear Medicine and Molecular Imaging*, vol. 31, no. 8, pp. 1097–1104, 2004.
- [5] I. Velikyan, G. J. Beyer, and B. Långström, "Microwave-supported preparation of (^{68}Ga) bioconjugates with high specific radioactivity," *Bioconjugate Chemistry*, vol. 15, no. 3, pp. 554–560, 2004.
- [6] Y. Menda and M. M. Graham, "Update on ^{18}F -fluorodeoxyglucose/positron emission tomography and positron emission tomography/computed tomography imaging of squamous head and neck cancers," *Seminars in Nuclear Medicine*, vol. 35, no. 4, pp. 214–219, 2005.
- [7] W. Siggelkow, W. Rath, U. Buell, and M. Zimny, "FDG PET and tumour markers in the diagnosis of recurrent and metastatic breast cancer," *European Journal of Nuclear Medicine and Molecular Imaging*, vol. 31, no. 1, pp. S118–S124, 2004.
- [8] T.-C. Yen and C.-H. Lai, "Positron emission tomography in gynecologic cancer," *Seminars in Nuclear Medicine*, vol. 36, no. 1, pp. 93–104, 2006.
- [9] P. F. Rambaldi, V. Cuccurullo, V. Briganti, and L. Mansi, "The present and future role of ^{111}In Pentetreotide in the PET era," *Quarterly Journal of Nuclear Medicine and Molecular Imaging*, vol. 49, no. 3, pp. 225–235, 2005.
- [10] M. Henze, A. Dimitrakopoulou-Strauss, S. Milker-Zabel et al., "Characterization of ^{68}Ga -DOTA-D-Phe1-Tyr 3-octreotide kinetics in patients with meningiomas," *Journal of Nuclear Medicine*, vol. 46, no. 5, pp. 763–769, 2005.
- [11] S. Milker-Zabel, A. Zabel-du Bois, M. Henze et al., "Improved target volume definition for fractionated stereotactic radiotherapy in patients with intracranial meningiomas by correlation of CT, MRI, and [^{68}Ga]-DOTATOC-PET," *International Journal of Radiation Oncology Biology Physics*, vol. 65, no. 1, pp. 222–227, 2006.
- [12] T. D. Poeppel, I. Binse, S. Petersenn et al., " ^{68}Ga -DOTATOC versus ^{68}Ga -DOTATATE PET/CT in functional imaging of neuroendocrine tumors," *Journal of Nuclear Medicine*, vol. 52, no. 12, pp. 1864–1870, 2011.
- [13] A. R. Haug, R. Cindea-Drimus, C. J. Auernhammer et al., "The Role of ^{68}Ga -DOTATATE PET/CT in suspected neuroendocrine tumors," *Journal of Nuclear Medicine*, vol. 53, no. 11, pp. 1686–1692, 2012.

Research Article

Automated Synthesis of ^{18}F -Fluoropropoxytryptophan for Amino Acid Transporter System Imaging

I-Hong Shih, Xu-Dong Duan, Fan-Lin Kong, Michael D. Williams, Kevin Yang, Yin-Han Zhang, and David J. Yang

Department of Cancer Systems Imaging, The University of Texas M. D. Anderson Cancer Center, Houston, TX 77030, USA

Correspondence should be addressed to I-Hong Shih; ishih@mdanderson.org

Received 30 January 2014; Revised 2 April 2014; Accepted 7 May 2014; Published 20 July 2014

Academic Editor: Mei-Hsiu Liao

Copyright © 2014 I-Hong Shih et al. This is an open access article distributed under the Creative Commons Attribution License, which permits unrestricted use, distribution, and reproduction in any medium, provided the original work is properly cited.

Objective. This study was to develop a cGMP grade of [^{18}F]fluoropropoxytryptophan (^{18}F -FTP) to assess tryptophan transporters using an automated synthesizer. **Methods.** Tosylpropoxytryptophan (Ts-TP) was reacted with K^{18}F /kryptofix complex. After column purification, solvent evaporation, and hydrolysis, the identity and purity of the product were validated by radio-TLC (1M-ammonium acetate : methanol = 4 : 1) and HPLC (C-18 column, methanol : water = 7 : 3) analyses. *In vitro* cellular uptake of ^{18}F -FTP and ^{18}F -FDG was performed in human prostate cancer cells. PET imaging studies were performed with ^{18}F -FTP and ^{18}F -FDG in prostate and small cell lung tumor-bearing mice (3.7 MBq/mouse, iv). **Results.** Radio-TLC and HPLC analyses of ^{18}F -FTP showed that the R_f and R_t values were 0.9 and 9 min, respectively. Radiochemical purity was >99%. The radiochemical yield was 37.7% (EOS 90 min, decay corrected). Cellular uptake of ^{18}F -FTP and ^{18}F -FDG showed enhanced uptake as a function of incubation time. PET imaging studies showed that ^{18}F -FTP had less tumor uptake than ^{18}F -FDG in prostate cancer model. However, ^{18}F -FTP had more uptake than ^{18}F -FDG in small cell lung cancer model. **Conclusion.** ^{18}F -FTP could be synthesized with high radiochemical yield. Assessment of upregulated transporters activity by ^{18}F -FTP may provide potential applications in differential diagnosis and prediction of early treatment response.

1. Introduction

Molecular imaging agents play a major role in drug discovery and development because of their ability to quantify drug properties *in vivo*. For example, positron emission tomography (PET) agents show high specific activities since they are made through a nuclear transformation and use carrier free forms of isotopes. Thus, PET agents do not produce detectable pharmacologic effects but provide important information concerning the characterization of various diseases such as central nervous system diseases (epilepsy, psychosis, dementia, and Alzheimer's disease) [1–4], cardiovascular diseases (myocardial viability) [5], cancer staging, restaging, and treatment planning for the malignant diseases [6]. In addition, molecular imaging helps to control and monitor dosage for increased safety and effectiveness.

The trends for PET agent development in oncology are to assist in the determination of optimal therapeutic dosing, delineation of differential diagnosis between inflammation/infection and recurrence, determination of sensitive or resistant to treatment response, and prediction of treatment response by selecting patient who may respond to therapy. ^{18}F -Fluorodeoxyglucose (^{18}F -FDG), a gold standard for PET, has been successfully used to image tumors with high glycolytic activity [7]. However, ^{18}F -FDG has several limitations that give rise to false positive/negative diagnosis and poor predictive value of chemoradiation therapy to tumor response [8]. For instance, ^{18}F -FDG has poor contrast in brain tumor due to the high uptake of glucose in normal brain tissue [9], and it has poor differentiation of tumor from inflammatory tissue because of high uptake of ^{18}F -FDG in granulocytes and macrophages [10]. Radiolabeled amino

acid is an alternative in characterizing tumors because of low accumulation in normal tissue, rather high accumulation in tumor tissue, and rapid blood clearance. Large neutral amino acids are uptaken by system L amino acid transporters (LAT), whose subtype LAT1 is reported to be upregulated in most cancerous tissues at both primary and metastatic sites [11–13]. For instance, 5-hydroxy-L-tryptophan (5-HTP) is taken up by the tumor cells via their LAT1 [14]. Upregulated LAT1 indirectly measures cell proliferation activity [15], and elevated expression of LAT1 in cancers correlates with poor prognosis [16].

Tryptophan is essential for normal growth and development in children as well as for keeping the nitrogen balance in adults. In addition, T-cells also depend on tryptophan for their immune response after invading cells have been recognized. Tryptophan is oxidized by indoleamine 2,3-dioxygenase (IDO) via the kynurenine pathway, and low uptake of tryptophan by LAT1 transporter may cause the T-cells death and subsequently result in cancers and autoimmune diseases. A high level of IDO expression reduces the concentration of tryptophan in the local tissues and starves T-cells for tryptophan. This results in an excess of kynurenine in the body fluids, which is toxic to T-cells and causes tumor immune resistance [17]. Tryptophan-kynurenine pathway plays a major role in neurological diseases and cancers [17, 18]. In addition, serotonin is also derived from tryptophan via tryptophan hydroxylase (TPH). Increased expression of TPH is associated with malignant phenotype in tumors. It has been suggested that IDO, LAT1, and serotonergic markers could serve as potential molecular targets to inhibit tumor cell growth [19]. Thus, it is amenable to develop a radiolabeled tryptophan to monitor *in vivo* expression and activity of IDO, LAT1, and TPH1 as well as to assess therapeutic response after selective inhibitors of IDO, LAT1, and TPH1 in cancer treatments.

Previously, α -[^{11}C]methyl-L-tryptophan (AMT), a substrate for TPH and IDO, was developed to study tryptophan transporter system. In PET studies of brain tumors, elevated tumor AMT metabolic rates were associated with increased expression of IDO [19]. However, the short half-life of ^{11}C ($t_{1/2} = 20$ min) makes it difficult in repeated imaging and multiple clinical studies. The half-life of ^{18}F is 110 min which allows repeated imaging and is suitable for multiple clinic studies. Krämer et al. evaluated the *in vitro* and *in vivo* characteristics of 5-(2- ^{18}F -fluoroethoxy)-L-tryptophan (^{18}F -FEHTP) as a PET probe for tumor imaging [20]. He et al. developed a similar analog 5-(3- ^{18}F -fluoropropoxy)-L-tryptophan (^{18}F -FPTP) and performed its biologic evaluation [21]. ^{18}F -FPTP was synthesized manually with a two-step reaction. The overall uncorrected radiochemical yield of ^{18}F -FPTP was $21.1 \pm 4.4\%$ with a synthesis time of 60 min. Both ^{18}F -FEHTP and ^{18}F -FPTP were accumulated in cancer cells. ^{18}F -FEHTP has been studied in endocrine (small cell lung cancer cells) and nonendocrine (PC-3, MDA 231) tumor models via LAT1 transporter system. ^{18}F -FPTP was accumulated in hepatocellular carcinoma cell (Hepa 1-6) via the amino acid transport system B0+, LAT2, and ASC. ^{18}F -FEHTP and ^{18}F -FPTP were not decarboxylated by aromatic

L-amino acid decarboxylase (AADC) and did not incorporate into protein synthesis [20, 21]. PET imaging revealed good uptake of ^{18}F -FEHTP and ^{18}F -FPTP in endocrine and nonendocrine tumors in rodents with low background. Though both ^{18}F -FEHTP and ^{18}F -FPTP could serve as PET probes for assessing tumor LAT1 activity, ^{18}F -FPTP was superior to ^{18}F -FEHTP and ^{18}F -FDG due to its better differentiation between tumors and inflammation in animal models. ^{18}F -FPTP had high tumor to inflammation count density ratio (2.53) at 60 min after administration [21].

Radiosynthesis of ^{18}F -compounds must be rapid because of higher risk of radiation exposure and short half-life of ^{18}F used during radiosynthesis. An automated apparatus is needed to assure production efficiency and minimize the radiation exposure by PET isotopes. ^{18}F -FPTP was selected as a candidate for automation due to its superior quality of images compared to ^{18}F -FEHTP. At present, commercially available black boxes are only suitable for production of ^{18}F -FDG but not for the preparation of ^{18}F -labeled tryptophan. To avoid mixing up or contamination, we developed a dedicated module for production of ^{18}F -FPTP for clinical application. Here, we report the efficient automated synthesis of ^{18}F -FTP (known as manually developed ^{18}F -FPTP) for cGMP (current Good Manufacturing Practice) compliance and its biologic validation. The automated module provides consistence, reproducible, and acceptable ^{18}F -FTP product.

2. Materials and Methods

2.1. Synthesis of Cold Fluoropropoxytryptophan (FTP; Reference Standard). The synthetic scheme of FTP is shown in Figure 1. Three steps were involved in the synthesis. In step 1, thionyl chloride (2.4 mL, 34 mmol) was dissolved in anhydrous methanol (100 mL) and cooled to 0°C . 5-Hydroxytryptophan (5.00 g, 22.7 mmol) was added in portions. After temperature returned to room temperature, the mixture was refluxed overnight. The solvent was evaporated, followed by silica-gel packed column chromatographic purification using ethyl acetate : hexane (4 : 1, v/v) as an eluent to yield 5-hydroxytryptophan methyl ester hydrochloride 5.18 g (84% yield). $^1\text{H-NMR}$ (300 MHz, CDCl_3): 7.23 (*d*, $J = 8.7$ Hz, 1H), 7.15 (*s*, 1H), 6.91 (*d*, $J = 2.1$ Hz, 1H), 6.73 (*dxd*, $J = 8.7$, $J' = 2.3$ Hz, 1H), 4.29 (*t*, $J = 6.3$, 1H), 3.83 (*s*, 3H), and 3.26–3.42 (*m*, 2H). $^{13}\text{C-NMR}$ (300 MHz, CDCl_3): 169.8, 150.8, 132.2, 127.9, 125.4, 112.2, 112.1, 105.6, 102.1, 53.5, 52.7, and 26.7.

Subsequently, 5-hydroxytryptophan methyl ester (2.4 g, 10 mmol) was dissolved in 100 mL of anhydrous DMF. Anhydrous triethyl amine (4 mL, 30 mmol) was added while stirring. Diterbutyldicarbonate (2.6 g, 12 mmol) was then added to the solution. The mixture was stirred and heated at 60°C overnight. The reaction mixture was evaporated under reduced pressure and was reconstituted in ethyl acetate. The crude product solution was loaded on a silica gel column and eluted with ethyl acetate : hexane (from 1 : 3 to 2 : 3, v/v). N-Boc-5-Hydroxytryptophan methyl ester was collected after solvent evaporation to yield 3.08 g (92% yield). $^1\text{H-NMR}$

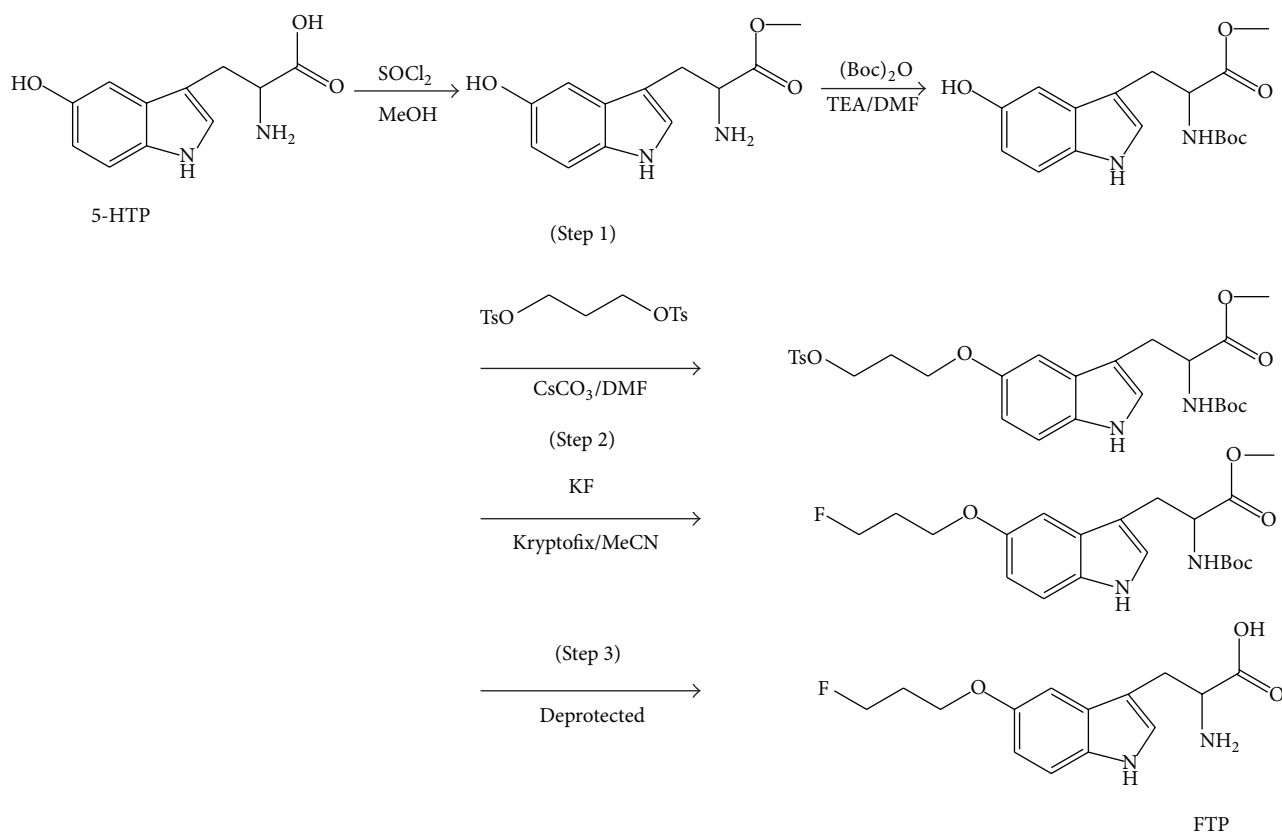


FIGURE 1: Synthetic scheme of $^{18/19}\text{F}$ fluoropropoxytryptophan ($^{18/19}\text{F}$ -FTP).

(300 MHz, CDCl_3): 7.05 (*d*, $J = 8.7$ Hz, 1 H), 6.90 (*s*, 1 H), 6.84 (*d*, $J = 2.1$ Hz, 1 H), 6.56 (*dx**d*, $J = 8.7$, $J' = 2.3$ Hz, 1 H), 4.30 (*t*, $J = 6.3$, 1 H), 3.56 (*s*, 3 H), 2.90–3.10 (*m*, 2 H), and 1.29 (*s*, 9 H). ^{13}C -NMR (300 MHz, CDCl_3): 173.8, 156.8, 150.4, 132.0, 128.4, 124.2, 111.8, 111.6, 109.0, 102.5, 79.7, 55.0, 51.6, 27.9, and 27.7.

In step 2, an aliphatic tosyl chain was to be added at phenolic hydroxyl group of N-Boc-5-hydroxytryptophan methyl ester. Cesium carbonate (3.9 g, 12 mmol) was added to N-Boc-5-hydroxytryptophan methyl ester (3.4 g, 10 mmol) in 60 mL of anhydrous DMF while stirring under nitrogen atmosphere. 1,3-Ditosyl-propanol (6.2 g, 16 mmol) was added to the solution. The mixture was stirred for overnight at 60°C . The reaction mixture was evaporated under reduced pressure and was reconstituted in ethyl acetate. The crude product solution was loaded on a silica gel column and eluted with ethyl acetate : hexane (from 1 : 3 to 2 : 3, v/v) to yield 4.6 g (84% yield) of N-Boc-tosylpropoxytryptophan methyl ester. ^1H -NMR (300 MHz, CDCl_3): 7.77 (*d*, $J = 8.3$ Hz, 2 H), 7.24 (*d*, $J = 8.8$ Hz, 1 H), 7.19 (*d*, $J = 8.3$ Hz, 2 H), 6.97 (*s*, 1 H), 6.91 (*d*, $J = 2.4$ Hz, 1 H), 6.70 (*dx**d*, $J = 8.8$, $J' = 2.4$ Hz, 1 H), 4.53 (*m*, 1 H), 4.28 (*t*, $J = 6.3$ Hz, 2 H), 4.00 (*t*, $J = 5.8$ Hz, 2 H), 3.67 (*s*, 3 H), 3.21 (*d*, $J = 5.2$, 2 H), 2.34 (*s*, 3 H), 2.13 (quintet, $H = 6.0$ Hz, 2 H), and 1.41 (*s*, 9 H). ^{13}C -NMR (300 MHz, CDCl_3): 173.2, 155.7, 153.4, 145.1, 133.3, 131.9, 130.2, 128.4, 128.2, 124.1, 113.1, 112.2, 110.3, 102.2, 77.6, 67.8, 64.4, 54.5, 52.7, 29.5, 28.7,

28.5, and 21.9. Mass spectrometry (M^+): 545.5 (100%), 445.4 (5%), 171.2 (10%), and 105.2 (10%).

In step 3, N-Boc-tosylpropoxytryptophan methyl ester was reacted with potassium fluoride (KF) in 2,2,2-kryptofix, followed by deprotection. N-Boc-Tosylpropoxytryptophan methyl ester (50 mg, 0.09 mmol), potassium fluoride (KF, 10.5 mg, 0.18 mmol), and 2,2,2-kryptofix (34 mg, 0.09 mmol) were dissolved in 5 mL of anhydrous acetonitrile while stirring under nitrogen atmosphere and was refluxed for 4 hrs. The reaction mixture was evaporated under reduced pressure, reconstituted in ethyl acetate (EtOAc, 0.5 mL), and purified with column chromatography using hexane : EtOAc = 1 : 1(v/v) to obtain 15 mg (43% yield) of N-Boc-fluoropropoxytryptophan methyl ester. ^1H -NMR (300 MHz, CDCl_3): 7.16 (*d*, $J = 8.8$ Hz, 1 H), 6.95 (*s*, 1 H), 6.91 (*d*, $J = 2.3$ Hz, 1 H), 6.78 (*dx**d*, $J = 8.8$, $J' = 2.3$ Hz, 1 H), 5.02 (*d*, 2 H), 4.69 (*t*, $J = 5.9$ Hz, 1 H), 4.53 (*t*, $J = 5.9$ Hz, 1 H), 4.07 (*d*, $J = 5.1$ Hz, 2 H), 3.61 (*s*, 3 H), 3.21 (*d*, $J = 5.1$, 2 H), 2.17 (quintet, $H = 6.0$ Hz, 1 H), 2.08 (quintet, $H = 6.0$ Hz, 1 H), and 1.35 (*s*, 9 H). ^{13}C -NMR (300 MHz, CDCl_3): 173.2, 155.7, 153.4, 131.9, 128.5, 124.0, 113.3, 112.3, 110.4, 102.4, 82.5, 80.3, 64.9, 54.7, 52.6, 32.9, 31.2, and 28.7. Mass spectrometry (M^+): 393.3 (50%), 248.8 (10%), 172.8 (20%), 140.8 (30%), and 112.6 (100%).

To deprotect amino and ester groups, N-Boc-fluoropropoxytryptophan methyl ester (15 mg, 0.038 mmol) was dissolved in dichloromethane : anhydrous trifluoroacetic acid

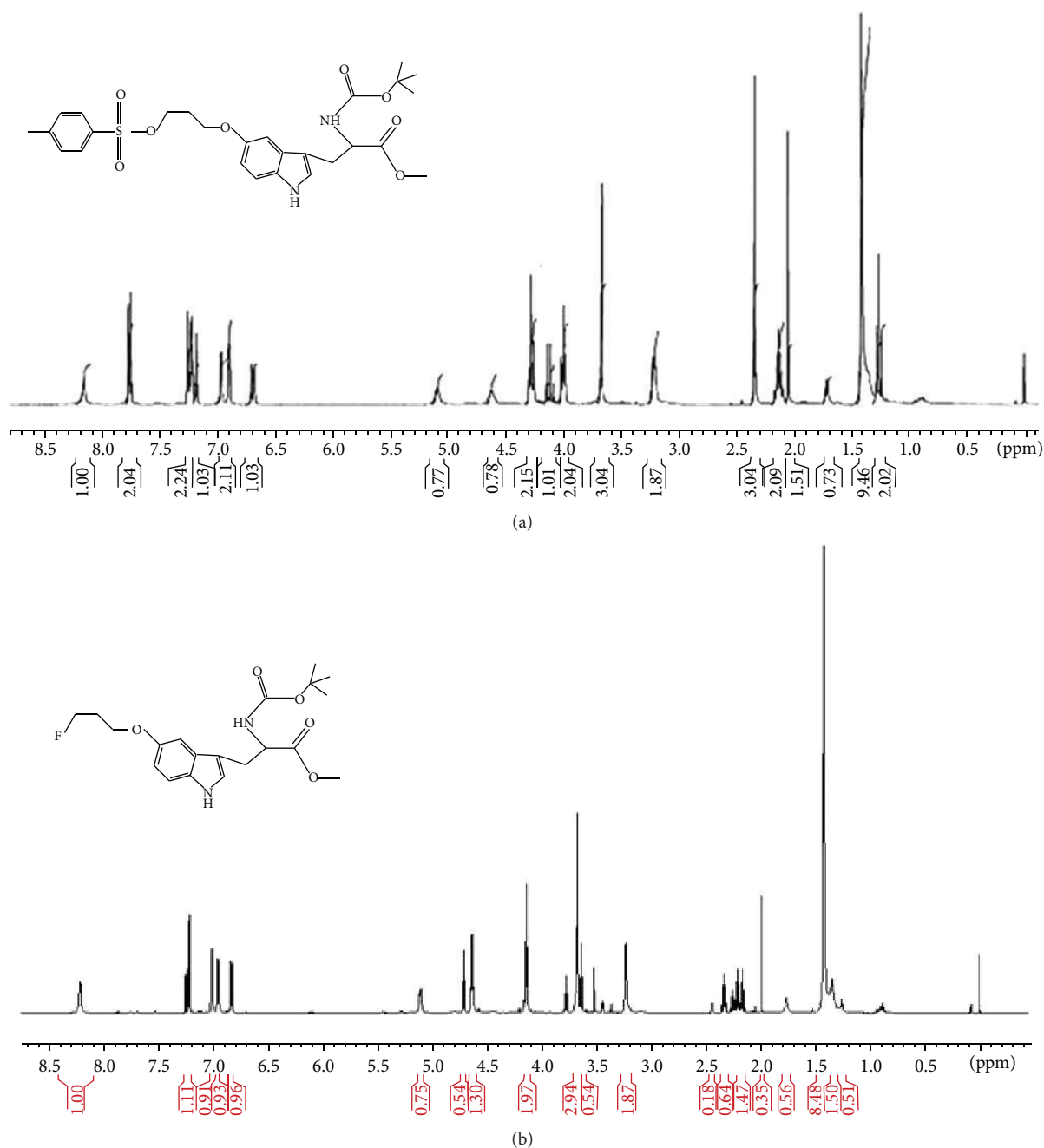


FIGURE 2: ¹H-NMR of N-Boc-tosylpropoxytryptophan methyl ester (a) and N-Boc-fluoropropoxytryptophan methyl ester (b).

(0.25 mL/0.25 mL). The mixture was stirred for 60 min. After solvent evaporation, 0.5 mL of 1 N NaOH was added to the residue. The reaction mixture was heated at 85°C for 60 min or till full dissolving of the mixture. The product was purified by prep-TLC (1 mm) using MeOH : EtOAc (1 : 3, v : v) to yield FTP (5.5 mg, 44%). ¹H-NMR (300 MHz, CDCl₃): 6.97 (s, 1 H), 6.91 (d, *J* = 2.4 Hz, 1 H), 6.70 (*dx*d, *J* = 8.8, *J'* = 2.4 Hz, 1 H), 4.53 (*m*, 1 H), 4.28 (*t*, *J* = 6.3 Hz, 2 H), 4.00 (*t*, *J* = 5.8 Hz, 2 H), 3.67 (*s*, 3 H), 3.21 (*d*, *J* = 5.2, 2 H), and 2.13 (quintet, *H* = 6.0 Hz, 2 H). ¹³C-NMR (300 MHz, CDCl₃): 173.2, 153.4, 131.9,

128.5, 124.0, 113.3, 112.3, 110.4, 102.4, 82.5, 64.9, 54.7, 32.9, and 31.2.

2.2. Development of the Automated Module. We have designed and built an automated module which is compact and easy to use and be maintained. This module consists of an apparatus and a control box. This system uses valves as well as other fittings and will be housed in the lead-shielded hot cell. In addition to the main unit, a built-in vacuum pump is used to generate sufficient vacuum for waste collection

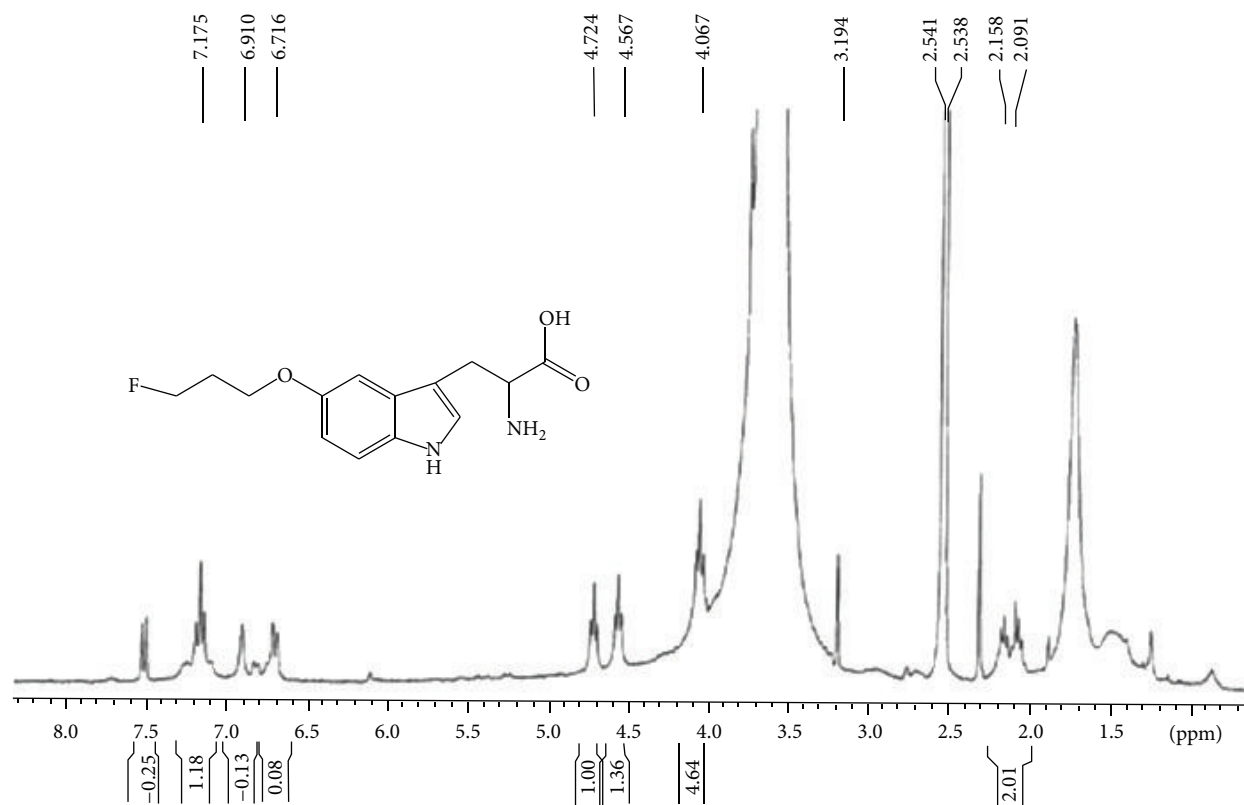


FIGURE 3: ¹H-NMR of cold fluoropropoxytryptophan (FTP).

and venting, and the infrared heater is installed for rapid heating. The control box hosting digital/analog input/output (I/O) modules is operated by LabView software (National Instruments, Austin, TX). We used this software to write the customized user interface for controlling and monitoring the synthesis of ¹⁸F-FTP. The module provides a rapid synthesis of ¹⁸F-FTP and can recover ¹⁸O-enriched water using an anionic resin which is cost-effective.

2.3. Radiosynthesis of [¹⁸F]Fluoropropoxytryptophan (¹⁸F-FTP). The synthetic scheme is the same as that of cold FTP (shown in Figure 1). [¹⁸F]Fluoride was produced by proton irradiation of enriched [¹⁸O]-water (Sigma Chemical Company, St. Louis, MO) in a small-volume silver target. Aliquots containing 4.44 GBq of ¹⁸F activity were combined with 26 mg kryptofix-2,2,2 and 4.6 mg anhydrous potassium carbonate, heated under reduced pressure to remove the excess [¹⁸O]-water, and dried by azeotropic distillation with acetonitrile (3 × 1.5 mL). K¹⁸F/kryptofix complex was reconstituted in 0.3 mL acetonitrile. An aliquot of K¹⁸F/kryptofix (0.62 GBq in 0.1 mL acetonitrile) was then administered to the module via an external port. N-Boc-Tosylpropoxytryptophan methyl ester (5 mg) was dissolved in acetonitrile (0.2 mL) and injected through a 1 mL syringe to a reaction vial (RV1). The IR heater automatically warmed the RV1 at 90°C for 15 min. The mixture in the RV1 was passed through a silica gel packed column (SPE-500 mg, Whatman

Lab, Clifton, NJ) and eluted with 1 mL ethyl acetate to the reaction vessel 2 (RV2) under nitrogen flow to remove free fluoride. Before de-BOC, the solution inside the RV2 was evaporated under vacuum at 90°C for 15 min. After that, trifluoroacetate (0.2 mL) in dichloromethane (0.4 mL) was loaded into the RV2 to deprotect amino group. The solution was set under room temperature for 10 minutes to allow the reaction to complete and then the solvent was evaporated to dryness under vacuum for 15 minutes. For deesterification, ethyl alcohol (0.4 mL) and 1 N NaOH (0.2 mL) were added into RV2. The hydrolysis of the ester group was performed at 90°C for 15 min. The solution in RV2 was evaporated under reduced pressure. ¹⁸F-FTP was reconstituted in water (1.2 mL) and filtered through a 0.22 μm filter. The activities of column, RV1 and RV2, were counted upon completion of the synthesis. A NIST-traceable dose calibrator was used to determine total activity (GBq or mCi) and the radioactivity concentration (GBq/mL or mCi/mL). A radio thin-layer chromatographic (radio-TLC) scanner (Bioscan System 200, Washington, DC) and high performance liquid chromatography (HPLC) using a 20 μL loop and Bondapak CN-RP column eluted with methanol:water = 7:3, v/v and flow rate 0.5 mL/min at 210 nm were performed to assure the purity and identity of ¹⁸F-FTP. To assure the quality of the product, the pyrogenicity test using Bacterial Endotoxins kit (Sigma, St. Louis, MO), the pH (by pH paper), and residual solvents (by LC-MS) were measured. The sterility test

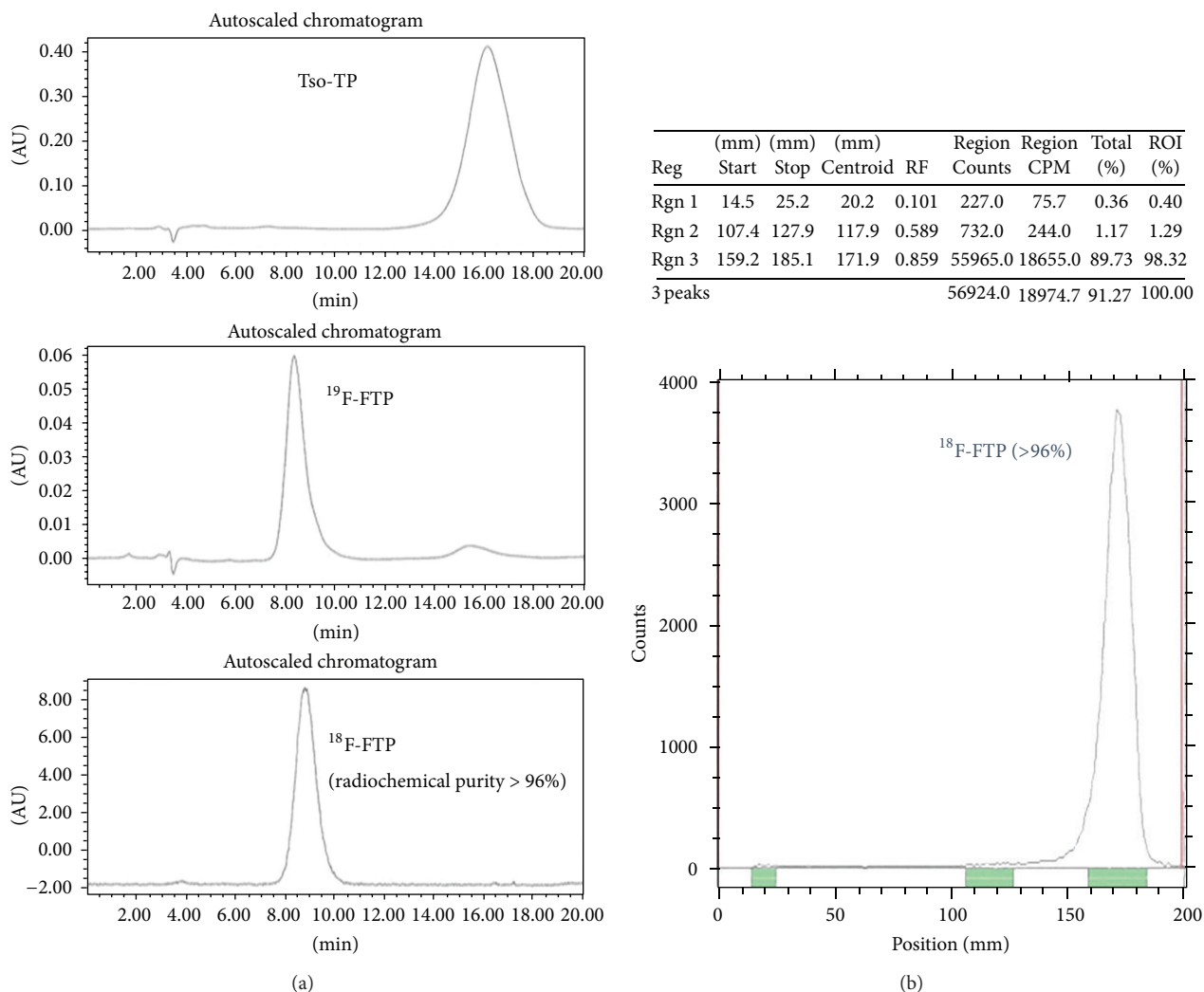


FIGURE 4: (a) HPLC of ^{18}F -FTP showed radiochemical purity >96% using C-18 RP (MeOH : water = 7 : 3) at flow rate 0.5 mL/min; (b) radio-TLC of ^{18}F -FTP showed greater than 96% purity using mobile phase ammonium acetate (1 M) : methanol (4 : 1, v : v).

using aerobic (NR6) and anaerobic (NR7) fermentation broth (Becton Dickinson Diagnostic Instrument Systems, Towson, MD) were conducted at 37°C for 7 days. The cloudiness of the broth was examined. The membrane filter integrity was also examined.

2.4. In Vitro Cellular Kinetic Assay. To assure quality of ^{18}F -FTP, cell uptake assays were performed for biologic validation. Cell uptake assay of ^{18}F -FTP and ^{18}F -FDG was performed using human prostate cancer cells (PC-3) as described in known literature. The cell line was selected because it is known as an excellent *in vitro* model for studying the interaction of large neutral amino acid conjugated drugs with LAT1 transporter [22]. ^3H -Tyrosine kinetic assays showed the saturable kinetics with $K(m)$ and $V(max)$ values of $34 \pm 3 \mu\text{M}$ and 0.70 ± 0.02 nanomoles/min/mg protein, respectively. The cell line was purchased from American Type Tissue Culture (Bethesda, MD). Cells were maintained in the mixtures of

Dulbecco's modification of Eagle's medium (DMEM), F-12 (GIBCO, Grand Island, NY), and 10% phosphate buffered saline (PBS) at 37°C in a humidified atmosphere containing 5% CO_2 . The cells were plated to 12-well tissue culture plates that contained 50,000 cells per well. The cells in each well were incubated with 0.74 MBq of ^{18}F -FTP or ^{18}F -FDG at 37°C for 30–120 min, respectively. After incubation, cells were washed with ice-cold phosphate-buffered saline (PBS) twice and trypsinized with 0.5 mL of trypsin solution. Then, cells were collected and the radioactivity was measured by gamma counter (PerkinElmer, Waltham, MA). Data are expressed in mean \pm S.D. percent uptake of three measurements.

2.5. PET Imaging Studies. The animals were housed in the University of Texas M. D. Anderson Cancer Center facility. All protocols involving animals were approved by the M. D. Anderson Animal Use and Care Committee. Expression of LAT1 in neuroendocrine tumors of the lung has been

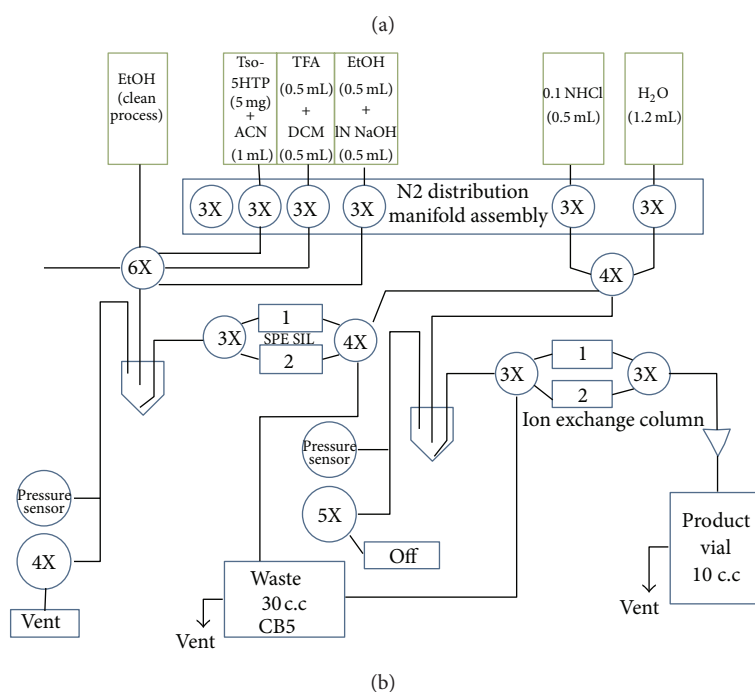
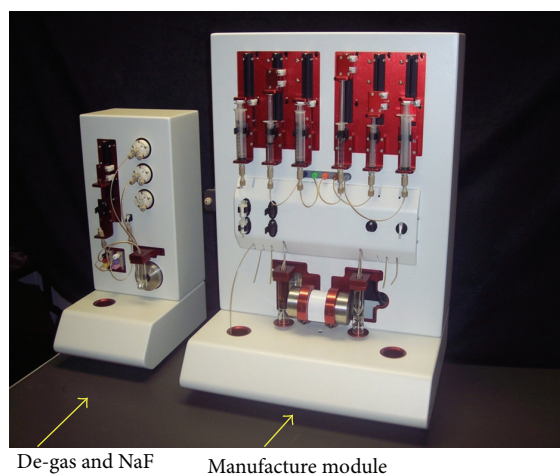


FIGURE 5: (a) Automated module for production of ^{18}F -FTP. (b) Functional component illustration in this module.

reported [23]. NCI H187Lu is an endocrine (small cell lung cancer) cancer cells and orthotopic nude mouse model is well established [24]. Thus, it was selected for comparison with nonendocrine (PC-3) mouse model. Athymic nude mice (15–20 g; NCI–NIH, Bethesda, MD) were inoculated with PC-3 or human small cell lung cancer NCI-H187Lu cells (s.c. 10^6 cells/mouse) at the left legs. After 16 days, a tumor size of 1 cm was observed. Mice were anesthetized with 2% isoflurane and injected intravenously with 7.4 MBq of ^{18}F -FDG and ^{18}F -FTP, respectively. Four serial 15-minute transaxial PET images were obtained through microPET/CT (Inveon, Siemens Medical System, Malvern, PA) or Concorde R4 microPET scanner (Knoxville, TN). All corrections for attenuation, scatter, dead time, and randoms were applied to generate quantifiable images.

3. Results

3.1. Chemistry. Using N-Boc-tosylpropoxytryptophan methyl ester as a precursor, we are able to shorten the synthetic step to one-step synthesis. ^1H -NMR of N-Boc-tosylpropoxytryptophan methyl ester and N-Boc-fluoropropoxytryptophan methyl ester are shown in Figure 2.

After hydrolysis, ^1H NMR of fluoropropoxytryptophan (FTP) is shown in Figure 3. During radiosynthesis, the activity of N-Boc- ^{18}F -fluoropropoxytryptophan methyl ester was 0.30 GBq (55.63%, decay-corrected). The radioactivity, radiochemical yield, and end-of-synthesis (EOS) time for ^{18}F -FTP were 0.13 GBq, 37.73% (decay-corrected), and 90 min, respectively. Radio-TLC (1 M ammonium acetate : methanol = 4 : 1, v/v) showed that the retarded factor (R_f) value was 0.9.

HPLC of tosyl precursor and ^{18}F -FTP showed that the retention time (R_t) was 16 min and 9 min, respectively (Figure 4(a)). The no-carrier-added displacement product corresponded to the unlabeled FTP under the same TLC and HPLC system. Radiochemical purity determined by HPLC and radio-TLC of the title compound was >96% (Figure 4). The specific activity of ^{18}F -FTP determined by HPLC was 74 GBq/ μmol . The pyrogenicity test (Bacterial Endotoxins) was <175 EU/4 mL and the pH was about 6.5. The product was sterile. There was no corruption for membrane filter integrity. LC-MS showed no more than 0.04% acetonitrile or methylene chloride of residual solvents in ^{18}F -FTP product. Automated module for production of FTP and the flow chart of the module are shown in Figure 5.

3.2. In Vitro Cellular Kinetic Assay. *In vitro* cell culture assays of ^{18}F -FTP and ^{18}F -FDG showed similar enhanced uptake patterns as a function of incubation time in PC-3 prostate cancer cells, and the uptake reached about 1.4% uptake for both radiotracers (Figure 6).

3.3. PET Imaging Studies. MicroPET/CT imaging studies showed that ^{18}F -FTP had less tumor uptake than ^{18}F -FDG at 22 min after administration of the tracer in prostate cancer model (Figure 7). However, ^{18}F -FTP had more uptake than ^{18}F -FDG at 45 min after administration of the tracer in small cell lung cancer model NCI-H187Lu by visualization (Figure 8). The uptake difference could be due to the nature of LAT1 activity in animal models.

4. Discussion

Assessment of the effectiveness of cancer therapy (e.g., volumetric and morphological changes) is generally measured by CT and MRI. In addition to these imaging modalities, the treatment endpoints rely almost exclusively on the analysis of biopsies by molecular and histopathological methods. These methods provide a microscopic picture of the general heterogeneous process. On the other hand, nuclear imaging measures blood flow and activity patterns. Therefore, to assess clinical endpoints adequately, a predictive nuclear biomarker is needed that would allow precise measurement of tumor targets on a whole-body image upon administration of a functional radiolabeled agent. These mechanism-based agents provide image-guided therapy which may discontinue ineffective treatment in the earlier phase and may be beneficial to patients.

Transporters for essential amino acids are particularly important because they are involved in protein synthesis to maintain cell integrity and cell cycle progression. Among several amino acid transporters, system L, a Na^+ -independent amino acid transport system, is a major route for providing cells with large neutral amino acids, including branched or aromatic amino acids. Large L-type amino acid transporter 1 (LAT1), a system L subtype, is suggested to be a target for therapy with antiproliferative inhibitors in cancer [25]. LAT family is known to form heterodimers, which

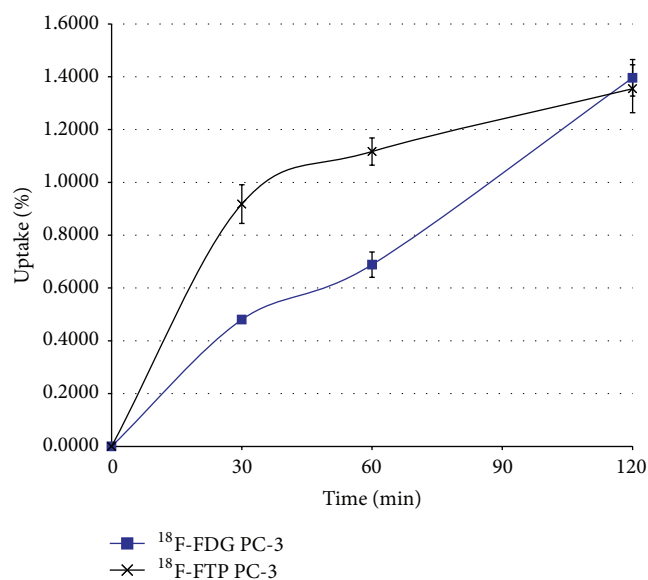


FIGURE 6: *In vitro* cellular kinetic assays of ^{18}F -FTP and ^{18}F -FDG showed similar enhanced uptake patterns as a function of incubation time in human prostate cancer cell line PC-3.

contain a chaperone-like heavy chain 4F2hc, and a 12-time transmembrane light chain that is unique to each subtype [26]. LAT1/4F2hc complex, one form of 4F2 antigen or CD98 antigen, preferentially transports large neutral amino acids, such as leucine, isoleucine, valine, phenylalanine, tyrosine, tryptophan, methionine, and histidine, which are essential for cell survival and proliferation [27]. An increasing amount of research shows that LAT1/4F2hc is overexpressed in a variety of human tumor cell lines and tumor tissues, suggesting that LAT1/4F2hc is implicated in the growth and proliferation of multiple types of human cancers [26]. Assessment of LAT1 activity provides potential applications in differential diagnosis and prediction of early treatment response in oncology and autoimmune diseases. Though ^{18}F -FDG-PET imaging demonstrates the increased glucose consumption of malignant cells, problems with specificity for cell proliferation have led to the development of new PET tracers. ^{18}F -FDG could assess metabolic activity, but it could not adequately assess neuroendocrine activity. ^{18}F -Fluorodopa has been used in clinic to assess dopamine transformation in both oncology and neurologic diseases. Due to the nature of LAT1 and neuroendocrine involvement in cancers and neurologic diseases, it would be important to develop a biomarker to probe LAT1 because LAT1 is the rate limiting step for the tumor and neuron uptake. The structure of ^{18}F -FTP is the same as ^{18}F -FPTP and ^{18}F -FPTP uptake is inhibited by LAT1 inhibitor, such as BCH (2-aminobicyclo-(2,2,1)-heptane-2-carboxylic acid)²¹. Thus, cell uptake of ^{18}F -FTP is recognized by LAT1.

The key difference in the synthesis of ^{18}F -FTP between our work and He et al. was the precursor [21]. The reported manual synthesis by He et al. used a 2-pot synthetic method

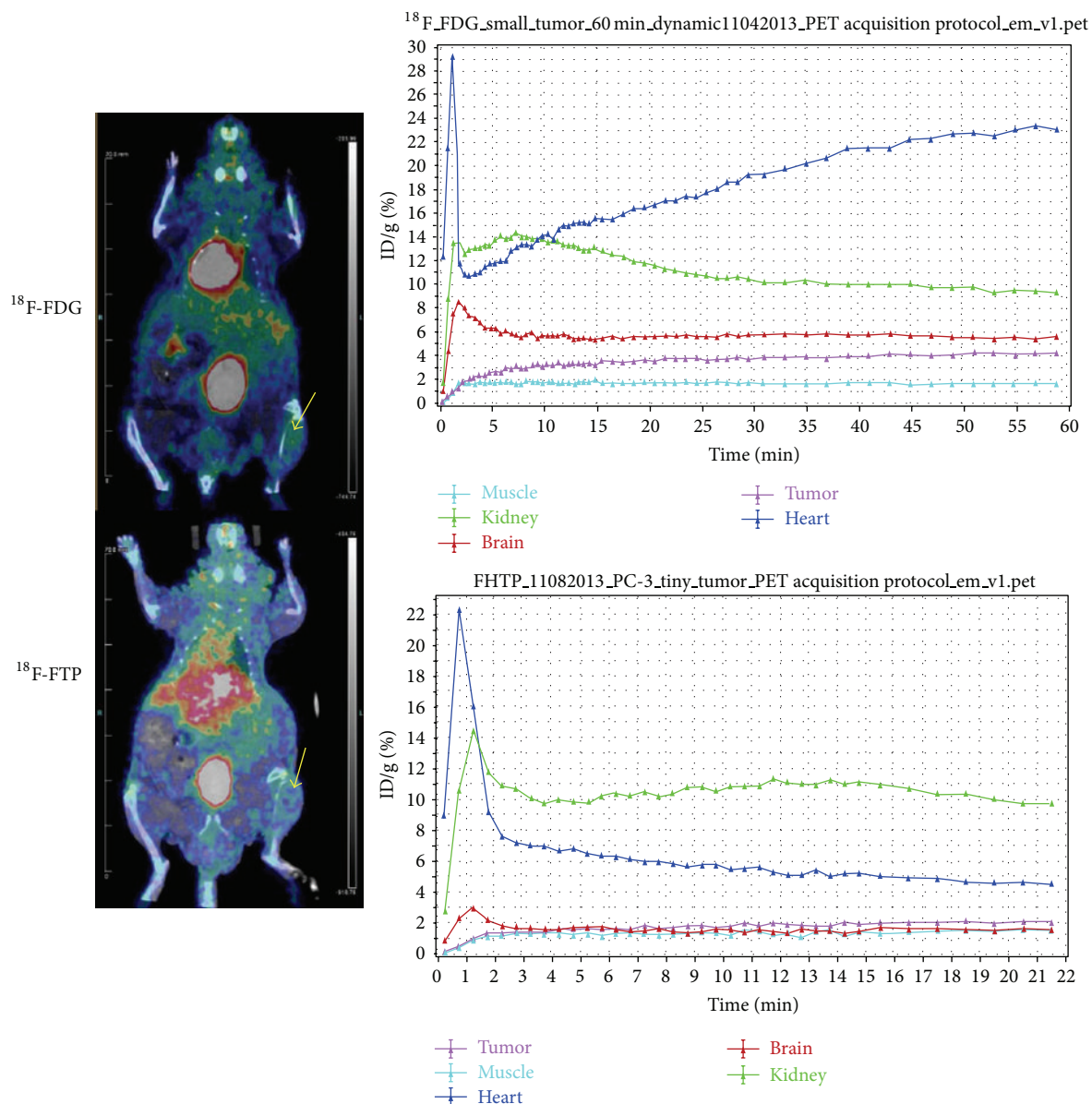


FIGURE 7: MicroPET/CT showed that $^{18}\text{F-FTP}$ had less tumor uptake than $^{18}\text{F-FDG}$ in prostate cancer model (PC-3, at 22 min). Arrow: tumor.

which caused lower yield [21]. The purity of our precursor (tosylpropoxytryptophan) and reference standard (FTP) were greater than 95%. Using our automated module, the radiochemical purity of $^{18}\text{F-FTP}$ was greater than 95%; 99.5% of the observed $^{18}\text{F-FTP}$ γ -emissions measured by a multichannel analyzer (MCA) corresponded to the 0.511 MeV. The $^{18}\text{F-FTP}$ product meets general acceptance criteria such as purity, identity, pH, pyrogenicity, and sterility. The overexpression of amino acid transporter system, such as LAT1, is an important marker for disease prognosis [22, 28]. In microPET imaging study, $^{18}\text{F-FTP}$ showed different biodistribution in two different tumor models. $^{18}\text{F-FTP}$ had less tumor uptake than $^{18}\text{F-FDG}$ at 22 min after administration in a PC-3

prostate cancer mouse model, while exhibiting higher tumor uptake in mice bearing NCI-H187Lu small cell lung cancer at 45 min after injection. The amount of tumor uptake may depend on the status of LAT1 transporter density in the two cancer cell lines. Though the study is focused on the development of an automated synthesis method of $^{18}\text{F-FTP}$ which fulfills the cGMP grade, further studies warrant determining the information of the LAT1 transporter density of NCI-H187Lu cancer cells and PC-3 prostate cancer cells.

In summary, $^{18}\text{F-FTP}$ was synthesized efficiently by one-pot method with high radiochemical yield and purity using an automated module. *In vitro* cellular uptake and PET imaging studies confirm biologic validation. Thus, $^{18}\text{F-FTP}$

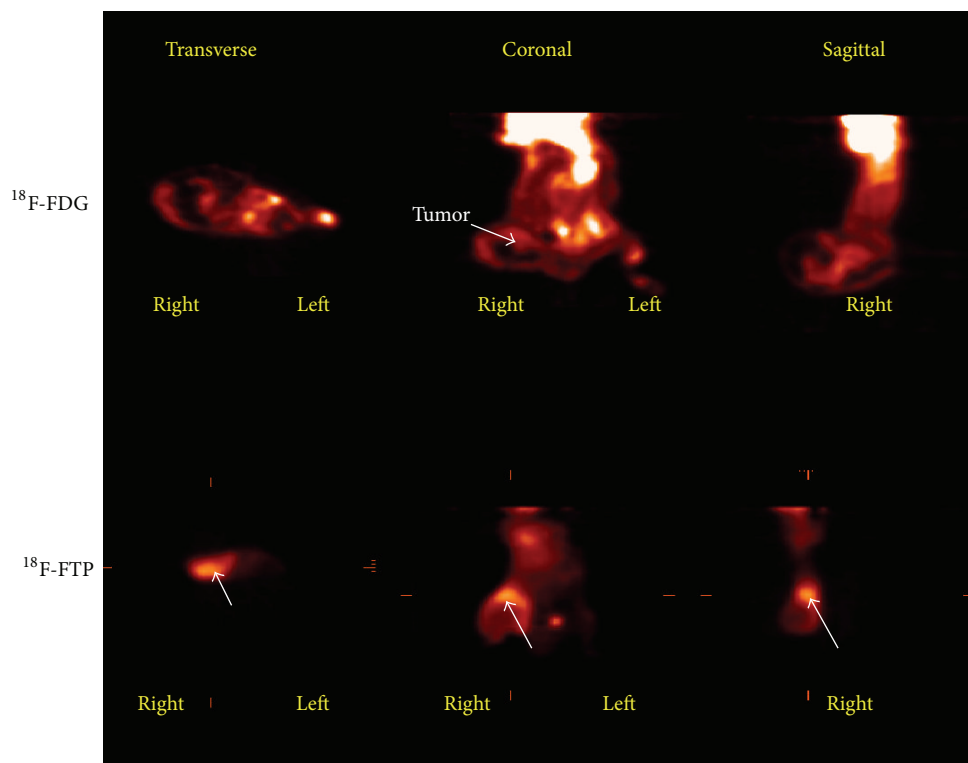


FIGURE 8: MicroPET imaging in human small cell lung tumor-bearing mice (NCI-H187Lu) at 45 min showed that ^{18}F -FTP had more tumor uptake than ^{18}F -FDG. Arrow: tumor.

may improve the diagnosis, planning, and monitoring of tryptophan transporter pathway-directed therapies.

Conflict of Interests

The authors declare that there is no conflict of interests regarding the publication of this paper.

Acknowledgments

This work was supported in part by MDACC sponsored Research Grant LS2007-00020647JW (Miyagi Clinic Sendai Medical Imaging Inc., Sendai, Japan), LS01-212 (Cell > Point, CO), and John S. Dunn Foundation. The animal research is supported by UT MD Anderson Cancer Center CORE Grant NIH/NCI P30CA016672.

References

- [1] S. Rubi, N. Costes, R. A. Heckemann et al., "Positron emission tomography with α -[^{11}C]methyl-L-tryptophan in tuberous sclerosis complex-related epilepsy," *Epilepsia*, vol. 54, no. 12, pp. 2143–2150, 2013.
- [2] H. K. Park, J. S. Kim, K. C. Im et al., "Visual hallucinations and cognitive impairment in parkinson's disease," *Canadian Journal of Neurological Sciences*, vol. 40, no. 5, pp. 657–662, 2013.
- [3] J. A. Bertelson and B. Ajtai, "Neuroimaging of dementia," *Neurologic Clinics*, vol. 32, pp. 59–93, 2014.
- [4] G. Chételat, R. La Joie, N. Villain et al., "Amyloid imaging in cognitively normal individuals, at-risk populations and preclinical Alzheimer's disease," *NeuroImage: Clinical*, vol. 2, no. 1, pp. 356–365, 2013.
- [5] S. Lehner, C. Uebles, F. Schüßler et al., "The amount of viable and dyssynchronous myocardium is associated with response to cardiac resynchronization therapy: initial clinical results using multiparametric ECG-gated [^{18}F]FDG PET," *European Journal of Nuclear Medicine and Molecular Imaging*, vol. 40, pp. 1876–1883, 2013.
- [6] J. W. Friedberg, A. Fischman, D. Neuberger et al., "FDG-PET is superior to gallium scintigraphy in staging and more sensitive in the follow-up of patients with de novo Hodgkin lymphoma: a blinded comparison," *Leukemia and Lymphoma*, vol. 45, no. 1, pp. 85–92, 2004.
- [7] A. Buerkle and W. A. Weber, "Imaging of tumor glucose utilization with positron emission tomography," *Cancer and Metastasis Reviews*, vol. 27, no. 4, pp. 545–554, 2008.
- [8] D. Delbeke, R. E. Coleman, M. J. Guiberteau et al., "Procedure guideline for tumor imaging with 18F-FDG PET/CT 1.0," *Journal of Nuclear Medicine*, vol. 47, no. 5, pp. 885–895, 2006.
- [9] S. J. Rosenbaum, T. Lind, G. Antoch, and A. Bockisch, "False-positive FDG PET uptake: the role of PET/CT," *European Radiology*, vol. 16, no. 5, pp. 1054–1065, 2006.
- [10] J. M. Chang, H. J. Lee, J. M. Goo, J. J. Lee, J. Chung, and J. Im, "False positive and false negative FDG-PET scans in various thoracic diseases," *Korean Journal of Radiology*, vol. 7, no. 1, pp. 57–69, 2006.

- [11] T. Urakami, K. Sakai, T. Asai, D. Fukumoto, H. Tsukada, and N. Oku, "Evaluation of O -[^{18}F]fluoromethyl-d-tyrosine as a radio-tracer for tumor imaging with positron emission tomography," *Nuclear Medicine and Biology*, vol. 36, no. 3, pp. 295–303, 2009.
- [12] D. B. Shennan, J. Thomson, M. C. Barber, and M. T. Travers, "Functional and molecular characteristics of system L in human breast cancer cells," *Biochimica et Biophysica Acta*, vol. 1611, no. 1-2, pp. 81–90, 2003.
- [13] K. Kaira, N. Oriuchi, H. Imai et al., "L-type amino acid transporter 1 and CD98 expression in primary and metastatic sites of human neoplasms," *Cancer Science*, vol. 99, no. 12, pp. 2380–2386, 2008.
- [14] H. Uchino, Y. Kanai, D. K. Kim et al., "Transport of amino acid-related compounds mediated by L-type amino acid transporter 1 (LAT1): insights into the mechanisms of substrate recognition," *Molecular Pharmacology*, vol. 61, no. 4, pp. 729–737, 2002.
- [15] T. Miyagawa, T. Oku, H. Uehara et al., "Facilitated amino acid transport is upregulated in brain tumors," *Journal of Cerebral Blood Flow & Metabolism*, vol. 18, no. 5, pp. 500–509, 1998.
- [16] S. Esseghir, J. S. Reis-Filho, A. Kennedy et al., "Identification of transmembrane proteins as potential prognostic markers and therapeutic targets in breast cancer by a screen for signal sequence encoding transcripts," *Journal of Pathology*, vol. 210, no. 4, pp. 420–430, 2006.
- [17] M. T. Travers, I. F. Gow, M. C. Barber, J. Thomson, and D. B. Shennan, "Indoleamine 2,3-dioxygenase activity and L-tryptophan transport in human breast cancer cells," *Biochimica et Biophysica Acta*, vol. 1661, no. 1, pp. 106–112, 2004.
- [18] G. F. Oxenkrug, "Tryptophan-kynurenine metabolism as a common mediator of genetic and environmental impacts in major depressive disorder: the serotonin hypothesis revisited 40 years later," *Israel Journal of Psychiatry and Related Sciences*, vol. 47, no. 1, pp. 56–63, 2010.
- [19] C. Juhász, Z. Nahleh, I. Zitron et al., "Tryptophan metabolism in breast cancers: molecular imaging and immunohistochemistry studies," *Nuclear Medicine and Biology*, vol. 39, no. 7, pp. 926–932, 2012.
- [20] S. D. Krämer, L. Mu, A. Müller et al., "5-(2- ^{18}F -fluoroethoxy)-L-tryptophan as a substrate of system L transport for tumor imaging by PET," *Journal of Nuclear Medicine*, vol. 53, no. 3, pp. 434–442, 2012.
- [21] S. He, G. Tang, K. Hu et al., "Radiosynthesis and biological evaluation of 5-(3-[^{18}F]fluoropropoxy)-L-tryptophan for tumor PET imaging," *Nuclear Medicine and Biology*, vol. 40, no. 6, pp. 801–807, 2013.
- [22] M. Patel, P. Dalvi, M. Gokulgandhi et al., "Functional characterization and molecular expression of large neutral amino acid transporter (LAT1) in human prostate cancer cells," *International Journal of Pharmaceutics*, vol. 443, no. 1-2, pp. 245–253, 2013.
- [23] T. Isobe, A. Onn, D. Morgensztern et al., "Evaluation of novel orthotopic nude mouse models for human small-cell lung cancer," *Journal of Thoracic Oncology*, vol. 8, no. 2, pp. 140–146, 2013.
- [24] K. Kaira, N. Oriuchi, H. Imai et al., "Expression of L-type amino acid transporter 1 (LAT1) in neuroendocrine tumors of the lung," *Pathology Research and Practice*, vol. 204, no. 8, pp. 553–561, 2008.
- [25] X. Fan, D. D. Ross, H. Arakawa, V. Ganapathy, I. Tamai, and T. Nakanishi, "Impact of system L amino acid transporter 1 (LAT1) on proliferation of human ovarian cancer cells: a possible target for combination therapy with anti-proliferative aminopeptidase inhibitors," *Biochemical Pharmacology*, vol. 80, no. 6, pp. 811–818, 2010.
- [26] E. M. del Amo, A. Urtti, and M. Yliperttula, "Pharmacokinetic role of L-type amino acid transporters LAT1 and LAT2," *European Journal of Pharmaceutical Sciences*, vol. 35, no. 3, pp. 161–174, 2008.
- [27] K. Kaira, N. Oriuchi, Y. Otani et al., "Fluorine-18-alpha-methyltyrosine positron emission tomography for diagnosis and staging of lung cancer: a clinicopathologic study," *Clinical Cancer Research*, vol. 13, no. 21, pp. 6369–6378, 2007.
- [28] H. Imai, K. Kaira, N. Oriuchi et al., "L-type amino acid transporter 1 expression is a prognostic marker in patients with surgically resected stage I non-small cell lung cancer," *Histopathology*, vol. 54, no. 7, pp. 804–813, 2009.

Research Article

Evaluation of Inhibitory Effect of Recreational Drugs on Dopaminergic Terminal Neuron by PET and Whole-Body Autoradiography

Skye Hsin-Hsien Yeh,^{1,2,3} Ming-Hsien Lin,^{1,4} Fan-Lin Kong,⁵ Chi-Wei Chang,^{1,6,7}
Li-Chung Hwang,¹ Chien-Feng Lin,⁸ Jeng-Jong Hwang,¹ and Ren-Shyan Liu^{1,3,6,7,9}

¹ Department of Biomedical Imaging and Radiological Sciences, National Yang Ming University, Taipei 11221, Taiwan

² Department of Education and Research, Taipei City Hospital, Taipei 10341, Taiwan

³ Biophotonic and Molecular Imaging Research Center, National Yang Ming University, Taipei 11221, Taiwan

⁴ Division of Nuclear Medicine, Taipei City Hospital Zhongxiao Branch, Taipei 11556, Taiwan

⁵ Department of Cancer Systems Imaging, The University of Texas MD Anderson Cancer Center, TX, USA

⁶ Molecular and Genetic Imaging Core/Taiwan Mouse Clinic, National Comprehensive Mouse Phenotyping and Drug Testing Center, Taipei 11533, Taiwan

⁷ National PET/Cyclotron Center and Department of Nuclear Medicine, Taipei Veterans General Hospital, Taipei 11221, Taiwan

⁸ Nuclear Medicine Department and PET-CT Center, Shuang Ho Hospital Ministry of Health and Welfare, Taipei Medical University, New Taipei City 23561, Taiwan

⁹ Institute of Clinical Medicine, National Yang-Ming University, Taipei 11221, Taiwan

Correspondence should be addressed to Jeng-Jong Hwang; jjhwang@ym.edu.tw and Ren-Shyan Liu; rsliu@vghtpe.gov.tw

Received 27 February 2014; Accepted 27 March 2014; Published 29 April 2014

Academic Editor: David J. Yang

Copyright © 2014 Skye Hsin-Hsien Yeh et al. This is an open access article distributed under the Creative Commons Attribution License, which permits unrestricted use, distribution, and reproduction in any medium, provided the original work is properly cited.

There is little investigation for the functional roles of peripheral dopamine. [¹⁸F]FDOPA has been used in cancer imaging (i.e., neuroendocrine and tumors pancreatic tumors) and neuroimaging (i.e., Parkinson's disease and Huntington's disease). Here, we accessed side effects of recreational drugs such as ketamine, cocaine, and methamphetamine on dopamine neurons in peripheral organs by using positron emission tomography (PET) imaging and quantitative whole-body autoradiography (QWBAR) with [¹⁸F]FDOPA. The images were applied for the measurement of specific binding ratios (SBRs) of striatum with the cerebellum as the reference region. Clear striatal [¹⁸F]FDOPA-derived radioactivity was observed. Moderate level of radiotracer accumulation was presented in the mucosal layers of the stomach and small intestine. The medulla layers of kidney had higher radioactivity than that of the cortex. Blocking images markedly eliminated the specific binding of [¹⁸F]FDOPA in the striatum and in peripheral organs such as stomachs, intestines, and kidney. Ketamine showed the highest inhibitory effect on striatal [¹⁸F]FDOPA-derived radioactivity followed by cocaine and methamphetamine. The current results demonstrated a useful crossing-validating tool that enhances the capability of [¹⁸F]FDOPA for further investigations of the alteration of dopaminergic neurons in the brain disorder or cancer diseases in peripheral tissues.

1. Introduction

The dopaminergic neurotransmitter system plays a crucial role in the mediation of movement cognition and emotion or neuroendocrine nature of tumor cells [1]. Small animal positron emission tomography (PET) imaging of rodent

model as a key component in preclinical research and translational medicine has been used to study dopaminergic function in animal models of human diseases, including neuroendocrine tumors [2], pancreatic tumors [1], Parkinson's disease [3], Huntington's disease [4], and drug abuse [5]. These methods have been recently extended to imaging

of dopaminergic function in genetically manipulated (D_2 receptor [D_2R] knockout) mice [6] or tumor-bearing mouse models [7].

Ketamine (2-*o*-chlorophenyl-2-methylamino cyclohexanone hydrochloride), as an N-methyl-D-aspartate (NMDA) noncompetitive antagonist, is a rapid-acting dissociative general anesthetic and was first used in anesthesia more than 40 years ago. Ketamine increases pain tolerance thresholds and has been shown to preserve laryngeal and pharyngeal reflexes [8]. Ironically, the very properties that restrict its clinical use have made ketamine an increasingly popular drug of abuse, to the extent that it is often erroneously sold as “Ecstasy” [9]. Indeed, ketamine has been reported to induce stereotyped behavior, a common feature of many amphetamine-type psychomotor stimulants [10].

Cocaine and methamphetamine (MA) are two of the most powerful drugs of abuse known. Up to date, there are no effective medications for these drugs abuse, dependence, or withdrawal. Despite many similar behavioral and physiological effects, MA has slower metabolism in the brain which results in it being present in the brain longer than cocaine, leading to prolonged effects [11]. Both cocaine and methamphetamine increase the levels of dopamine in the striatum; however, animal studies have shown that the levels of dopamine are higher when MA is administered [12]. Previous studies demonstrated that cocaine blocks dopamine reuptake, prolonging dopamine activity in the brain, whereas MA not only blocks dopamine reuptake, but also increases the release of dopamine. This in turn causes high dopamine concentrations in the synapse and thus longer lasting effects [12].

The role of dopamine nervous system in drug abuse and addiction has been investigated for some time [13]. The mesolimbic dopamine system, especially the nucleus accumbens (NAc), has received particular attention for its involvement in the reinforcing and addictive properties of cocaine and methamphetamine [14].

In vivo PET imaging using [^{18}F]fluoro-3,4-dihydroxyphenyl-L-alanine ([^{18}F]FDOPA), an analog of L-dihydroxyphenylalanine (L-DOPA), has been used in preclinical [15] and clinical scans of Parkinson's disease or oncology [16]. The accumulation of 6-L-[^{18}F]fluorodopa in the terminals of nigrostriatal dopamine neurons reflects its transport, decarboxylation, and vesicular uptake. The uptake rate constant of 6-L-[^{18}F]fluorodopa in tissue as an *in vivo* index of dopaminergic presynaptic integrity correlates well with the number surviving dopamine neurons in human subjects [17].

The effects of recreational drug such as ketamine, cocaine, and methamphetamine on dopamine neurons have been reported in the brains in rodent [18], nonhuman primate models [19], or human studies [20]; however, there is little investigation for the functional roles of peripheral dopamine or the side effects of these drugs in peripheral organs. The goal of this study was to evaluate the alteration of presynaptic dopaminergic terminal function after acute administration of ketamine by *in vivo* [^{18}F]FDOPA PET imaging and quantitative whole-body autoradiography (QWBAR). In

addition, we also studied groups after treatment with cocaine and methamphetamine to examine whether any observed changes were specific for ketamine. Secondly, we evaluated the roles of peripheral dopamine in metabolic homeostasis using these multi-imaging modalities.

2. Materials and Methods

2.1. ^{18}F -FDOPA Synthesis. [^{18}F]FDOPA synthesis was performed by use of a previously reported procedure [21]. The radiochemical purity was greater than 97% the chemical and radiochemical purities of the product isolated from the semipreparative high-pressure liquid chromatography system that were further confirmed by an analytic high-pressure liquid chromatography method (specific activity $\sim 18.5 \times 10^{10}$ Bq/mmol (5 Ci/mmol)) and were both greater than 99%. The product was made isotonic with sodium chloride and sterilized by passage through a 0.22- μ m Millipore filter into a sterile multidose vial.

2.2. Animals. Four-week-old male BALB/C mice weighing 15–20 g were used in all the studies. The animals were kept on a complete pellet diet (Lab Diet, Richmond, IN, USA) at room temperature of 25°C, with free access to tap water. The animal experiments were approved by the Laboratory Animal Care Panel of the National Yang Ming University.

2.3. Chemicals. Ketamine (Sin-Ton Chemicals, Taipei, Taiwan), methamphetamine (National Bureau of Controlled Drugs, Department of Health, Executive Yuan, Taipei, Taiwan), and cocaine (National Bureau of Controlled Drugs, Department of Health, Executive Yuan, Taipei, Taiwan) were used.

2.4. Pretreatment for [^{18}F]FDOPA. Carbidopa (0.5 mg in 0.25% carbomethyl cellulose sodium salt, Sigma-Aldrich Chemicals) was given intraperitoneally 30 minutes prior to the administration of [^{18}F]FDOPA.

2.5. Biodistribution in Mice. BALB/C mice ($n = 3$ per time point) were injected with 0.1 mL of saline solution containing 3.7 MBq of [^{18}F]FDOPA through the caudal vein. Animals were sacrificed by chloroform (Nacalai Tesque Inc., Japan) at different time points from 2 minutes to 6 hours after administration of [^{18}F]FDOPA. Organs of interest were removed and weighed, and the radioactivity was counted. The radioactivity concentration was determined, decay corrected, and recalculated as percentage injected dose per gram of tissue (%ID/g).

2.6. Quantitative Whole-Body Autoradiography (QWBAR). The procedure has been described previously [22]. Briefly, mice were injected with 0.2 mL of a saline solution containing 3.7 MBq of [^{18}F]FDOPA through caudal veins. Animals were sacrificed by chloroform at 120 minutes after injection and immediately dipped into isopentane (Nacalai Tesque Inc., Japan), which was prechilled with liquid nitrogen. The whole

carcass was frozen for 1-2 minutes, depending on body size. The frozen carcass was then embedded on a cryostat holder ($7 \times 3 \times 5$ cm) with 4% carboxymethylcellulose. The embedded carcass was put on the quick freezing stage (-25°C) in the cryostat (Bright Instrument Company Ltd., UK) for about 120 minutes. Frontal sections were obtained with a Bright OTF cryomicrotome with a slice thickness of $30 \mu\text{m}$. The frozen mice were sectioned at -20°C . Pieces of prechilled adhesive tape (Deer Brand, Four Pillars Company, Taiwan) were used for lifting the frozen sections. Sections attached to tape were air dried at 22°C and awaited further processing.

For quantitative autoradiography (QAR), the tissue sections were exposed for 6–8 hours to the BAS SR-2040 phosphor imaging plate (Fujifilm) along with a set of $20\text{-}\mu\text{m}$ autoradiographic standards of known ^{18}F radioactivity concentration freshly prepared using pork liver homogenate. Images were acquired using a phosphorimager system FLA5100 (Fuji Photo Film Co., Tokyo, Japan). Using the known radioactivity concentration in the standards and the injected dose, the autoradiographic images were converted to color-coded parametric images of percent ID per gram tissue (%ID/g) using image analysis software MCID Elite 7.0 (InterFocus Imaging Ltd.).

2.7. MicroPET Imaging. Animal imaging was performed using the microPET R4 tomography (Concorde Microsystems, Knoxville, USA), which has a 12 cm animal port with an image field of view (FOV) of 11.5 cm. Animals ($n = 3$ per group or per dose of drug) were imaged at 2 hours after injection of 3.7 MBq of $[^{18}\text{F}]\text{FDOPA}$ and immediately positioned in the microPET system. Anesthesia was induced with isoflurane (4%). As soon as deep anesthesia was obtained, endotracheal intubation was performed and anesthesia was maintained by constant insufflations of 2.5% isoflurane in oxygen. Images were acquired over 30 minutes (10 min time frame \times 3).

Scatter-corrected sinograms were reconstructed using the transmission scan data for ordered subset expectation maximization (OSEM). The intrinsic special resolution of the reconstructed images is 1.85 mm full width at half maximum at the center of the field of view. The image pixel size in OSEM reconstructed images was 0.4 mm transaxially with a 1.2 mm slice thickness. Radioactivity in the brains was measured in 15 brain sections.

2.8. Image Analysis. The striatum and cerebellum as a set of regions of interest (ROI) were drawn on the reconstructed PET images using vendor software (ASI Pro 4.1; Concorde Microsystems). Region placement was by reference to an atlas of rodent brain [23]. The cerebellum was used as the reference region assuming that no dopamine receptors are present in this region. The regional radioactivity concentrations (KBq/mL) of $[^{18}\text{F}]\text{FDOPA}$ were estimated from the maximum pixel values within each ROI expressed as percentage of injected dose/tissue g (%ID/g).

2.9. Blocking Experiments. For blocking studies, inhibitors were administered in various doses at 90 minutes after injection of $[^{18}\text{F}]\text{FDOPA}$. The inhibitors and doses used for these experiments were ketamine (35, 45, or 55 mg/kg, i.p.), cocaine (5, 10, 20, or 25 mg/kg, i.v.), and methamphetamine (5, 10, 15, or 20 mg/kg, i.v.), respectively.

2.10. Quantification of Specific to Nonspecific Uptake Ratio of $[^{18}\text{F}]\text{FDOPA}$ in the Mice Brain. The quantification of the specific to nonspecific uptake ratio was calculated by

$$\text{Specific Binding Ratio} = \frac{\text{Radioactivity (\%ID/g)}_{\text{Tissue}} - \text{Radioactivity (\%ID/g)}_{\text{Reference}}}{\text{Radioactivity (\%ID/g)}_{\text{Reference}}} \quad (1)$$

where $\text{Radioactivity (\%ID/g)}_{\text{Tissue}}$ is the radioactivity concentration in the striatum and $\text{Radioactivity (\%ID/g)}_{\text{Reference}}$ is the radioactivity concentration in cerebellum.

3. Results

3.1. Biodistribution of $[^{18}\text{F}]\text{FDOPA}$ in Normal Mice. The time courses of radioactivity of $[^{18}\text{F}]\text{FDOPA}$ in brain and in various organs of the mice are shown in Table 1. The highest activity was observed in the kidney and bladder at the first 15 minutes after injection of $[^{18}\text{F}]\text{FDOPA}$. This pattern of renal clearance was followed by fast increased radioactivity in blood and liver and subsequent clearance by kidneys. High accumulations of radioactivity were found in the liver, spleen, muscle, large intestine, and blood. Brain had the peak of radioactivity concentration in the first 30 min and then showed a gradual decrease over time; however, kidney and bladder showed a redistribution at 120 min after administration of $[^{18}\text{F}]\text{FDOPA}$. Up to 4 hours after injection of $[^{18}\text{F}]\text{FDOPA}$, substantial radioactivity was present in the bladder. There were less radioactivity accumulations in the heart, spleen, testis, muscle, and bone, up to 6 hours after injection.

3.2. In Vivo Imaging of $[^{18}\text{F}]\text{FDOPA}$. For determining pharmacokinetics of $[^{18}\text{F}]\text{FDOPA}$ in the brain of rodents, a baseline PET imaging study was performed. The time course of $[^{18}\text{F}]\text{FDOPA}$ radioactivity, normalized to the %ID/g in striatum and cerebellum of the mouse brain and then calculated for specific binding ratio (SBR), is shown in Figure 1(a). A gradually increased SBR was observed in the brain of mice with the SBR of 0.31 ± 0.026 at 30 minutes, reaching 0.48 ± 0.040 and 0.52 ± 0.008 at 60 and 120 minutes after injection, respectively. Therefore, based on the current results, we concluded that the optimal imaging time point to access SBR for $[^{18}\text{F}]\text{FDOPA}$ in mouse brain was at 120 minutes after administration of $[^{18}\text{F}]\text{FDOPA}$. Thus, in following posttreatment studies, we acquired PET images at 120 minutes after $[^{18}\text{F}]\text{FDOPA}$ administration. In contrast, SBRs were markedly reduced by different concentrations of dopamine reuptake inhibitors, ketamine, cocaine,

TABLE 1: Biodistribution of accumulated radioactivity (%ID/g) in different tissues at the designed time points after administration of [^{18}F]FDOPA in normal mice.

Organs	Radioactivity (% injection dose/tissue g)					
	2 min	15 min	30 min	60 min	120 min	240 min
Skin	0.06 ± 0.030	0.44 ± 0.140	0.47 ± 0.220	0.36 ± 0.510	0.33 ± 0.070	0.31 ± 0.060
Blood	0.12 ± 0.000	0.62 ± 0.170	0.58 ± 0.110	0.45 ± 0.080	0.31 ± 0.060	0.13 ± 0.040
Heart	0.07 ± 0.020	0.63 ± 0.270	0.51 ± 0.020	0.43 ± 0.060	0.28 ± 0.040	0.16 ± 0.050
Spleen	0.04 ± 0.010	0.73 ± 0.130	0.65 ± 0.160	0.44 ± 0.050	0.40 ± 0.110	0.19 ± 0.070
Stomach	0.28 ± 0.090	1.07 ± 0.300	1.15 ± 0.080	0.91 ± 0.150	0.78 ± 0.170	0.47 ± 0.060
Liver	0.06 ± 0.040	0.87 ± 0.210	0.87 ± 0.160	0.58 ± 0.180	0.34 ± 0.090	0.16 ± 0.060
Small intestine	0.09 ± 0.030	0.87 ± 0.200	1.01 ± 0.210	1.13 ± 0.190	0.56 ± 0.220	0.20 ± 0.040
Large intestine	0.05 ± 0.020	0.57 ± 0.170	0.60 ± 0.320	0.49 ± 0.110	0.39 ± 0.040	0.21 ± 0.050
Kidney	0.18 ± 0.060	4.07 ± 1.880	2.84 ± 0.230	2.84 ± 0.560	4.14 ± 0.100	3.25 ± 0.700
Bladder	0.04 ± 0.020	3.75 ± 2.240	7.88 ± 5.220	4.51 ± 1.850	11.25 ± 3.960	2.30 ± 0.850
Testis	0.02 ± 0.010	0.37 ± 0.180	0.40 ± 0.080	0.28 ± 0.020	0.26 ± 0.260	0.16 ± 0.100
Muscle	0.03 ± 0.020	0.50 ± 0.310	0.60 ± 0.370	0.45 ± 0.050	0.45 ± 0.60	0.19 ± 0.080
Bone	0.04 ± 0.020	0.46 ± 0.250	0.43 ± 0.140	0.33 ± 0.040	0.40 ± 0.030	0.19 ± 0.060
Brain	0.02 ± 0.000	0.36 ± 0.180	0.38 ± 0.040	0.31 ± 0.040	0.23 ± 0.040	0.09 ± 0.030

Data shown as average ± standard error of mean ($n = 3$ per time point).

and methamphetamine, respectively (Figures 1(b)–1(d)). In ketamine and cocaine posttreated groups, the SBRs showed the reduction in the striatum with increasing ketamine or cocaine doses, suggesting that ketamine or cocaine inhibits the dopamine reuptake system in a dose-dependent manner resulting in a slower accumulation or inefficient utilization of [^{18}F]FDOPA as an analog of L-DOPA. A similar inhibitory effect was observed in the different dosage regiment of methamphetamine (Figure 1(d)).

PET images showed a significant accumulation of [^{18}F]FDOPA in striatum at 120 min after injection (Figure 2(a)). In contrast, the level of [^{18}F]FDOPA accumulation was reduced in blocking groups (Figures 2(b)–2(d)).

In the separate group of animals ($n = 3$ per group), quantitative whole-body autoradiography (QWBAR) was performed to confirm the PET imaging results and provide anatomic details (Figure 3). At 120 min after injection of [^{18}F]FDOPA, high radioactivity was observed in eye ball and aorta, which had been difficult to be distinguished by PET images (Figure 3(a)). Moderate level of radiotracer accumulation was presented in the mucosal layers of the stomach and small intestine. Little radioactivity could be identified in the brown fat, muscle, liver, and spleen. In kidneys, the medulla layers had higher radioactivity than that of the cortex. Most of the adrenal radioactivity was located in the medulla with a little found in the renal cortex region (Figure 4(a)).

Blocking images obtained from microPET and QWBAR showed marked elimination of the specific binding of [^{18}F]FDOPA in the striatum. The autoradiographies demonstrated a reduction of radiotracer accumulation as compared to the control mice (Figures 3(b)–3(d)). Moreover, the significant inhibitory effect of drugs was also observed

TABLE 2: Accumulation of [^{18}F]FDOPA in different imaging modalities in mice.

Control	PET	QWBAR
30 min	0.251 ± 0.056	0.290 ± 0.028
60 min	0.406 ± 0.090	0.480 ± 0.070
120 min	0.511 ± 0.080	0.523 ± 0.020

Data shown as average ± standard error of mean ($n = 3$ per dose).

in peripheral organs such as stomachs, intestines, and kidneys (Figures 4(a)–4(d)). A summary of quantitative measures of [^{18}F]FDOPA accumulation in control and blocking groups at 120 min post intravitreal injection is provided in Tables 2 and 3.

Correlation of striatal radioactivity values obtained from both PET imaging and QWBAR yielded a Pearson correlation coefficient (r) = 0.9587 (Figure 5(a)). Similarly, the drug-treated determined r values were 0.9061 (ketamine), 0.7864 (cocaine), and 0.9413 (methamphetamine), respectively (Figures 5(b)–5(d)). These results indicated a strong and linear relationship between PET and QWBAR images.

4. Discussion

This is the first study to access the *in vivo* differential alterations in peripheral dopamine by ketamine, cocaine, and methamphetamine using whole-body PET [^{18}F]FDOPA and QWBAR in mice. In comparison with previous reports of [^{18}F]FDOPA [15, 18], our results provided more information on tissue distribution either by tissue dissection or QWBAR and also the distribution in later time points. In the current study, despite the good SBR in striatum and cerebellum of the mice, the hepatobiliary clearance followed two-phase

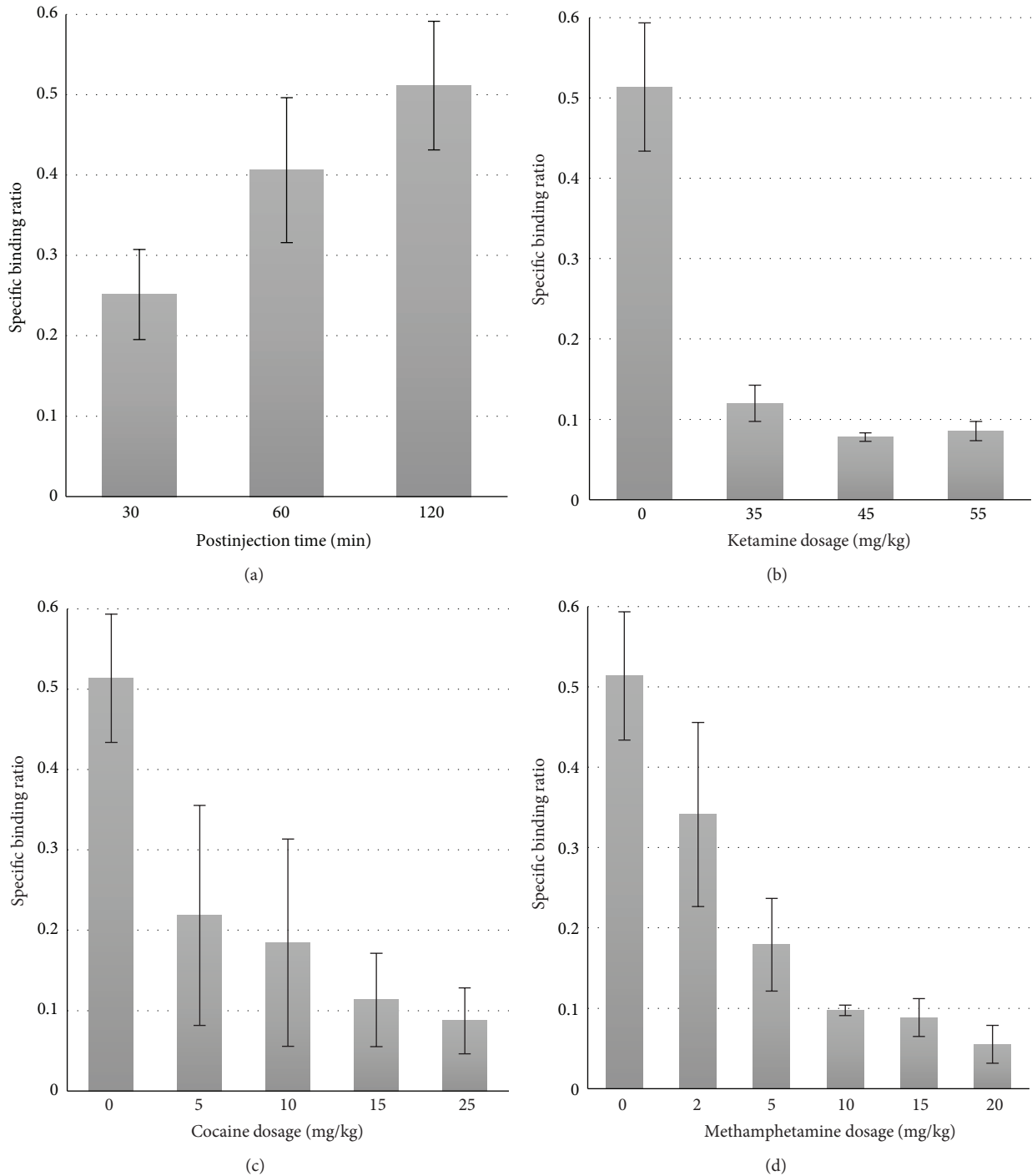


FIGURE 1: Time course of [¹⁸F]FDOPA radioactivity in striatum (a) and quantification of inhibitory effect of recreational drugs on the striatum radioactivity at 120 minutes after administration of [¹⁸F]FDOPA (b) ketamine, (c) cocaine, and (d) methamphetamine. Data shown as average ± standard error of mean (*n* = 3 per time point or per dose).

exponential dissociation kinetics with a fast initial phase (0–15 minutes) and a very slow subsequent phase (30–240 minutes). This biphasic pattern of liver radioactivity was reflected by a rapid increase of radioactivity concentration during the first 15 minutes in the stomach and small intestine. The renal clearance of the radiotracer was rapid and

efficient and was observed by a rapid initial increase in kidney (0–15 minutes) and bladder (0–30 minutes). As the results of such pharmacokinetics of clearance, the radioactivity levels in blood rapidly dropped below 0.12% ID/g during the first 2 minutes after radiotracer injection and had exhibited characteristics of two-phase exponential clearance (Table 1).

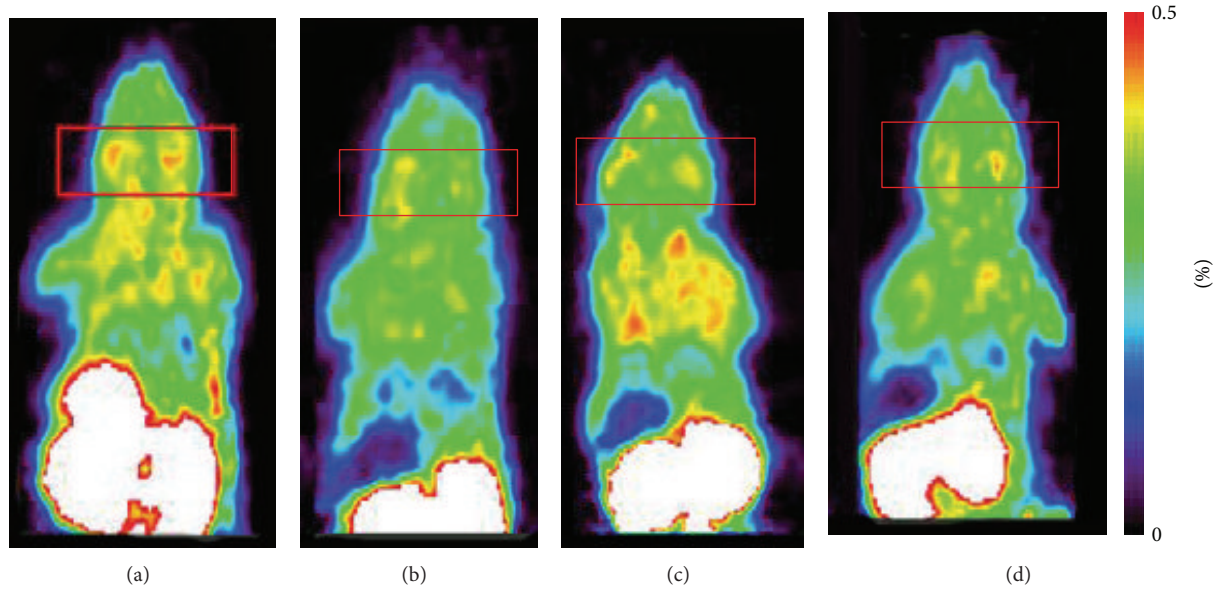


FIGURE 2: An example of axial PET images obtained 120 minutes after administration of [^{18}F]FDOPA in mice showing the specific binding (a) control, following injection of a given dose of (b) ketamine (55 mg/Kg), (c) cocaine (25 mg/Kg), and (d) methamphetamine (20 mg/Kg).

TABLE 3: Accumulation of [^{18}F]FDOPA radioactivity in different imaging modalities in mice after treatment with recreational drugs.

Ketamine	PET	QWBAR
0 mg/kg	0.511 ± 0.080	0.523 ± 0.082
35 mg/kg	0.120 ± 0.022	0.114 ± 0.044
45 mg/kg	0.078 ± 0.005	0.026 ± 0.025
55 mg/kg	0.085 ± 0.012	0.041 ± 0.015
Cocaine	PET	QWBAR
0 mg/kg	0.511 ± 0.080	0.523 ± 0.085
5 mg/kg	0.218 ± 0.137	0.094 ± 0.003
10 mg/kg	0.184 ± 0.129	0.048 ± 0.025
15 mg/kg	0.113 ± 0.058	0.031 ± 0.004
25 mg/kg	0.087 ± 0.041	0.026 ± 0.001
Methamphetamine	PET	QWBAR
0 mg/kg	0.511 ± 0.080	0.523 ± 0.082
2 mg/kg	0.341 ± 0.114	0.093 ± 0.115
5 mg/kg	0.179 ± 0.058	0.068 ± 0.053
10 mg/kg	0.097 ± 0.006	0.048 ± 0.022
15 mg/kg	0.088 ± 0.023	0.035 ± 0.023
20 mg/kg	0.055 ± 0.023	0.026 ± 0.115

Data shown as average \pm standard error of mean ($n = 3$ per dose).

The kidney and bladder had a redistribution peak as compared with the lung and liver. The possible reason could be due to the accumulation of [^{18}F]FDOPA purged by other specific target organs. Based on our results, [^{18}F]FDOPA exhibited a significant hepatobiliary and renal clearances and, therefore, could reduce the radiation exposure of peripheral tissues for imaging brain at 2 hours after radiotracer administration.

We correlated the relationship among tissue-sampling biodistribution, QWBAR, and PET imaging in this study. The evidences of these positive linear relationships between variables suggested that the quantitative imaging crossing multiple-modalities could be a useful tool for preclinical research. However, in using either film or storage phosphor autoradiography as the gold standard for QWBAR, one must be aware of the fact that, because of inherent methodological problems (e.g., quenching, slight variations in slice thickness, quality of standard varying between trails with the bovine cortex, or other organs have been manually dissected and homogenized), this method is not yet supposed to yield error-free results [24, 25].

The nature of specific regional binding of [^{18}F]FDOPA, predominately in the striatum region, was further validated by *in vivo* blocking studies. Virtually all of the selective binding, as indicated by the ratios of striatum/cerebellum, can be blocked by posttreatments with recreational drugs, ketamine, cocaine, and methamphetamine. We also observed the dose-dependent effect of acute administration of these drugs by using PET and QWBAR, which was in a good agreement with previous studies [18, 26, 27]. The inhibition effects of the [^{18}F]FDOPA accumulation in striatum or tissues were varied. The presented data demonstrated that ketamine required higher dose than that of cocaine or methamphetamine to achieve a similar inhibition effect. This may imply that ketamine may have larger half maximal inhibitory (ID_{50}) when compared to the other two; however, it needs further investigations. The explanation could be that ketamine, as an NMDA noncompetitive antagonist, can inhibit the reuptake of dopamine and increase striatal dopamine release [28, 29]. Dopaminergic response induced by ketamine results in excess dopamine into the synaptic

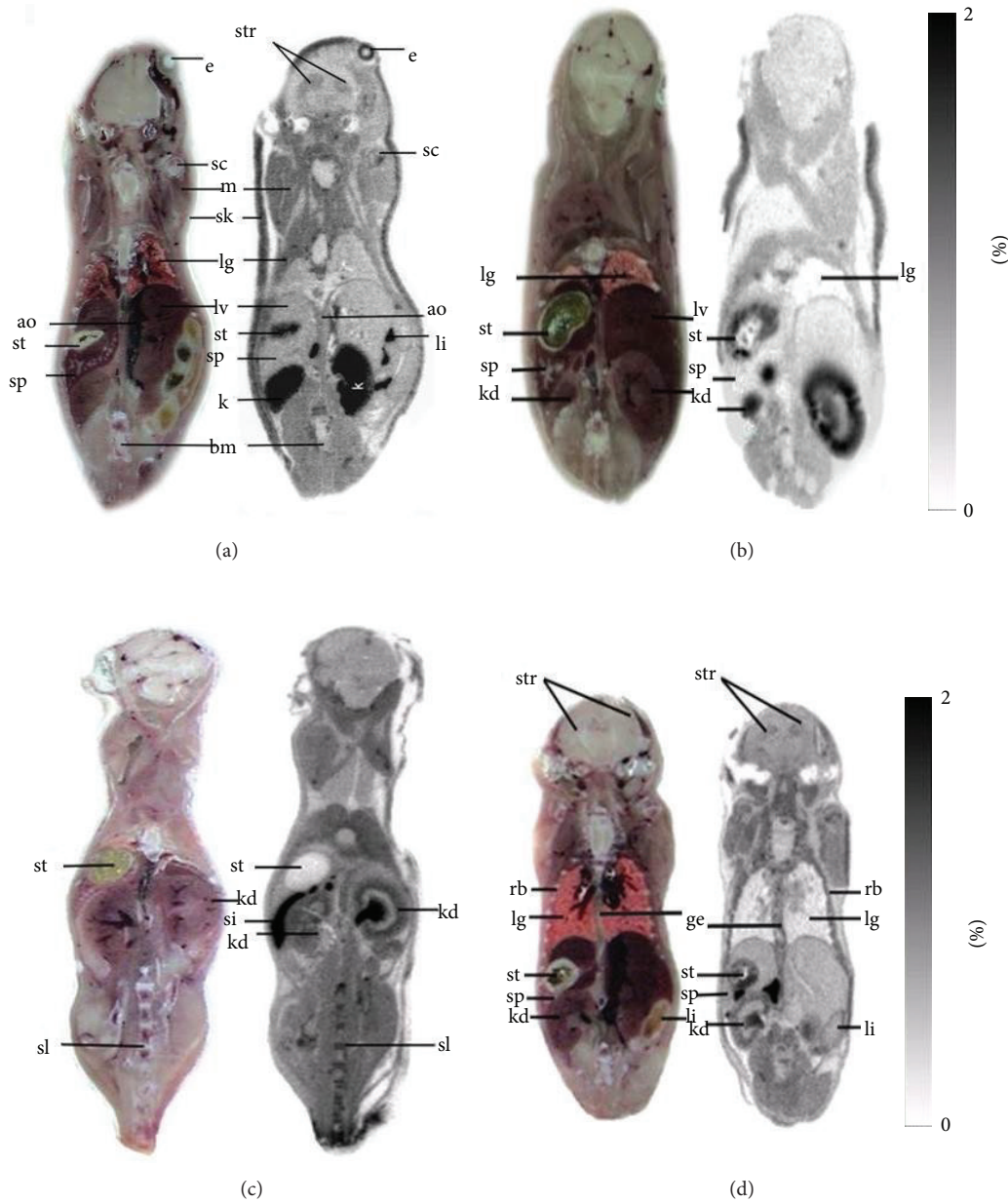


FIGURE 3: An example of axial QWBR images showing $[^{18}\text{F}]$ FDOPA distribution obtained at 120 minutes after administration of $[^{18}\text{F}]$ FDOPA (a) control, following injection of a given dose of (b) ketamine (55 mg/Kg), (c) cocaine (25 mg/Kg), and (d) methamphetamine (20 mg/Kg). ao: aorta; e: eye; str: striatum; bm: bone marrow; k: kidney; lg: lung; li: large intestine; lv: liver; m: muscle; si: small intestine; sk: skin; sp: spleen; st: stomach; rb: rib.

clefts of dopaminergic neurons and then reduces the specific binding of $[^{18}\text{F}]$ FDOPA.

In present study, except for bladder, kidneys had the highest radioactivity concentration. This may raise the possibility of extra radiation burden in the kidney tissues contributed by the radio-metabolites. The potential damage to the organ caused by the extra radiation should be avoided as possible unless only small amount of radiotracer is applied.

On the other hand, it was noted that relatively higher inhibitory effect of recreational drugs was found in renal

medulla when compared to other peripheral tissues, suggesting a mechanism by which recreational drugs abuse may cause urinary tract abnormalities. Despite valuable properties as an anesthetic agent, the use of ketamine has been limited by extent and variety of side effect. There is growing evidence that chronic use or abuse of ketamine is linked with major urological syndrome such as inflammatory cystitis with low volume bladders. Selby et al. reported a clinical case that the inflammatory cystitis and reversible hydronephrosis of ketamine abuse were associated with the precipitation of

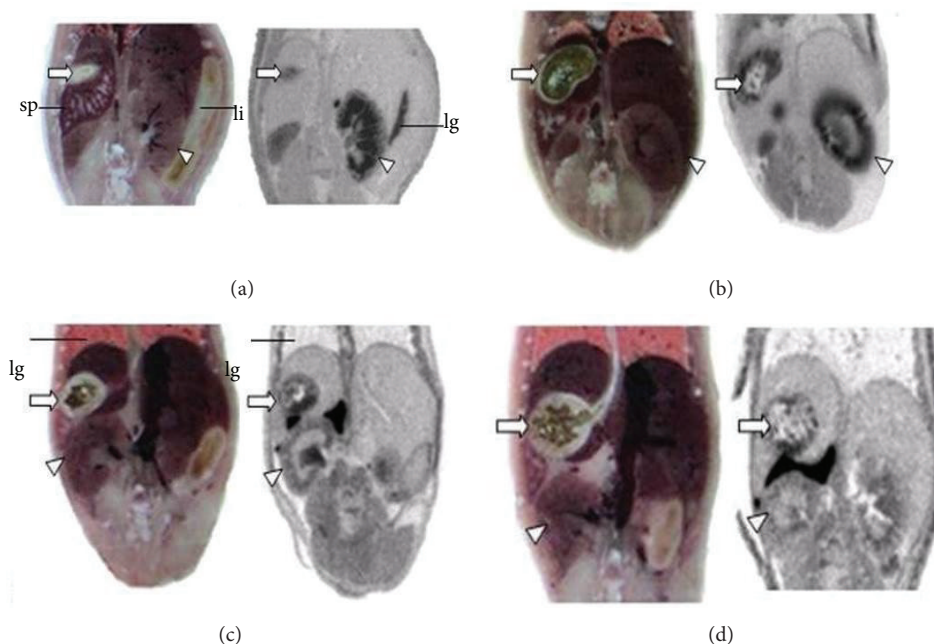


FIGURE 4: An example of magnified view of axial QWBR images of stomach and kidney in the mice obtained at 120 minutes after administration of [^{18}F]FDOPA. Accumulation of the radiotracer was found mainly in the renal medulla; less or none uptake of the radiotracer can be identified in the renal cortex (triangle heads). The radiotracer was accumulated in the mucosal layer of the stomach (arrow heads) but was less accumulated in the intestine. (a) Control group, (b) ketamine (55 mg/Kg), (c) cocaine (25 mg/Kg), and (d) methamphetamine (20 mg/Kg). lg: lung; li: large intestine; k: kidney; sp: spleen; st: stomach.

ketamine metabolites in the ureters and acute renal failure [30]. By using a mouse model, Yeung et al. strengthened the linkage between ketamine addition and urinary tract damage [31]. These findings may also have implications for the drug's use as an antidepressant [32]. Autry et al. showed that in mouse models of depression, ketamine promotes the rapid synthesis of brain-derived neurotrophic factor (BDNF) and p-mTOR that is known to have antidepressant effects, suggesting that this may provide a therapeutic target for developing fast-acting antidepressants [32]. Moreover, Walker et al. developed the means to assess the uptake and trapping rate of dopamine by [^{18}F]FDOPA and the rate constant for the loss of [^{18}F]FDOPA metabolites which enhances the capability of [^{18}F]FDOPA imaging to assist in the development of novel therapies in brain disorder associated with dopaminergic function [33].

Carbidopa, a competitive inhibitor of aromatic L-amino acid decarboxylase (AADC), is routinely used prior to [^{18}F]FDOPA administration in clinical or preclinical study of neuroimaging in order to minimize the peripheral metabolism and to increase radio concentration of in the brain. Carbidopa increased the accumulation of [^{18}F]FDOPA in sham and tumor-bearing mice three- or fourfold, respectively, when compared to vehicle pretreatment. However, there was no significant difference between Carbidopa pretreated sham and tumor-bearing mice [1]. Therefore, we concluded that the effect of Carbidopa in brain and peripheral organs could be neglected since we pretreated

all animal with Carbidopa in the same condition and compared the accumulation of [^{18}F]FDOPA as % inject dose per tissue gram before and after dosing with recreational drugs.

Recently, increasing evidence has implicated ketamine that induces depression of excitatory synaptic transmission in the nucleus accumbens [34]. Also, ketamine causes the alterations of histone deacetylase (HDAC) activity and (BDNF) brain-derived neurotrophic factor in the prefrontal cortex, hippocampus, amygdala, and nucleus accumbens [35]. The current findings support the role of epigenetic mechanisms in nucleus accumbens that contributes to transcriptional and behavioral changes induced by recreational drugs. It motivates that coupled-imaging through PET [^{18}F]FDOPA and [^{18}F]FAHA, a radiotracer for HDAC activity, could be used to evaluate the withdrawal phase which is associated with gene-specific changes in acetylation of histone protein as well as development of antidepressants without these negative effects.

5. Conclusion

The current results provided a useful crossing-validation tool for the further understanding of the alteration of dopaminergic neurons in the brain or peripheral organs. These findings indicated that the [^{18}F]FDOPA imaging along or coupled with [^{18}F]FAHA could be a promising means for assessment the malfunction of peripheral dopamine in tissues including

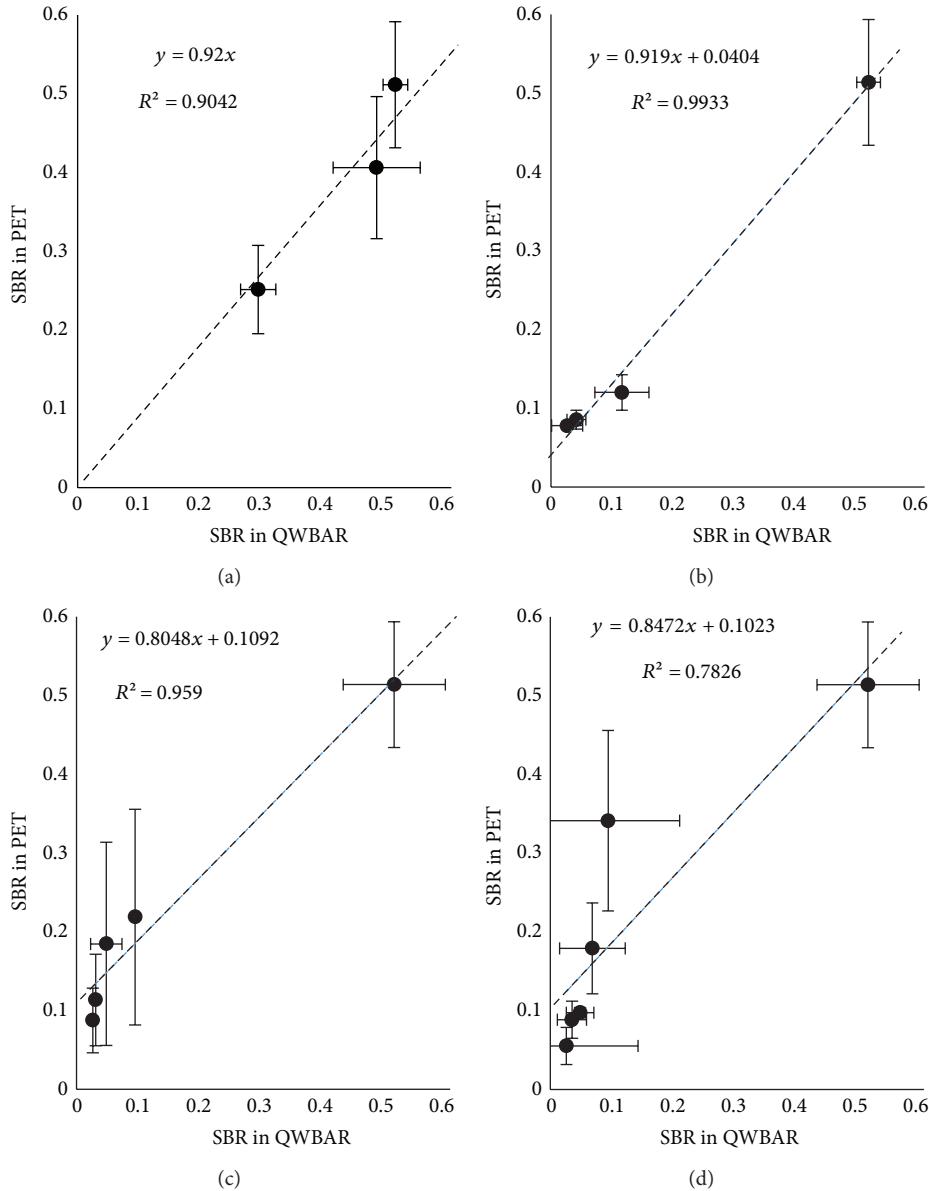


FIGURE 5: Scatter plot and linear regression analysis of relationship between the [¹⁸F]FDOPA PET imaging and QWBAR accumulation in striatum; an almost linear relationship is observed. (a) Control group ($r = 0.96$), (b) ketamine group ($r = 0.99$), (c) cocaine group ($r = 0.98$), and (d) methamphetamine group ($r = 0.88$).

the brain caused by recreational drugs or evaluation of therapy efficiency of antidepressants.

Conflict of Interests

The authors declare that there is no conflict of interests regarding the publication of this paper.

Authors' Contribution

Ming-Hsien Lin equally contributed to the study as the first author.

Acknowledgments

This research was supported by the Grants: 102TPECH13 (Taipei City Hospital, Taiwan), NSC 91-2314-B010-078, NSC100-2923-B-010-001-MY3 (National Science Council, Taiwan), and V102E3-007 (Taipei Veterans General Hospital). The authors thank the technical support from Molecular and Genetic Imaging Core, Taiwan Mouse Clinic (NSC 102-2325-B-001-042) which is funded by the National Research Program for Biopharmaceuticals (NRPB) at the National Science Council (NSC) of Taiwan.

References

- [1] J. Tuomela, S. Forsback, L. Haavisto et al., "Enzyme inhibition of dopamine metabolism alters 6-[¹⁸F]FDOPA uptake in orthotopic pancreatic adenocarcinoma," *EJNMMI Research*, vol. 3, no. 1, p. 18, 2013.
- [2] A. Imperiale, P. Addeo, G. Averous, I. J. Namer, and P. Bachellier, "Solid pseudopapillary pancreatic tumor mimicking a neuroendocrine neoplasm on ¹⁸F-FDOPA PET/CT," *The Journal of Clinical Endocrinology and Metabolism*, vol. 98, no. 7, pp. 2643–2644, 2013.
- [3] S. P. Hume, A. A. Lammertsma, R. Myers et al., "The potential of high-resolution positron emission tomography to monitor striatal dopaminergic function in rat models of disease," *Journal of Neuroscience Methods*, vol. 67, no. 2, pp. 103–112, 1996.
- [4] K. Ishiwata, N. Ogi, N. Hayakawa et al., "Positron emission tomography and ex vivo and in vitro autoradiography studies on dopamine D2-like receptor degeneration in the quinolinic acid-lesioned rat striatum: comparison of [¹¹C]raclopride, [¹¹C]nemonapride and [¹¹C]N-methylspiperone," *Nuclear Medicine and Biology*, vol. 29, no. 3, pp. 307–316, 2002.
- [5] H. Tsukada, J. Kreuter, C. E. Maggos et al., "Effects of binge pattern cocaine administration on dopamine D1 and D2 receptors in the rat brain: an in vivo study using positron emission tomography," *Journal of Neuroscience*, vol. 16, no. 23, pp. 7670–7677, 1996.
- [6] P. K. Thanos, N. B. Taintor, D. Alexoff et al., "In vivo comparative imaging of dopamine D2 knockout and wild-type mice with ¹¹C-raclopride and microPET," *Journal of Nuclear Medicine*, vol. 43, no. 11, pp. 1570–1577, 2002.
- [7] L. Martiniova, S. Cleary, E. W. Lai et al., "Usefulness of [¹⁸F]-DA and [¹⁸F]-DOPA for PET imaging in a mouse model of pheochromocytoma," *Nuclear Medicine and Biology*, vol. 39, no. 2, pp. 215–226, 2012.
- [8] O. H. G. Wilder-Smith, L. Arendt-Nielsen, D. Gäumann, E. Tassonyi, and K. R. Rifat, "Sensory changes and pain after abdominal hysterectomy: a comparison of anesthetic supplementation with fentanyl versus magnesium or ketamine," *Anesthesia and Analgesia*, vol. 86, no. 1, pp. 95–101, 1998.
- [9] D. Shewan and P. Dalgarno, "Ecstasy and neurodegeneration...such as ketamine," *BMJ*, vol. 313, no. 7054, p. 424, 1996.
- [10] S. M. Yentis, N. Hirsch, and G. Smith, Eds., *Anaesthesia and Intensive Care A-Z*, Butterworth-Heinemann, 2003.
- [11] NIDA, *Methamphetamine: Abuse and Addiction*, 2006.
- [12] A. M. Barr, W. J. Panenka, G. W. MacEwan et al., "The need for speed: an update on methamphetamine addiction," *Journal of Psychiatry and Neuroscience*, vol. 31, no. 5, pp. 301–313, 2006.
- [13] R. M. Murray, A. Paparelli, P. D. Morrison, A. Marconi, and M. Di Forti, "What can we learn about schizophrenia from studying the human model, drug-induced psychosis?" *American Journal of Medical Genetics. Part B*, vol. 162B, no. 7, pp. 661–670, 2013.
- [14] Y. Mateo, E. A. Budygin, C. E. John, and S. R. Jones, "Role of serotonin in cocaine effects in mice with reduced dopamine transporter function," *Proceedings of the National Academy of Sciences of the United States of America*, vol. 101, no. 1, pp. 372–377, 2004.
- [15] K. Ishiwata, M. Shinoda, S.-I. Ishii, T. Nozaki, and M. Senda, "Synthesis and evaluation of an ¹⁸F-labeled dopa prodrug as a PET tracer for studying brain dopamine metabolism," *Nuclear Medicine and Biology*, vol. 23, no. 3, pp. 295–301, 1996.
- [16] P. Jokinen, M. Karrasch, A. Brück, J. Johansson, J. Bergman, and J. O. Rinne, "Cognitive slowing in Parkinson's disease is related to frontostriatal dopaminergic dysfunction," *Journal of the Neurological Sciences*, vol. 329, no. 1-2, pp. 23–28, 2013.
- [17] K. Kyono, T. Takashima, Y. Katayama et al., "Use of [¹⁸F]FDOPA-PET for in vivo evaluation of dopaminergic dysfunction in unilaterally 6-OHDA-lesioned rats," *EJNMMI Research*, vol. 1, no. 1, p. 25, 2011.
- [18] C. K. Fang, H. W. Chen, W. H. Wang, R. S. Liu, and J. J. Hwang, "Acute effects of three club drugs on the striatum of rats: evaluation by quantitative autoradiography with [¹⁸F]FDOPA," *Applied Radiation and Isotopes*, vol. 77, pp. 153–159, 2013.
- [19] H. Yamanaka, C. Yokoyama, H. Mizuma et al., "A possible mechanism of the nucleus accumbens and ventral pallidum 5-HT1B receptors underlying the antidepressant action of ketamine: a PET study with macaques," *Translational Psychiatry*, vol. 4, p. e342, 2014.
- [20] C. Wang, D. Zheng, J. Xu, W. Lam, and D. T. Yew, "Brain damages in ketamine addicts as revealed by magnetic resonance imaging," *Frontiers in Neuroanatomy*, vol. 7, p. 23, 2013.
- [21] C. W. Chang, H. E. Wang, H. M. Lin, C. S. Chtsai, J. B. Chen, and R.-S. Liu, "Robotic synthesis of 6-[¹⁸F]fluoro-L-dopa," *Nuclear Medicine Communications*, vol. 21, no. 9, pp. 799–802, 2000.
- [22] K.-J. Lin, X.-X. Ye, T.-C. Yen et al., "Biodistribution study of [¹²³I] ADAM in mice: correlation with whole body autoradiography," *Nuclear Medicine and Biology*, vol. 29, no. 6, pp. 643–650, 2002.
- [23] C. W. George Paxinos, Ed., *The Rat Brain in Stereotaxic Coordinates*, Academic Press, 4th edition, 1998.
- [24] S. Nikolaus, R. Larisch, M. Beu, H. Vosberg, and H.-W. Müller-Gärtner, "Imaging of striatal dopamine D2 receptors with a PET system for small laboratory animals in comparison with storage phosphor autoradiography: a validation study with ¹⁸F-(N-methyl)benperidol," *Journal of Nuclear Medicine*, vol. 42, no. 11, pp. 1691–1696, 2001.
- [25] H. H. Yeh, K. Ogawa, J. Balatoni et al., "Molecular imaging of active mutant L858R EGF receptor (EGFR) kinase-expressing non-small cell lung carcinomas using PET/CT," *Proceedings of the National Academy of Sciences of the United States of America*, vol. 108, no. 4, pp. 1603–1608, 2011.
- [26] H. Tsukada, N. Harada, S. Nishiyama, H. Ohba, and T. Kakiuchi, "Dose-response and duration effects of acute administrations of cocaine and GBR12909 on dopamine synthesis and transporter in the conscious monkey brain: PET studies combined with microdialysis," *Brain Research*, vol. 860, no. 1-2, pp. 141–148, 2000.
- [27] L. K. M. Wright, E. C. Pearson, T. G. Hammond, and M. G. Paule, "Behavioral effects associated with chronic ketamine or remacemide exposure in rats," *Neurotoxicology and Teratology*, vol. 29, no. 3, pp. 348–359, 2007.
- [28] Y. Usun, S. Eybrard, F. Meyer, and A. Louilot, "Ketamine increases striatal dopamine release and hyperlocomotion in adult rats after postnatal functional blockade of the prefrontal cortex," *Behavioural Brain Research*, vol. 256, pp. 229–237, 2013.
- [29] F. X. Vollenweider, P. Vontobel, I. Øye, D. Hell, and K. L. Leenders, "Effects of (S)-ketamine on striatal dopamine: a [¹¹C]raclopride PET study of a model psychosis in humans," *Journal of Psychiatric Research*, vol. 34, no. 1, pp. 35–43, 2000.
- [30] N. M. Selby, J. Anderson, P. Bungay, L. J. Chesterton, and N. V. Kolhe, "Obstructive nephropathy and kidney injury associated with ketamine abuse," *NDT Plus*, vol. 1, no. 5, pp. 310–312, 2008.

- [31] L. Y. Yeung, J. A. Rudd, W. P. Lam, Y. T. Mak, and D. T. Yew, "Mice are prone to kidney pathology after prolonged ketamine addiction," *Toxicology Letters*, vol. 191, no. 2-3, pp. 275–278, 2009.
- [32] A. E. Autry, M. Adachi, E. Nosyreva et al., "NMDA receptor blockade at rest triggers rapid behavioural antidepressant responses," *Nature*, vol. 475, no. 7354, pp. 91–96, 2011.
- [33] M. D. Walker, K. Dinelle, R. Kornelsen et al., "In-vivo measurement of LDOPA uptake, dopamine reserve and turnover in the rat brain using [¹⁸F]FDOPA PET," *Journal of Cerebral Blood Flow & Metabolism*, vol. 33, no. 1, pp. 59–66, 2013.
- [34] M. J. Hunt, K. Kessal, and R. Garcia, "Ketamine induces dopamine-dependent depression of evoked hippocampal activity in the nucleus accumbens in freely moving rats," *Journal of Neuroscience*, vol. 25, no. 2, pp. 524–531, 2005.
- [35] G. Z. Reus, H. M. Abelaira, M. A. dos Santos et al., "Ketamine and imipramine in the nucleus accumbens regulate histone deacetylation induced by maternal deprivation and are critical for associated behaviors," *Behavioural Brain Research*, vol. 256, pp. 451–456, 2013.

Research Article

Rational Design of a Triple Reporter Gene for Multimodality Molecular Imaging

Ya-Ju Hsieh,¹ Luen Hwu,² Chien-Chih Ke,^{2,3} Skye Hsin-Hsien Yeh,^{4,5,6}
Chien-Feng Lin,⁷ Fu-Du Chen,^{2,8} Hsin-Ell Wang,^{2,4} Kang-Ping Lin,⁹
Ran-Chou Chen,^{4,5} and Ren-Shyan Liu^{2,3,4,6,10}

¹ Department of Medical Imaging and Radiological Sciences, Kaohsiung Medical University, No. 100, Shih-Chuan 1st Road, Kaohsiung 80708, Taiwan

² Molecular and Genetic Imaging Core/Taiwan Mouse Clinic, National Comprehensive Mouse Phenotyping and Drug Testing Center, No. 201, Section 2, Shih-Pai Road, Taipei 11217, Taiwan

³ Institute of Clinical Medicine, National Yang-Ming University, No. 155, Section 2, Linong Street, Taipei 11221, Taiwan

⁴ Department of Biomedical Imaging and Radiological Sciences, National Yang-Ming University, No. 155, Section 2, Linong Street, Taipei 11221, Taiwan

⁵ Department of Education and Research, Taipei City Hospital, No. 145, Zhengzhou Road, Datong District, Taipei 10341, Taiwan

⁶ Biophotonic and Molecular Imaging Research Center, National Yang-Ming University, No. 155, Section 2, Linong Street, Taipei 11221, Taiwan

⁷ Nuclear Medicine Department and PET-CT Center, Shunang Ho Hospital Ministry of Health and Welfare, Taipei Medical University, No. 291, Zhongzheng Road, Zhonghe District, New Taipei City 23561, Taiwan

⁸ Center for Teaching and Learning Resources, Chinese Culture University, No. 55, Hwa-Kang Road, Taipei 11114, Taiwan

⁹ Department of Electrical Engineering and Holistic Medical Device Development Center, Chung Yuan Christian University, No. 200, Chung Pei Road, Chung Li City 32023, Taiwan

¹⁰ National PET/Cyclotron Center and Department of Nuclear Medicine, Taipei Veterans General Hospital, No. 201, Section 2, Shih-Pai Road, Taipei 11217, Taiwan

Correspondence should be addressed to Ran-Chou Chen; daa60@tpech.gov.tw and Ren-Shyan Liu; rsliu@vghtpe.gov.tw

Received 16 January 2014; Accepted 25 February 2014; Published 7 April 2014

Academic Editor: Fan-Lin Kong

Copyright © 2014 Ya-Ju Hsieh et al. This is an open access article distributed under the Creative Commons Attribution License, which permits unrestricted use, distribution, and reproduction in any medium, provided the original work is properly cited.

Multimodality imaging using noncytotoxic triple fusion (TF) reporter genes is an important application for cell-based tracking, drug screening, and therapy. The firefly luciferase (*fl*), monomeric red fluorescence protein (*mrfp*), and truncated herpes simplex virus type 1 thymidine kinase SR39 mutant (*ttksr39*) were fused together to create TF reporter gene constructs with different order. The enzymatic activities of TF protein *in vitro* and *in vivo* were determined by luciferase reporter assay, ³H-FEAU cellular uptake experiment, bioluminescence imaging, and micropositron emission tomography (microPET). The TF construct expressed in H1299 cells possesses luciferase activity and red fluorescence. The tTKSR39 activity is preserved in TF protein and mediates high levels of ³H-FEAU accumulation and significant cell death from ganciclovir (GCV) prodrug activation. In living animals, the luciferase and tTKSR39 activities of TF protein have also been successfully validated by multimodality imaging systems. The red fluorescence signal is relatively weak for *in vivo* imaging but may expedite FACS-based selection of TF reporter expressing cells. We have developed an optimized triple fusion reporter construct *DsRedm-fl-ttksr39* for more effective and sensitive *in vivo* animal imaging using fluorescence, bioluminescence, and PET imaging modalities, which may facilitate different fields of biomedical research and applications.

1. Introduction

Multiple molecular imaging techniques have been used not only to monitor complex biological processes both spatially

and temporally but also to study the transplanted cell trafficking, long term monitoring of disease (i.e., cancer progression), and therapeutic effectiveness in living animals

[1, 2]. These techniques have accelerated the translation of *in vitro* based drug discovery studies to *in vivo* imaging-based preclinical and clinical applications [3]. Several noninvasive imaging modalities such as positron emission tomography (PET), single photon emission computed tomography (SPECT), magnetic resonance imaging (MRI), and optical imaging are available for real-time repetitive imaging of reporter gene expression in living subjects [1–4]. Optical imaging is quick and cost-effective and requires no radioisotopes for validating different reporter systems. However, it does not provide optimal tomographic information and quantitative data as compared to 3D radionuclide imaging techniques (i.e., PET, SPECT) [5]. A dual or triple fusion reporter gene construct harboring various fluorescent proteins (i.e., enhanced green fluorescent protein (*egfp*), red fluorescent protein (*rfp*), and different luciferase genes (i.e., firefly luciferase (*fl*), renilla luciferase (*rl*), and herpes simplex virus type 1 thymidine kinase (*tk*) gene)) can combine the advantage of fluorescence, bioluminescence, and radionuclide imaging techniques and overcome the shortcomings of each imaging modality [6].

The *tk-egfp* dual fusion gene allows for microscopic and whole-body fluorescence imaging as well as PET imaging [7]. Another fusion gene, the *tksr39-rl* (*tksr39* is a mutant version of *tk* [8]), was also validated in living mice bearing transduced tumor xenografts by microPET and bioluminescence imaging (BLI) [9]. A triple fusion (TF) reporter gene, truncated *tk-egfp-fl*, was constructed to visualize the TF-transduced cells in living animals by optical, fluorescent, and nuclear imaging modalities [10]. However, the carboxyl-terminal (C-terminal) region of *tk* is involved in the enzymatic catalysis profoundly [11] and fusion of the partner gene such as *fl* gene to the C-terminal region of *tk* would lead to a decreased TK activity (note that *tk* refers to the gene and TK to the protein) [9]. The configuration of *tk-egfp-fl* TF reporter gene is not favorable due to severe influence on TK folding and enzymatic function from the downstream large bulky EGFP-FLUC fusion protein. Several other TF genes had also been constructed and validated, that is, *rl-egfp-ttksr39* [12], *rl-mrfp-ttksr39*, and *fl-mrfp-ttksr39* [3, 13] (*mrfp*: monomeric red fluorescent protein; *ttksr39*: truncated *tksr39*). Because of the intrinsic autofluorescence problem in the living animals, the *egfp*-harboring TF gene constructs were not chosen for *in vivo* imaging applications. In contrast, the efficacy of TF gene construct harboring *rfp* gene in the 293T human embryonic kidney cells or A375M human melanoma cells has been demonstrated in living mice with microPET and optical imaging systems [3]. The *fl-mrfp-ttksr39* reporter gene has also been applied in stem cell research. In 2006, Cao et al. developed murine embryonic stem cells (ESCs) stably expressing human ubiquitin-C (UBC) promoter-driven TF fusion gene and demonstrated that kinetics of ESC survival, proliferation, and migration in living mice could be monitored using multimodality imaging systems [14, 15]. Using lentiviral-mediated transduction, the modified myeloproliferative sarcoma virus (*mnd*) promoter-driven TF gene can be stably expressed in human mesenchymal stem cell (MSC) for *in vivo* monitoring of the efficacy of stem cell transplantation [16]. It is noteworthy that there are no experimental data

using stem cells transduced with an *fl-mrfp-ttksr39* gene construct driven by a constitutive cytomegaloviral (CMV) promoter. Several studies have reported epigenetic silencing of CMV promoter after longitudinal passage of stem cells [16, 17]. Thus, we speculated whether the lentiviral-mediated overexpression of *fl-mrfp-ttksr39* TF driven by the CMV promoter would induce aberrant characteristics or alter differentiation capacity of stem cells.

For drug screening and validation, a less cytotoxic and highly sensitive reporter gene that faithfully reflects the drug effectiveness and eludes the cytotoxic effect of reporter gene product is required. Furthermore, for cell therapy and trafficking, it is also necessary to adopt a less cytotoxic reporter gene to minimize the cellular stress from the aggregation-prone reporter gene product in cell labeling. However, considering the detection sensitivity and limitation, the reporter gene was usually driven by a strong promoter to increase the reporter gene expression and consequently the aggregation-prone reporter gene products accumulated in the transfected cells and ultimately resulted in cellular stress and cytotoxic effect that hampered the cell growth. Previous reports indicated that the *rl-mrfp-ttksr39* or *fl-mrfp-wt.ttk* (*wt.ttk*; truncated wild type *tk*) is the best configuration of TF gene constructs for multimodality imaging techniques, if the *rl* or *fl* are chosen for TF [3, 13]. To best preserve the TK activity for radionuclide imaging the *ttksr39* should be combined with the *rl-mrfp* component and the *wt.ttk* should be combined with the resting *fl-mrfp* component. The enzymatic activity of *ttksr39* or *wt.ttk* could be significantly influenced by fusion with different fusion partners. Furthermore, the intracellular localization of TK-harboring fusion proteins changes significantly while different fusion partner is in-frame fused to *tk* gene or the same fusion partner is in-frame fused to *tk* at N- or C-terminal. The GFP-TK fusion protein is exclusively and homogeneously expressed in the nuclei of the transduced cells, whereas TK-GFP exists as pancellular localization but the majority of proteins are in the nucleus with the massive aggregated form of nuclear bodies [10, 18]. Such intracellular localization of TK-containing fusion protein will result in a reduced enzymatic activity of TK and most likely cause severe cytotoxic effects to cells due to the reporter protein aggregation in the cell nucleus [19, 20]. Because of the advantage of TF reporter construct in the research, we attempted to establish cancer cell clones stably expressing CMV driven *fl-DsRedm-ttksr39* TF gene construct. However, our unpublished studies demonstrated that the fast chromophore maturation of TF is similar to primitive tetrameric DsRed protein suggesting that the TF protein in transfected cells might exist in a tetrameric form. The cell clones only transiently expressed the TF fusion protein and the survived cells did not proliferate after G418 selection and failed to establish clonal populations. Thus, we postulated that the *fl-DsRedm-ttksr39* protein may be toxic to cells. Since the order of fusion genes in TF determines the mRNA structure that may influence ribosomal accessibility or mRNA stability, we aimed to construct a new TF reporter gene with optimal configuration for multimodality imaging, the p3H (*DsRedm-fl-ttksr39*), and to compare this novel TF

gene with other two TF genes, the p3G (*rl-DsRedm-ttksr39*) and p3R (*fl-DsRedm-ttksr39*).

2. Experimental Procedures

2.1. Construction of Triple Fusion Reporter Gene. The *rl-DsRedm-ttksr39* (p3G) and *fl-DsRedm-ttksr39* (p3R) were constructed as described by Ray et al. [3, 12]. The novel triple fusion reporter plasmid, *DsRedm-fl-ttksr39* (p3H), was constructed essentially as described by Ray et al. [3, 12]. Briefly, the monomeric DsRed expression plasmid, *pDsRed-Monomer-CI*, driven by CMV enhancer/promoter, was purchased from Clontech (BD science, Inc., USA). The *pDsRed-Monomer-CI* digested with restriction enzyme of BamH I and Xba I (New England Biolabs, Inc., USA) was purified from 1% agarose gel by PCR/Gel Extraction kit (Geneaid Inc., Taiwan) and used as cloning vector. The truncated *tksr39* gene was amplified from the plasmid *pttksr39* (generous gifts from Professor FD Chen, TransWorld University, Taiwan) by polymerase chain reaction (PCR) with 5'-end primer *ttkUp/BamHI* (5'-CAA GAC GGA TCC TCT GGT AAA ATG CCC ACG CTA CTG C-3'), 3'-end primer *ttkDn-XbaI* (5'-GTA TTC TCT AGA TCA GTT AGC CTC CCC CAT C-3'), and the proof-reading KOD Taq DNA polymerase (Novagen Inc., USA). The *ttksr39* PCR products were purified and subjected to restriction enzyme of BamH I and Xba I (New England Biolabs, Inc., USA) digestion and then the purified *ttksr39* insert DNAs were ligated with BamH I-XbaI digested *pDsRed-Monomer-CI* vector by T4 DNA ligase (New England Biolabs, Inc., USA) generating a *DsRedm-ttksr39* dual fusion reporter genetic construct. The *DsRedm-ttksr39* plasmid was digested with restriction enzyme of EcoR I and Sal I (New England Biolabs, Inc., USA) and used for a cloning vector. The *fl* gene from the pGL3 basic plasmid (Promega Corporation, Madison, WI, USA) was amplified by PCR using the same 5'-end primer *FLUCUp-EcoRI* 5'-AGC ATC GAA TTC TGA GGA CGC CAA AAA CAT AAA G-3', the 3'-end primer *FLUCDn-SalI* 5'-CTA GTA GTC GAC AGC AAT CTT TCC GCC CTT CT-3', and the proof-reading KOD Taq DNA polymerase (Novagen Inc., USA). After purification, the *fl* PCR products were digested with restriction enzyme of EcoR I and Sal I and then were ligated with the EcoR I-Sal I digested *DsRedm-ttksr39* cloning vector to create the *DsRedm-fl-ttksr39* triple fusion reporter genetic construct. To create the *DsRed1-ttksr39* construct, the *pDsRed1-CI* plasmid was digested with Age I and Bam HI, and the *DsRed1* gene was purified from agarose gel electrophoresis and was used as DNA inserts. The *DsRedm-fl-ttksr39* (p3H) plasmid was digested with the same restriction enzymes to remove the *DsRedm-fl* DNA fragment and was used as a vector for cloning *DsRed1* gene. The DNA coding sequences of all constructs were verified by DNA sequencing service (Misson Biotech, Inc., Taiwan) using ABI model 3730 DNA sequencer.

2.2. Cell Culture. The H1299 nonsmall cell lung cancer cells were maintained in RPMI 1640 growth medium supplemented with 10% fetal calf serum at 37°C. Cells were incubated in a humidified incubator at 37°C and 5% CO₂:95% air.

2.3. Cell Transfection and Luciferase Reporter Assays. Cells were seeded into 12-well plates (Orange Inc., USA) at a concentration sufficient to give 80–90% confluency on the day of transfection, typically 8×10^4 cells/well, and cultured overnight. In all, 1.5 µg trifusion reporter plasmids were cotransfected with 0.5 µg of *CMV-rl*, in which the *rl* was driven by CMV promoter, as an internal control for transfection efficiency using Lipofectamine 2000 transfection reagent (Invitrogen, USA) according to the manufacturer's instructions. Briefly, 2 µg of plasmid DNA and 6 µL of Lipofectamine 2000 transfection reagent diluted in serum-free culture medium (Gibco, USA) were used for each transfection. After a 48-hr incubation, cells were analysed for both firefly and renilla luciferase expression using the Dual Luciferase Assay (Promega, USA). All transfections were carried out in triplicate and normalized by the internal control and amounts of protein. Results presented are the means of at least three independent experiments.

2.4. Cellular Uptake Studies. The H1299 cells were cotransfected with reporter gene (p3H, p3R, p3G, *CMV-ttksr39*, and *DsRed1-ttksr39*; 1.8 µg of each construct) and *CMV-egfp* (0.2 µg). The transfected cells (1.0×10^5 cells) were plated in 12-well dishes. Twenty-four hours after ³H-FEAU (1.48 × 10³ Bq/mL [0.4 µCi/mL]) was added in each well and incubated at 37°C for 2 h, cells were washed with cold phosphate-buffered saline (PBS) and lysed by protein extraction reagent (CytoBuster, Novagen, USA), and the radioactivity of each well was measured using beta counter (Perkin-Elmer, USA). The same wells were used to determine the total protein. Because the transfection efficiency of different gene constructs in H1299 cell lines may not be identical, the results were normalized by measuring EGFP expression levels. All results were expressed as the net accumulation of the probe in dpm of cells/dpm of medium/EGFP/µg total protein ± standard error (SE).

2.5. GCV-Mediated Growth Inhibition Studies. Twenty-four hours after transfection with *CMV-fl*, p3H, p3G, p3R, or *DsRed1-ttksr39* plasmids, the transfected cells were reseeded in 96-well flat-bottom microtiter cell culture plates and incubated overnight. Cells were then treated with 300 µL of fresh medium in the presence of varying concentrations of ganciclovir (GCV) (Roche, Germany) for five days at 37°C. The MTT [3-(4,5-dimethyl-thiazol-2-yl)-2,5-diphenyl tetrazolium bromide] (Sigma, USA) was used to treat the cells for 2 h at 37°C. To quantify the cell viability, the formazan products solubilized by DMSO (Sigma, USA) were measured by spectrophotometer (Bio-Rad, USA) with 570 nm and 630 nm of wavelength.

The percentage of cell survival was calculated as

$$\text{Cell viability} = \frac{B}{A} 100\%, \quad (1)$$

where A is the absorbance from the cells incubated with various concentrations of GCV and B is the absorbance from the cells incubated with the medium containing various concentrations of GCV.

2.6. In Vivo MicroPET and Cooled CCD Optical Imaging. The nu/nu nude mice (6–8-week-old, male) were purchased from National Laboratory Animal Center, Taiwan. About 8×10^6 H1299 cells transfected with TF plasmids were subcutaneously injected into the shoulders and legs of the mice. Forty-eight hours posttransfection, each mouse was placed in the black chamber of CCD camera IVIS 50 (Perkin Elmer, USA) equipped with a halogen light source, an excitation filter at 500–550 nm, and an emission filter at 575–650 nm to acquire a whole body image for 1 s. For bioluminescence imaging, the mice were injected with D-luciferin (Promega, USA) intraperitoneally for analysis of *fl* gene expression ($n = 4$) and injected later with coelenterazine (Promega, USA) through tail vein for analysis of *rl* gene expression. Subsequently, static images were obtained from the same anesthetized animals intravenously injected with 0.13 MBq (35 μCi) of ^{18}F -FEAU (100 μL) by using microPET R4 (Concord Microsystems, USA) ($n = 4$). The bioluminescence and fluorescence signals were obtained by a CCD camera thermoelectrically cooled to -70°C . Bioluminescence signals were displayed in pseudocolors and superimposed on the photographic image using Xenogen's Living Image software. Both bioluminescence and fluorescence signals were recorded as maximum photons/second/centimeter²/steradian (photons/sec/cm²/sr). Regions of interest (ROIs) in microPET image were drawn over the tumor and the ROI counts were converted to percentage of injected dose per gram (%ID/g) using filtered back projection [3].

2.7. Immunofluorescence Staining. H1299 transfected cells were seeded onto poly-(lysine) coated coverslips and fixed with 4% paraformaldehyde. Cells permeabilized with 0.1% of Triton X-100 were blocked in 4% BSA/PBS and subsequently probed with primary antibody anti-HSV tk Ab (a generous gift from Professor Juri Gelovani, MD Anderson Cancer Center, TX, USA) followed by goat anti-mouse IgG antibody conjugated to FITC (Santa Cruz, USA). The 4',6-diamidino-2-phenylindole (DAPI) was dropped onto the sections to stain the nuclei. Fluorescent signals from DsRed- or HSV1 tk-expressed cells were obtained using confocal microscopy (Leica TCS SP5, Germany).

2.8. Statistical Analysis. The mean and standard error values were calculated for each group and experimental. The 2-tailed Student's *t*-test and two-way ANOVA were used for statistical analysis using SPSS 15.0 (SPSS, Inc., IL, USA). Statistical significance was defined as $P < 0.05$.

3. Results

3.1. In Vitro Demonstration of the Efficacy of Triple Fusion Reporter Gene. Plasmid DNA of three different TF vectors (p3G, p3R, and p3H) has been used to transiently transfect the H1299 cells, and *pDsRed-Monomer-C1* (BD Science, Clontech, USA) was used for positive control. The transfected cells were first visualized by fluorescence microscopy for monomeric DsRed activity and further assayed for either RLUC or FLUC and tTKSR39 activities. Fluorescence microscopy of transfected cells demonstrated homogenous distribution of positive control protein (*pDsRed-Monomer-C1*) throughout the nucleus and cytoplasm (Figure 1). However, fluorescence in p3H (*DsRedm-fl-ttksr39*) transfected cells was predominantly and uniformly distributed in the cytoplasm with slight fluorescence detectable in the cell nucleus. The majority of cells expressing p3G (*rl-DsRedm-ttksr39*) gene demonstrated tightly packed red fluorescent aggregates mainly in the cytoplasm. Only a small amount of fusion protein appeared in the nucleus. The cells transfected with p3R (*fl-DsRedm-ttksr39*) gene demonstrated a similar distribution pattern of TF fusion protein as positive control, with less aggregation in the cytoplasm and nucleus as compared with the p3G-transfected cells. Among all gene constructs used in this study, the p3G-transfected cells demonstrated higher red fluorescence intensity, as compared to *pDsRed-Monomer-C1* positive control, whereas cells expressing either p3R or p3H gene exhibited relatively lower fluorescence intensity. Curiously, the red fluorescent signal from the p3G and p3R expressing cells could be observed already overnight posttransfection, as compared to *pDsRed-Monomer-C1* and p3H transduced cells, of which the fluorescence was not detectable until 36 hrs posttransfection (data not shown). This phenomenon suggests that p3G and p3R TF reporter protein has faster chromophore maturation rate than that of monomeric DsRed protein. The faster maturation rate is reminiscent of the tetrameric DsRed protein trait. To assess the tTKSR39 enzyme activity, H1299 cells were transiently transfected with TF reporter vectors along with positive control (*CMV-ttksr39*) and negative control (*CMV-DsRed*). The uptake of ^3H -FEAU in p3G-transfected cells was the highest among the three TF reporter vectors ($P < 0.05$), about 33% of positive control (Figure 2(a)). In *fl*-harboring TF vectors, the p3H-transfected cells accumulated more ^3H -FEAU than the p3R-transfected cells (23% versus 19%), indicating that higher tTKSR39 activity is achievable using the p3H vector ($P < 0.05$). Also, we constructed a dual reporter gene (*DsRed1-ttksr39*) as another positive control. In the cells transfected with *DsRed1-ttksr39* gene, a 46% decrease in ^3H -FEAU uptake was observed, as compared with the positive control (*CMV-ttksr39*). However, the tTKSR39 activity in the *DsRed1-ttksr39* construct was still higher (54%) than all three TF vectors. Further, luciferase enzyme assay was used to compare the FLUC activity achieved by p3H and p3R vectors; the *CMV-fl* was used as a positive control for reporter gene expression. The FLUC activity was normalized by measuring the activity of cotransfected *CMV-rl* using dual-luciferase reporter assay system (<http://www.promega.com/tbs/>). The highest FLUC activity was observed in cells transfected with

CMV-fl (Figure 2(b)). The p3H vector retained about 27% of the FLUC activity measurable with positive control and exhibited threefold higher activity than the p3R vector ($P < 0.05$).

3.2. Subcellular Localization of Different Triple Fusion Proteins. Immunofluorescence staining of transfected cells demonstrated distinct differences in subcellular localization of native tTKSR39 and fused tTKSR39 (p3G, p3R, and p3H) proteins. The single tTKSR39 protein exhibited uniform distribution in the nucleus and cytoplasm (Figure 3). Fusion of *tksr39* with p3G, p3R, and p3H genes resulted in predominant cytoplasmic distribution of fusion proteins (Figure 3). This effect was more pronounced in p3H-expressing cells than p3G- and p3R-expressing cells. Moreover, the cells transfected with p3R showed a tendency to form small aggregation in the perinuclear region and the cytoplasm.

3.3. GCV-Mediated Cytotoxicity in Triple Fusion Reporter Gene-Transfected Cells. Efficient tTKSR39 expression in the TF-transfected cells should facilitate the activation of GCV and subsequently enhance cell killing. Cells transfected with either *CMV-fl* or *CMV-tksr39* were used as negative and positive controls, respectively. The slight decrease in cell viability observed in negative control was due to the nature toxicity of GCV to cells (Figure 4). Consistent with the results of *in vitro* ^3H -FEAU accumulation studies, the positive control showed the highest level of tTKSR39 resulting in significant decrease in cell viability (Figure 4). In contrast, all three TF-transfected cell lines exhibited less pronounced GCV-induced cell death than the positive control cells; the cell death induced by GCV in p3R-transduced cells was the lowest among three TF vectors.

3.4. In Vivo Imaging of the Triple Fusion Reporter Gene Expression by Optical and Radionuclide Techniques. Subsequent to *in vitro* studies, we investigated whether the TF vectors would simultaneously and repeatedly express the three fusion proteins in living subjects and would be detectable using different imaging modalities. The H1299 cells transiently transfected with p3G, p3R, p3H, or *DsRed1-tksr39* vectors were injected subcutaneously into the shoulders and legs of 6~8-week-old nude mice (Figure 5(a)). The red fluorescence was detected in tumors grown from p3G-transfected cells with the signal ($80.8 \pm 3 \times 10^6$ photons/sec/cm²/sr) lower than that observed in positive control tumors established from cells expressing *DsRed1-tksr39* gene ($225 \pm 37 \times 10^6$ photons/sec/cm²/sr) but was not detectable in tumors grown from p3R- or p3H-transfected cells (Figure 5(b)). The expression efficacy of *rl* reporter gene in tumors established from p3G-transfected cells was demonstrated by bioluminescence imaging (Figure 5(c)). The bioluminescence signal of RLUC ($1.65 \pm 0.55 \times 10^6$ photons/sec/cm²/sr) was observed in tumors established from cells expressing p3G protein. Tumors expressing p3H protein showed 4-fold higher FLUC activity ($211 \pm 137 \times 10^6$ photons/sec/cm²/sr) than tumors expressing p3R protein ($50.4 \pm 12.44 \times 10^6$

photons/sec/cm²/sr) (Figure 5(d)). Because FEAU has a better substrate affinity to tTKsr39 enzyme than acycloguanosine FHBG [21] and the accumulation of FEAU in the gastrointestinal tract is lower than FHBG, we thus selected ^{18}F -FEAU for monitoring of the *tksr39* reporter gene expression in living subjects (Figure 6(a)). Tumors expressing *DsRed1-tksr39* positive control gene showed 1.36-fold higher level of ^{18}F -FEAU uptake (2.66 ± 0.26 %ID/g) than tumors expressing p3G TF gene (1.96 ± 0.38 %ID/g) (Figure 6(b)). A trend of decreasing ^{18}F -FEAU uptake (p3G > p3H > p3R) in all three TF vectors was observed. However, the differences in ^{18}F -FEAU uptake between each tumor did not reach statistical significance.

4. Discussion

Genetic fusion reporter systems have greatly facilitated studies on the regulation of gene expression, as well as protein localization and function using multiple imaging modalities. Several triple fusion (TF) reporter genes harboring a bioluminescence reporter genes (i.e., *rl* or *fl*), fluorescence reporter genes (i.e., *mrfp* or *egfp*), and a radionuclide imaging reporter gene (*tksr39* or *wt.tk*) have been utilized for *in vivo* imaging of small animals. Our primary interest was to develop TF reporter gene constructs for research applications in cancer, stem cell, and regenerative medicine. However, we have observed that several types of stem cells lost their proliferation ability and showed morphological abnormalities after transfection with p3R developed by Ray et al. [17]. These problems have been resolved in a novel TF gene construct-p3H by changing the orientation of *fl* and *DsRedm* genes in the expression cassette. The C-terminal region of TK is essential for maintaining nucleoside phosphorylation activity of this enzyme [11]. Moreover, the N-terminal tTKSR39 fusion proteins are susceptible to enzymatic cleavage [9]. Therefore, we placed the *tksr39* gene at the carboxyl end of a TF gene construct. The different subcellular distribution pattern of monomeric DsRed or TK in all three TF gene constructs demonstrated that the localization of fusion protein can be influenced not only by the nature of different fusion partner proteins but also by their order in the fusion.

It has been established that chromophore maturation rate and brightness of monomeric DsRed protein are lower than dimeric or tetrameric form [22, 23]. In the current study, fluorescence microscopy demonstrated that chromophore maturation rate in p3G- and p3R-transfected cells (<24 hrs) was faster than that in p3H-transfected cells (>24 hrs), which caused a significant condensation of TF protein in the cytoplasm. One possible explanation of this observation is that the sequence of proteins in p3G and 3R is more prone to formation of DsRed beta-barrel structure, as compared to p3H. Previous studies have also pointed out that due to high levels of reporter gene expression mediated by CMV promoter, the transfected cells may exhibit growth defects [24, 25] and detach from the growth surface [24]. Such cytotoxicity was typical of high levels of RFP expression that causes aggregation of this protein [24, 26]. Significant

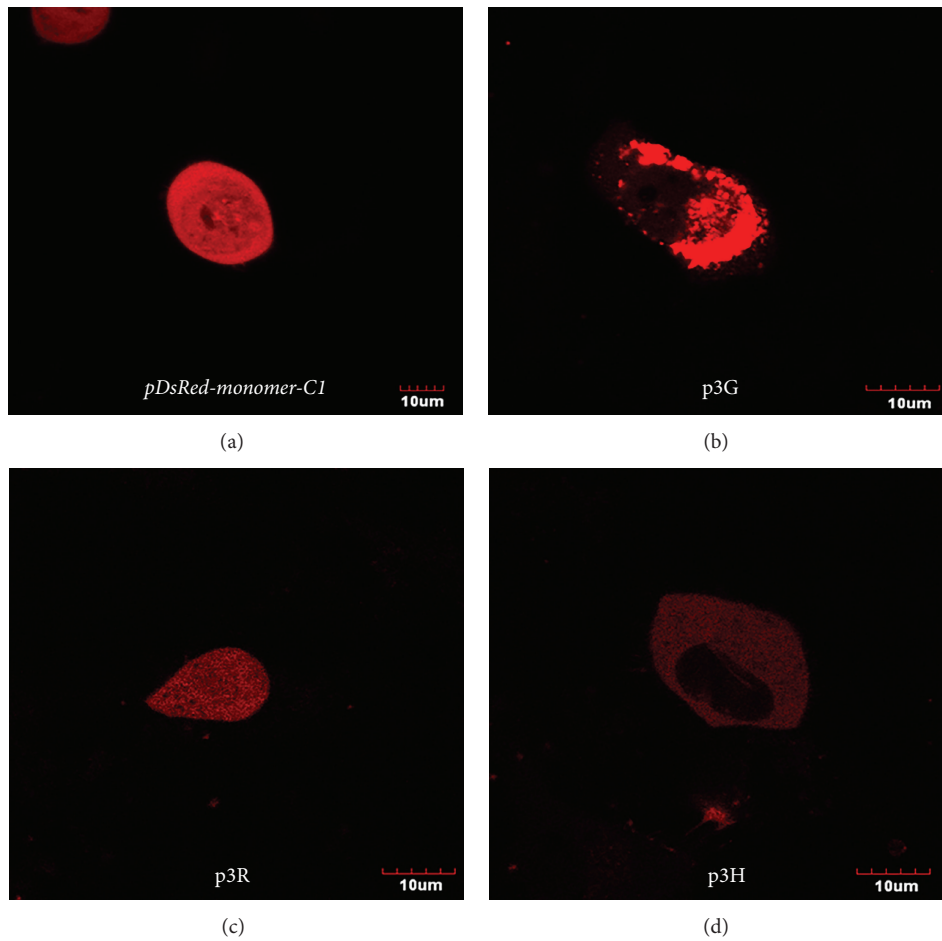


FIGURE 1: Red fluorescence photomicrographs of H1299 cells expressing *pDsRed-Monomer-C1*, *p3G*, *p3R*, and *p3H* gene constructs. Bars for the fluorescence micrographs represent 10 μm .

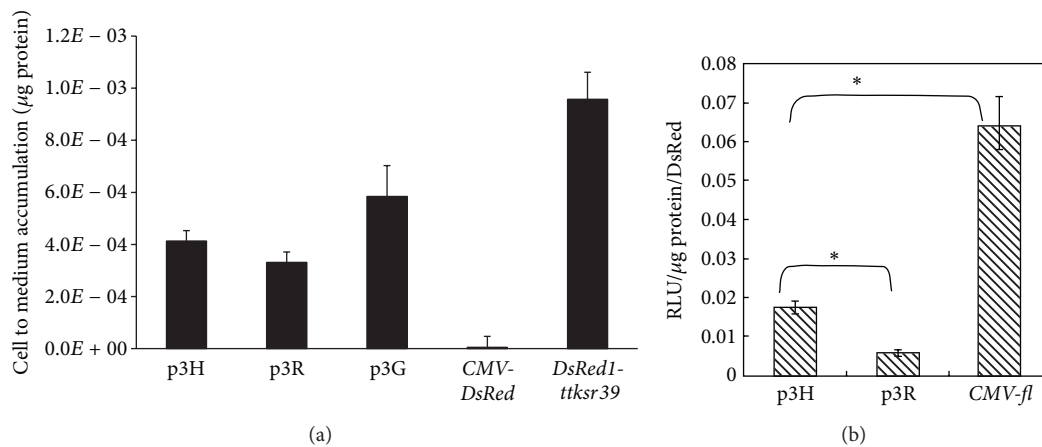


FIGURE 2: The firefly luciferase and tTKSR39 activity exhibited by H1299 cells transiently transfected with different gene constructs. The H1299 cells were cotransfected with *CMV-rl* and *fl*-harboring gene constructs. The tTK activity normalized with CMV-EGFP was expressed as cell to medium accumulation/g protein (a). Values for FLUC activity was normalized with RLUC activity and expressed as relative light units (RLU)/g protein/RLUC activity (b). All the experiments ($n = 4$) were done in triplicate. * $P < 0.05$.

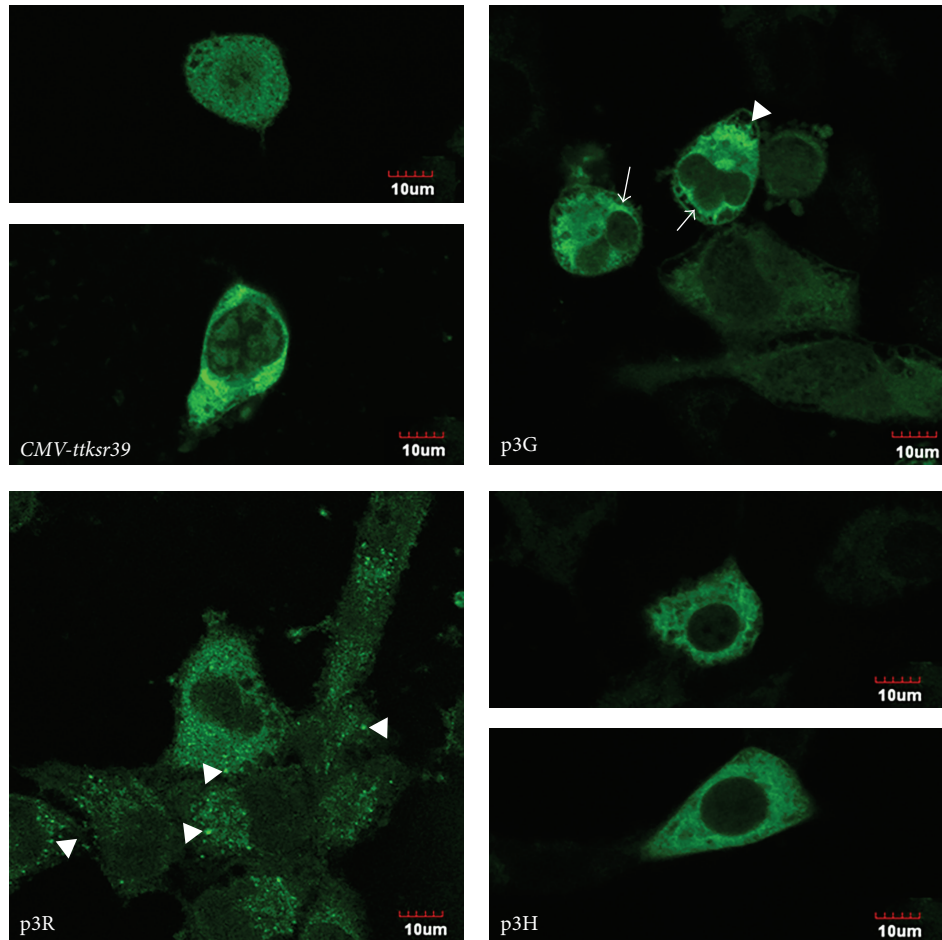


FIGURE 3: Immunofluorescence staining for TKSR39 protein expressed by cells transfected with *CMV-ttksr39*, p3G, p3R, or p3H gene constructs. Arrow heads indicate aggregated proteins of p3G and p3R in cytoplasm. Arrows indicate peri-nuclear distribution of p3G proteins. Bars for the fluorescence micrographs represent 10 μm .

protein aggregates will lead to the impairment of ubiquitin-proteasome system (UPS) that plays an important role in regulating cell division and apoptosis and may cause cell cycle arrest in G2/M [19, 27]. This mechanism may explain at least in part the failure of our previous efforts to establish stable clones of transduced tumor cells using p3G or p3R TF constructs. By using split synthetic renilla luciferase complementation-based bioluminescence assay, Degrève et al. demonstrated the homodimerization of HSV1-TKSR39 [28]. If the tTKSR39 fusion part in p3G or p3R forms homodimer more easily than p3H, the DsRedm fusion part may also form dimeric or tetrameric form resulting in faster chromophore maturation and obvious protein aggregation. In contrast, in p3H the FLUC positioned between DsRed and tTKSR39 may act as a structural barrier to avoid dimerization or tetramerization mediated by tTKSR39. However, as the result of such positioning of RFP in p3H construct, the brightness of RFP fluorescence is relatively lower than that in p3G and p3R.

Previous crystal structure studies revealed that FLUC has a large N-terminal domain (residues 1–436) and a small C-terminal domain (residues 440–550) [29]. During the

enzyme-substrate reaction, the distance between N- and C-terminal needs to be close enough to sandwich the substrate [30]. Previous studies indicated that not only the C-terminal domain of FLUC is indispensable for efficient coupling of adenylation and oxidation steps [21] but also the extreme N-terminal amino acid sequence of FLUC is important in thermal stability and proper conformation of this enzyme [31]. In fact, the N-terminal amino acids from residues 1 to 11 are not directly involved in the active site of FLUC, which is located in the cleft formed by N- and C-terminal domains [21]. The FLUC activity has been shown to be 50-fold higher in cells expressing the *wt.tk-fl* fusion gene, as compared to cells expressing the *fl-wt.tk* fusion gene [32]. To test the effect of N-terminal amino acid modification on the FLUC enzyme activity, the GAL4 DNA binding domain was fused with the N terminus of *fl*, and the results showed that the enzymatic activity of FLUC from GAL4-FLUC fusion protein is as normal as in the nonfused protein [31]. The N terminus of FLUC seems to be more tolerant of fusions than the C terminus. Therefore, we hypothesized that changing the sequence of genes in the *fl-mrffp* fusion to *mrffp-fl* may improve the enzymatic activity of FLUC. The results of

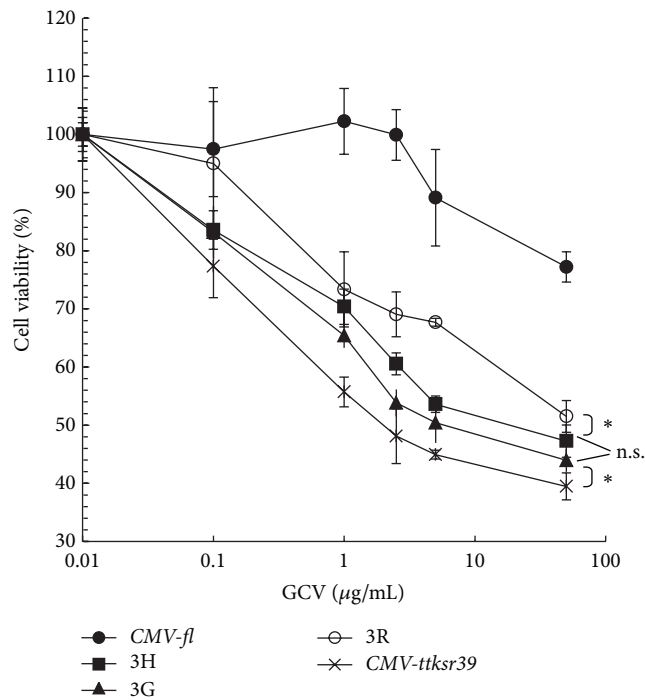


FIGURE 4: *In vitro* cytotoxicity effect of GCV in H1299 cells transfected with *CMV-fl* (●), p3H (■), p3G (▲), p3R (○), or *CMV-ttksr39* (×) constructs. Cells transfected with these constructs were incubated with various concentrations of GCV for 5 days followed by cell survival estimation using MTT. All the experiments ($n = 4$) were done in triplicate. * $P < 0.05$; n.s.: statistically nonsignificant.

our studies demonstrated a 3-fold improvement of FLUC enzymatic activity in p3H-expressing cells, as compared to the p3R-expressing cells, which supports our hypothesis. Another probable reason for impaired FLUC activity is that the close proximity of the bulky DsRedtTKSR39 to FLUC may increase the distance between C- and N-terminal domains of FLUC and interfere with the active site formation and/or function [30, 31]. As expected, the functional activity of FLUC was partially preserved in both p3H and p3R TF gene constructs.

The truncated *tksr39* we choose for one partner of our TF gene construct lacks the first 45 amino acids and is designed to disrupt its nuclear localization signal (NLS) and a putative cryptic testicular-specific promoter, which causes sterility in transgenic mouse males [28, 33]. TF constructs harboring this truncated protein exhibit pancellular distribution of the tTKSR39 reporter protein, whereas the wild type TK (wt.TK) localizes predominantly to the cell nucleus and results in improved total cellular enzymatic activity [18]. In addition, the TKSR39 exhibits increased sensitivity towards different acycloguanosine analogues when compared with wt.TK [3]. The TKSR39 has been extensively studied as a reporter gene for noninvasive imaging with PET using different radiolabeled acycloguanosine analogues as reporter probes, including [^{14}C]1-(2'-fluoro-2'-deoxy-D-arabinofuranosyl)-5-methyluracil (^{14}C -FMAU), [^3H]2'-fluoro-2'-deoxyarabinofuranosyl-5-ethyluracil (^3H -FEAU),

[^{14}C]2'-fluoro-2'-deoxy- β -D-arabinofuranosyl-5-iodouracil (^{14}C -FIAU), and [^3H] penciclovir (^3H -PCV) [34]. In the current study, the immunofluorescence images of tTKSR39 protein demonstrated that the p3H-expressing cells have more cytoplasmic localization of TF protein than the p3R-expressing cells indicating that higher tTKSR39 activity is preserved in the p3H construct. Moreover, a significant aggregation of TF protein was observed in the cytoplasm and, especially, in the perinuclear regions of p3R-expressing cells. Such abnormal aggregation of p3R protein had a negative effect on the efficacy of GCV prodrug activating ability of tTKSR39 and resulted in decrease in GCV-induced cytotoxicity, as well as decreased the cellular uptake of ^3H -FEAU, as compared to p3G or p3H reporter constructs. Furthermore, in mouse imaging studies we observed the red fluorescence signals in the implanted tumors established from p3G-transfected cells, albeit the RFP gene expression of p3G was significantly lower than the DsRed1-*tksr39* (positive control). This observation is consistent with previous reports demonstrating that *DsRed1* gene expressed a tetrameric form that has substantially higher fluorescence than the monomeric form [22, 23]. In addition to the strong red fluorescent signal and relatively high RLUC, the TK activity is also preserved in the aggregation-prone p3G TF protein. This provides evidence that the aggregation of p3G TF protein might not severely inhibit the function of the individual proteins in this TF reporter. The red fluorescence of the p3R- and p3H-expressing cells was weak and easily scattered and attenuated by the surrounding tissues *in vivo*. The *fl* gene expression can be successfully monitored *in vivo*, with 4-fold higher FLUC activity in the p3H-expressing cells than in the p3R-expressing cells indicating that the FLUC activity in TF gene constructs is preserved and is sufficient for *in vivo* bioluminescence imaging.

In the current work we clearly demonstrated the differences of tTKSR39 activity among three TF gene constructs by *in vitro* cellular uptake, but the differences in *tksr39* gene expression (1.25- to 1.4-folds) are too small to be discriminated by *in vivo* PET imaging. The individual differences of mice and the transfection efficiency contributed by different gene constructs may mask the small differences in tTKSR39 activity. Although it seems attractive to perform multiple imaging modalities with p3G TF construct, which retained the most activities of each fusion partners among all three TF constructs, the following criteria are in favor of using *fl* for BLI instead of *rl*: (1) in *rl*, the tissue penetration of light is limited due to emissions peaking at 480 nm; (2) the multidrug resistant MDRI p-glycoprotein (PgP) which overexpresses in cancer cells [35] can alter the transport of coelenterazine (the RLUC substrate), resulting in a decreased bioluminescence signals; (3) while injected with *i.p.*, the bioluminescence contributes to high background [36]; (4) coelenterazine is more expensive than D-luciferin (FLUC substrate). We also noted that the origin/source of *fl* reporter gene used by Ray et al. to construct the first and second generation TF gene constructs were different [13]. The nucleotide sequence of a fusion partner gene can influence the structure and stability of TF mRNA and further affect the efficiency of TF protein

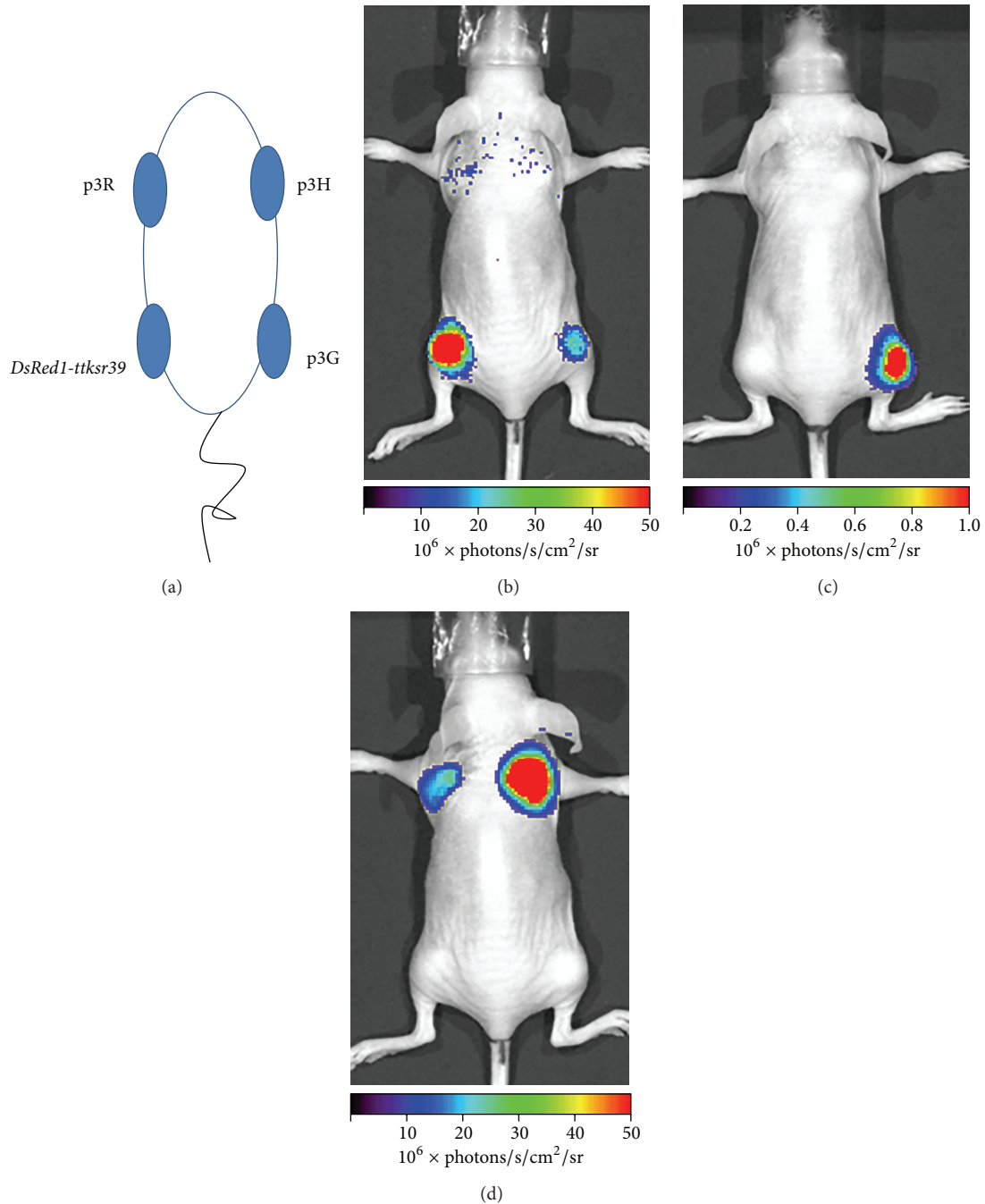


FIGURE 5: Demonstration of triple fusion gene vector in living subjects by optical imaging. Cells transiently expressing p3R, p3H, p3G, and *DsRed1-ttksr39* genes were implanted subcutaneously at four different sites of a nude mouse (a). Red fluorescence signals were detectable only in the regions implanted with *DsRed1-ttksr39*- and p3G-expressing cells (b). Bioluminescence signals resulted from RLUC were found in p3G-expressing cells (c). Different levels of bioluminescence signals resulted from FLUC were observed in p3H- and p3R-expressing cells (d).

translation. It may explain why Ray et al. chose the *wt.tk* as the fusion partner in their second generation TF construct, even though the enzymatic affinity of tTKSR39 mutant to acycloguanisines is higher than that of the wt.TK. In order to eliminate any undesired effect resulting from certain fusion partners of uncertain origin/source, we used commercially available, codon optimized fusion partner genes to construct

the p3G, p3R, and p3H. Thus, the different efficacies between p3R and p3H fusion protein demonstrated in this study resulted solely from the orientation of the genes in the reporter construct.

Our results demonstrated a decreased tTKSR39 activity in all fusion constructs. Longer spacer between the two fusion partner genes might improve the function of each protein

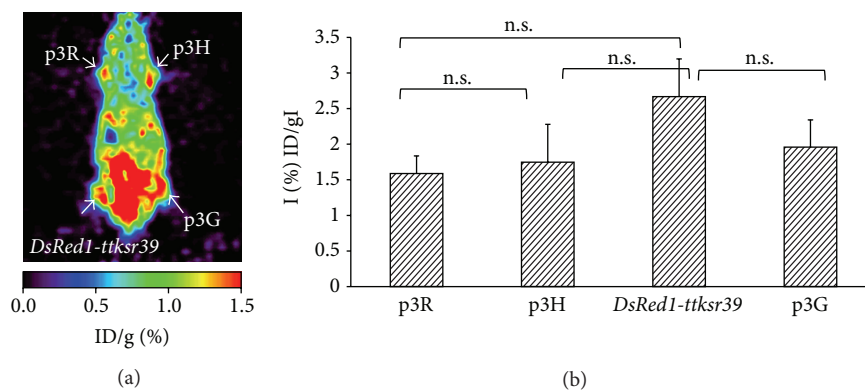


FIGURE 6: Demonstration of triple fusion gene vector in living subjects by microPET imaging. The same mouse demonstrated previously by optical imaging was then imaged by microPET using ^{18}F -FEAU. Cells expressing the fusion reporter genes and *DsRed1-ttk* gene showed ^{18}F -FEAU accumulation in the tumor (coronal section) (a). ROIs drawn over the sites of cell implantation of four mice were calculated and expressed as percentage of injected dose per gram of tissue (% ID/g). Each bar represents the mean \pm SD ($n = 4$) (b). n.s.: statistically nonsignificant.

[9]. Truncation of the first 135bp of the native *tk* coding sequence shortened the distance between *fl* and *tk* genes. Thus, a longer spacer composed of small flexible amino acids, such as poly-glycine, or the use of the minimally truncated *tk* gene (only with deletion of N-amino terminal nuclear localization signal) instead of *tk* can be considered as another option for the next generation of TF gene. Moreover, human codon optimization could be implemented to alter the NLS and the cryptic testicular promoter regions of the full-length *tk* for applications in transgenic mice. Such kind of modification can remove the high frequency of CpG island in *tk* gene and eliminate the CpG methylation associated with transcriptional silencing, resulting in high-yield and long-term gene expression of *tk* [35]. Several new *DsRed* variant genes, such as *mCherry* or *mRaspberry*, could also be used for the new generation of TF genes, which will benefit from far-red emissions spectra and little overlap with GFP and YFP [37].

In conclusion, we have developed an optimized construct of triple reporter gene for multimodality molecular imaging *in vitro* and *in vivo*. The *DsRedm-fl-ttksr39* triple reporter gene is less cytotoxic, more effective, and sensitive for *in vitro* cell imaging as well as *in vivo* animal imaging using fluorescence, bioluminescence, and PET imaging modalities, which may facilitate different fields of translational biomedical research and applications.

Conflict of Interests

The authors declare that there is no conflict of interests regarding the publication of this paper.

Authors' Contribution

Luen Hwu and Ya-Ju Hsieh contributed equally to the study.

Acknowledgments

This research was supported by the following grants: NSC 102-2314-B-010-038-MY3, NSC 102-2627-M-010-003

(National Science Council, Taiwan), MOHW103-TD-B-111-02 (Department of Health), and VI02C-082 (Taipei Veterans General Hospital). The authors thank the technical support from Molecular and Genetic Imaging Core, Taiwan Mouse Clinic (NSC 102-2325-B-001-042), which is funded by the National Research Program for Biopharmaceuticals (NRPB) at the National Science Council (NSC) of Taiwan and Mr. Tsung-Hsun Yu and Ms. Tsuey-Ling Jan for the assistance in preparing the paper.

References

- [1] T. F. Massoud and S. S. Gambhir, "Molecular imaging in living subjects: seeing fundamental biological processes in a new light," *Genes and Development*, vol. 17, no. 5, pp. 545–580, 2003.
- [2] H. R. Herschman, "Molecular imaging: looking at problems, seeing solutions," *Science*, vol. 302, no. 5645, pp. 605–608, 2003.
- [3] P. Ray, A. De, J.-J. Min, R. Y. Tsien, and S. S. Gambhir, "Imaging tri-fusion multimodality reporter gene expression in living subjects," *Cancer Research*, vol. 64, no. 4, pp. 1323–1330, 2004.
- [4] R. Alford, M. Ogawa, P. L. Choyke, and H. Kobayashi, "Molecular probes for the *in vivo* imaging of cancer," *Molecular BioSystems*, vol. 5, no. 11, pp. 1279–1291, 2009.
- [5] C. E. O'Connell-Rodwell, S. M. Burns, M. H. Bachmann, and C. H. Contag, "Bioluminescent indicators for *in vivo* measurements of gene expression," *Trends in Biotechnology*, vol. 20, no. 8, pp. S19–S23, 2002.
- [6] M. Dubrovin, I. Serganova, P. Mayer-Kuckuk, V. Ponomarev, and R. G. Blasberg, "Multimodality *in vivo* molecular-genetic imaging," *Bioconjugate Chemistry*, vol. 15, no. 6, pp. 1376–1388, 2004.
- [7] A. Jacobs, M. Dubrovin, J. Hewett et al., "Functional coexpression of HSV-1 thymidine kinase and green fluorescent protein: implications for noninvasive imaging of transgene expression," *Neoplasia*, vol. 1, no. 2, pp. 154–161, 1999.
- [8] S. S. Gambhir, E. Bauer, M. E. Black et al., "A mutant herpes simplex virus type 1 thymidine kinase reporter gene shows improved sensitivity for imaging reporter gene expression with positron emission tomography," *Proceedings of the National Academy of Sciences of the United States of America*, vol. 97, no. 6, pp. 2785–2790, 2000.

- [9] P. Ray, A. M. Wu, and S. S. Gambhir, "Optical bioluminescence and positron emission tomography imaging of a novel fusion reporter gene in tumor xenografts of living mice," *Cancer Research*, vol. 63, no. 6, pp. 1160–1165, 2003.
- [10] V. Ponomarev, M. Doubrovin, I. Serganova et al., "A novel triple-modality reporter gene for whole-body fluorescent, bioluminescent, and nuclear noninvasive imaging," *European Journal of Nuclear Medicine and Molecular Imaging*, vol. 31, no. 5, pp. 740–751, 2004.
- [11] M. Saijo, T. Suzutani, M. Niikura, S. Morikawa, and I. Kurane, "Importance of C-terminus of herpes simplex virus type 1 thymidine kinase for maintaining thymidine kinase and acyclovir-phosphorylation activities," *Journal of Medical Virology*, vol. 66, no. 3, pp. 388–393, 2002.
- [12] Y. J. Kim, P. Dubey, P. Ray, S. S. Gambhir, and O. N. Witte, "Multimodality imaging of lymphocytic migration using lentiviral-based transduction of a tri-fusion reporter gene," *Molecular Imaging and Biology*, vol. 6, no. 5, pp. 331–340, 2004.
- [13] P. Ray, R. Tsien, and S. S. Gambhir, "Construction and validation of improved triple fusion reporter gene vectors for molecular imaging of living subjects," *Cancer Research*, vol. 67, no. 7, pp. 3085–3093, 2007.
- [14] F. Cao, S. Lin, X. Xie et al., "In vivo visualization of embryonic stem cell survival, proliferation, and migration after cardiac delivery," *Circulation*, vol. 113, no. 7, pp. 1005–1014, 2006.
- [15] F. Cao, M. Drukker, S. Lin et al., "Molecular imaging of embryonic stem cell misbehavior and suicide gene ablation," *Cloning and Stem Cells*, vol. 9, no. 1, pp. 107–117, 2007.
- [16] Z. Love, F. Wang, J. Dennis et al., "Imaging of mesenchymal stem cell transplant by bioluminescence and PET," *Journal of Nuclear Medicine*, vol. 48, no. 12, pp. 2011–2020, 2007.
- [17] Y. H. Kim, D. S. Lee, J. H. Kang et al., "Reversing the silencing of reporter sodium/iodide symporter transgene for stem cell tracking," *Journal of Nuclear Medicine*, vol. 46, no. 2, pp. 305–311, 2005.
- [18] A. Söling, A. Simm, and N. G. Rainov, "Intracellular localization of Herpes simplex virus type 1 thymidine kinase fused to different fluorescent proteins depends on choice of fluorescent tag," *FEBS Letters*, vol. 527, no. 1–3, pp. 153–158, 2002.
- [19] T. F. Massoub, R. Paulmurugan, and S. S. Gambhir, "Molecular imaging of homodimeric protein-protein interactions in living subjects," *FASEB Journal*, vol. 18, no. 10, pp. 1105–1107, 2004.
- [20] N. F. Bence, R. M. Sampat, and R. R. Kopito, "Impairment of the ubiquitin-proteasome system by protein aggregation," *Science*, vol. 292, no. 5521, pp. 1552–1555, 2001.
- [21] K. Ayabe, T. Zako, and H. Ueda, "The role of firefly luciferase C-terminal domain in efficient coupling of adenylation and oxidative steps," *FEBS Letters*, vol. 579, no. 20, pp. 4389–4394, 2005.
- [22] N. C. Shaner, R. E. Campbell, P. A. Steinbach, B. N. G. Giepmans, A. E. Palmer, and R. Y. Tsien, "Improved monomeric red, orange and yellow fluorescent proteins derived from *Discosoma* sp. red fluorescent protein," *Nature Biotechnology*, vol. 22, no. 12, pp. 1567–1572, 2004.
- [23] D. E. Strongin, B. Bevis, N. Khuong et al., "Structural rearrangements near the chromophore influence the maturation speed and brightness of DsRed variants," *Protein Engineering, Design and Selection*, vol. 20, no. 11, pp. 525–534, 2007.
- [24] R. L. Strack, D. E. Strongin, D. Bhattacharyya et al., "A noncytotoxic DsRed variant for whole-cell labeling," *Nature Methods*, vol. 5, no. 11, pp. 955–957, 2008.
- [25] W. Tao, B.-G. Evans, J. Yao et al., "Enhanced green fluorescent protein is a nearly ideal long-term expression tracer for hematopoietic stem cells, whereas DsRed-express fluorescent protein is not," *Stem Cells*, vol. 25, no. 3, pp. 670–678, 2007.
- [26] Y. G. Yanushevich, D. B. Staroverov, A. P. Savitsky et al., "A strategy for the generation of non-aggregating mutants of *Anthozoa* fluorescent proteins," *FEBS Letters*, vol. 511, no. 1–3, pp. 11–14, 2002.
- [27] E. J. Bennett, N. F. Bence, R. Jayakumar, and R. R. Kopito, "Global impairment of the ubiquitin-proteasome system by nuclear or cytoplasmic protein aggregates precedes inclusion body formation," *Molecular Cell*, vol. 17, no. 3, pp. 351–365, 2005.
- [28] B. Degreve, R. Esnouf, E. de Clercq, and J. Balzarini, "Characterization of multiple nuclear localization signals in herpes simplex virus type 1 thymidine kinase," *Biochemical and Biophysical Research Communications*, vol. 264, no. 2, pp. 338–342, 1999.
- [29] R. A. Morton, T. A. Hopkins, and H. H. Seliger, "The spectroscopic properties of firefly luciferin and related compounds. An approach to product emission," *Biochemistry*, vol. 8, no. 4, pp. 1598–1607, 1969.
- [30] E. Conti, N. P. Franks, and P. Brick, "Crystal structure of firefly luciferase throws light on a super-family of adenylate-forming enzymes," *Structure*, vol. 4, no. 3, pp. 287–298, 1996.
- [31] D. Sung and H. Kang, "The N-terminal amino acid sequences of the firefly luciferase are important for the stability of the enzyme," *Photochemistry and Photobiology*, vol. 68, no. 5, pp. 749–753, 1998.
- [32] A. Söling, C. Theiß, S. Jungmichel, and N. G. Rainov, "A dual function fusion protein of Herpes simplex virus type 1 thymidine kinase and firefly luciferase for noninvasive in vivo imaging of gene therapy in malignant glioma," *Genetic Vaccines and Therapy*, vol. 2, no. 1, article 7, 2004.
- [33] J. L. Cohen, O. Boyer, B. Salomon et al., "Fertile homozygous transgenic mice expressing a functional truncated herpes simplex thymidine kinase Δ TK gene," *Transgenic Research*, vol. 7, no. 5, pp. 321–330, 1998.
- [34] K. W. Kang, J.-J. Min, X. Chen, and S. S. Gambhir, "Comparison of [14 C]FMAU, [3 H]FEAU, [14 C]FIAU, and [3 H]PCV for monitoring reporter gene expression of wild type and mutant Herpes simplex virus type 1 thymidine kinase in cell culture," *Molecular Imaging and Biology*, vol. 7, no. 4, pp. 296–303, 2005.
- [35] V. Ponomarev, M. Doubrovin, I. Serganova et al., "Cytoplasmically retargeted HSV1-tk/GFP reporter gene mutants for optimization of noninvasive molecular-genetic imaging," *Neoplasia*, vol. 5, no. 3, pp. 245–254, 2003.
- [36] W. Wang and W. S. El-Deiry, "Bioluminescent molecular imaging of endogenous and exogenous p53-mediated transcription in vitro and in vivo using an HCT116 human colon carcinoma xenograft model," *Cancer Biology & Therapy*, vol. 2, no. 2, pp. 196–202, 2003.
- [37] N. C. Shaner, P. A. Steinbach, and R. Y. Tsien, "A guide to choosing fluorescent proteins," *Nature Methods*, vol. 2, no. 12, pp. 905–909, 2005.